RAL-91-048

Science and Engineering Research Council
Rutherford Appleton Laboratory
Chilton DIDCOT Oxon OX11 0QX

RAL-91-048

Measurement of Atomic Momentum Distribution Functions by Neutron Compton Scattering; Progress on the EVS Spectrometer during 1990

J Mayers and A C Evans

June 1991

MEASUREMENT OF ATOMIC MOMENTUM DISTRIBUTION FUNCTIONS BY NEUTRON COMPTON SCATTERING; PROGRESS ON THE EVS SPECTROMETER DURING 1990

J. MAYERS
RUTHERFORD APPLETON LABORATORY

A. C. EVANS
DEPARTMENT OF PHYSICS, UNIVERSITY OF WARWICK

June 17, 1991

1 Introduction

Compton scattering of high energy photons by electrons is a well established technique for probing electron momentum distributions [1]. The technique relies upon the assumption that when the energy transferred from the photon to the electron is large compared with the electron binding energy, the Impulse Approximation (IA) is valid. The scattering cross-section is then related in a simple way to the electron's momentum. Hohenberg and Platzmann [2] suggested in 1966 that the same principle could be used to measure nuclear momentum distributions by neutron scattering at very high energy transfers. However until the recent advent of spallation neutron sources, such as ISIS at the Rutherford Appleton Laboratory, neutron scattering has been limited by the available intensity at high energies to energy transfers less than $\simeq$ 0.3 electron volts. At such low energy transfers, the IA is inaccurate and the simple relationship between the momentum of the target nucleus and the scattering cross-section does not apply.

ISIS has intensities greater by a factor of $\simeq$ 100 than reactor sources at energies between 1 and $50eV$. The pulsed nature of the source also allows for the use of time-of-flight measurements to measure high energy transfers accurately. On the EVS instrument at ISIS, where energy transfers greater than $10eV$ can be measured, corrections to the IA are small and in principle EVS provides a unique opportunity for accurate measurement of the nuclear momentum distribution function $n(\mathrm{p})$. The function $n(\mathrm{p})$ is one of the most fundamental properties of a condensed matter system and cannot be measured by any other technique. The measurement of atomic momentum distributions by high energy neutron scattering is known as 'Deep Inelastic Neutron Scattering' (DINS), 'Neutron Compton Scattering' or 'Recoil Scattering'.

In systems containing hydrogen it is often a good approximation to replace the interaction between the proton and other atoms by an averaged single particle potential. In this case $n(\mathrm{p})$ is related by Fourier transform to the wavefunction and hence to the spatial localisation of the proton. DINS from hydrogen is complementary to other neutron spectroscopy, which measures the quantised energy levels of the proton in the potential rather than the wavefunction. We anticipate that the main application of EVS will be to measure the momentum distribution of hydrogen or deuterium in, for example, hydrogen bonds, hydrogen in metals and hydrogen in semiconductors. However the instrument has sufficient resolution to measure the momentum distribution of other atoms with atomic masses below $\simeq$ 15 amu.

In this report we summarise the work done during 1990 to develop the EVS spectrometer as a probe of atomic momentum distributions. We start in section 2 by outlining the theory required to understand the DINS technique and data analysis procedures on EVS. In section 3 we describe the EVS instrument. In sections 4 and 5 we describe the calibration procedures and the measurement of the instrument resolution function. In section 6 we describe the data analysis procedures currently used

on EVS and in section 7 we give examples of measurements. In section 8 we discuss the experimental evidence for the validity of the IA on EVS. Finally in section 9 we discuss some current problems and suggest ways in which future progress can be made.

2 Theory

2.1 The Impulse Approximation

The analysis of data on EVS relies upon the assumption that at the high momentum and energy transfers available on the instrument the impulse approximation (IA) is valid. The calculation of corrections to the IA is a difficult theoretical problem [3, 4], but as we show in section 8 corrections to the IA on EVS are small. In this section we discuss the implications of assuming that the IA is valid for the analysis of EVS data.

In the Impulse Approximation, the neutron scattering function $S(\mathbf{q},\omega)$ is given by [5]

$$S(\mathbf{q},\omega) = \int n(\mathbf{p})\delta\left(\omega - \frac{(\mathbf{p}+\mathbf{q})^2}{2M} + \frac{p^2}{2M}\right) d\mathbf{p} \tag{1}$$

where $n(\mathbf{p})d\mathbf{p}$ is the probability that an atom has momentum p, M is the atomic mass, $\mathbf{q}$ is the momentum transfer and ω is the energy transfer. This expression for $S(\mathbf{q},\omega)$ is identical to that obtained for a free gas of particles with a momentum distribution $n(\mathbf{p})$. For a free gas, the δ-function ensures that kinetic energy and momentum are conserved in collisions between neutrons and individual atoms. For purposes of data analysis, we can treat the target system as if it were a fictitious free gas with the momentum distribution of atoms in the target system. However we emphasise that $n(\mathbf{p})$ in the target system, is modified from $n(\mathbf{p})$ of a free gas at the same temperature by particle interactions and hence a measurement of $n(\mathbf{p})$ provides information on these interactions.

Taking the z-axis along $\mathbf{q}$ and using the well known property of the δ-function, $\delta(ax) = \delta(x)/a$, equation 1 reduces to,

$$S(\mathbf{q},\omega) = \frac{M}{q} J(y) \tag{2}$$

where

$$y = \frac{M}{q}\left(\omega - \frac{q^2}{2M}\right) \tag{3}$$

and

$$J(y) = \int n(p_x,p_y,p_z)\delta(p_z - y)dp_x dp_y dp_z = \int n(p_x,p_y,y)dp_x dp_y \tag{4}$$

It follows from equation 4 that the function $J(y)dy$ is the probability that an atom has a momentum component of magnitude y, along the direction of $\mathbf{q}$.

The geometrical interpretation of $J(y)$ in atomic momentum space is shown in figure 2.1. $J(y)$ is calculated by measuring a distance y along the direction of $\mathbf{q}$ from the origin of momentum space to the point $R = y\hat{\mathbf{q}}$, where $\hat{\mathbf{q}}$ is the unit vector parallel to $\mathbf{q}$ and then integrating $n(\mathbf{p})$ over the plane passing through R and perpendicular to $\hat{\mathbf{q}}$. In the simple case illustrated of a Fermi gas at T=0, the momentum distribution is a solid sphere, ie $n(\mathbf{p}) = \rho, p < p_f$ and $n(\mathbf{p}) = 0$ for $p > p_f$. The function $J(y)$ is then proportional to the area of intersection of the sphere with a plane at a distance y from centre of the sphere ie

$$J(y) = \rho\pi(p_f^2 - y^2) \tag{5}$$

J(y) is a parabola for $p < p_f$ and zero for $p > p_f$ as shown.

In a time of flight scan on EVS the point R follows a curved path through p space in the scattering plane as the direction of $\hat{\mathbf{q}}$ and the magnitude of q and ω vary with t. This is illustrated in figure 7.7 where time of flight scans at different detector angles on EVS are shown. For an anisotropic $n(\mathbf{p})$, such as that illustrated in figure 7.7, $J(y)$ depends both upon the direction of $\mathbf{q}$ and the magnitude of y. However in an isotropic system such as a liquid or polycrystalline sample, $J(y)$ depends only on the magnitude of y and reduces to

$$J(y) = \int_{|y|}^{\infty} pn(p)dp \tag{6}$$

The function $J(y)$ is well known from Compton scattering measurements of electron momentum distributions, where the IA is used in an almost identical way to inteprete experimental data. In Compton scattering $J(y)$ is known as the 'Compton profile' [1]. In the context of DINS, $J(y)$ is often referred to as the neutron Compton profile.

The properties of $S(\mathbf{q},\omega)$ which follow from equations 2 to 4 are known in the literature as ' y scaling ' [6]. The condition for conservation of momentum and kinetic energy in equation 1 links the variables q and ω, reducing the number of degrees of freedom by one. Thus in an isotropic system, $qS(\mathbf{q},\omega)$ is a function of one independent variable y rather than of q and ω separately. The presence or absence of y scaling of experimental data can be used to test the validity of the IA. We list the properties of $S(\mathbf{q},\omega)$ which are implied by y scaling.

1. It follows from equation 2 that the magnitude of $S(\mathbf{q},\omega)$ is proportional to $1/q$ at a fixed y. For example along the line $\omega = q^2/(2M)$ where $y = 0$, the amplitude of $S(\mathbf{q},\omega)$ is inversely proportional to q.

2. From equation 3

$$\left(\frac{\partial\omega}{\partial y}\right)_q = \frac{q}{M} \tag{7}$$

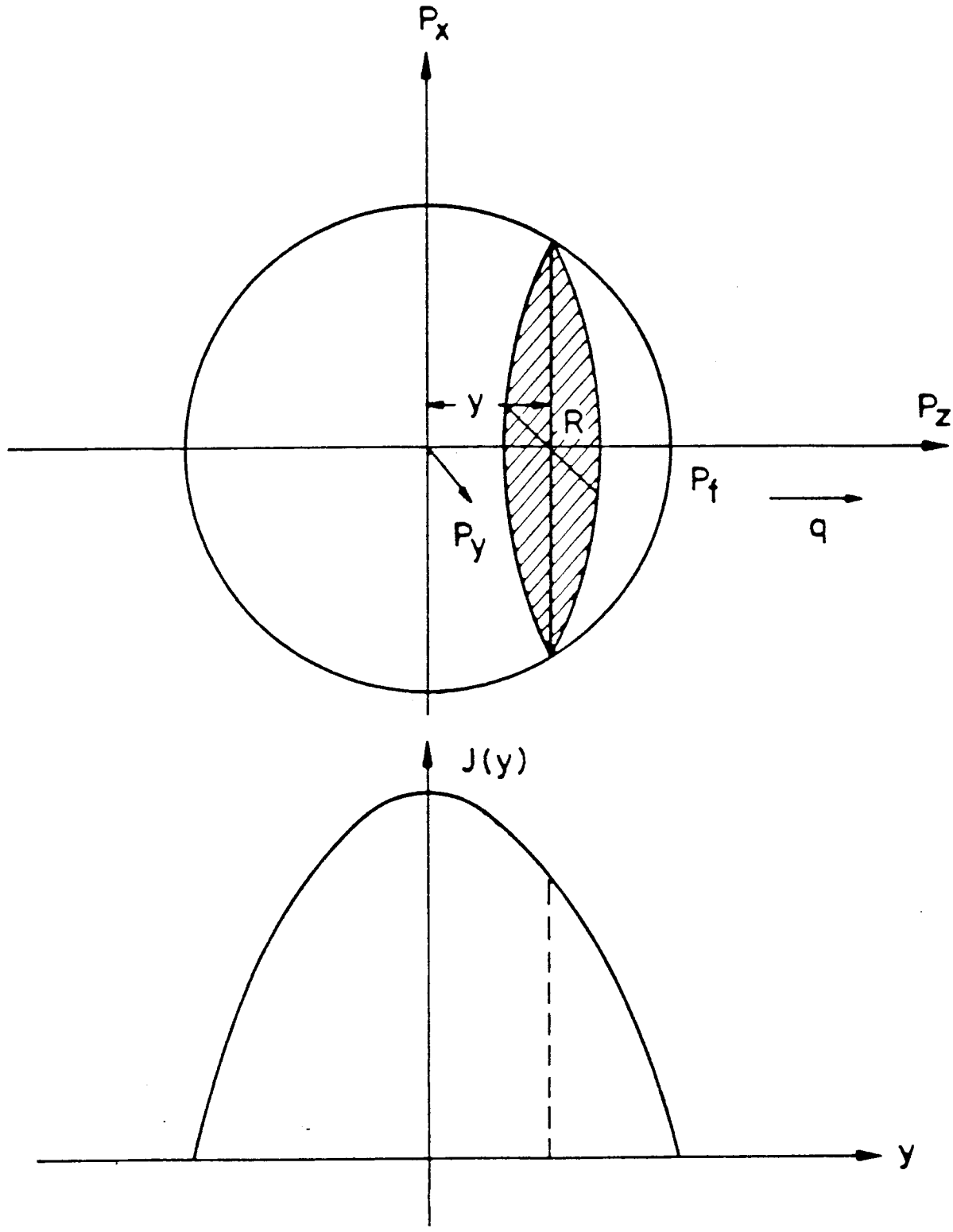

Figure 2.1 Illustration of how the neutron Compton profile $J(y)$ is calculated. $J(y)$ is an integration of $n(\mathbf{p})$ over a plane perpendicular to q at a distance y from the origin of atomic momentum space. In the simple case illustrated $n(\mathbf{p})$ is a solid sphere and $J(y)$ is the area of intersection of the sphere and the plane.

Thus if the FWHM of $J(y)$ is Δy, the FWHM of $S(\mathbf{q},\omega)$ at constant $\mathbf{q}$ is $\Delta\omega = q\Delta y/M$, ie the width of $S(\mathbf{q},\omega)$ is proportional to q.

3. The physical interpretation of $J(y)$ as a probability distribution for atomic momenta, implies that $J(y)$ is an even function of y with its maximum value at $y = 0$. It follows directly from equations 2 and 3 that at constant q, $S(\mathbf{q},\omega)$ has its maximum at the recoil energy $\omega_R = q^2/(2M)$ and is symmetric in ω around ω_R. The locus of the maxima in $S(\mathbf{q},\omega)$ at constant q is the line

$$\omega = \frac{q^2}{2M} \tag{8}$$

Thus if the positions ω_{max} of the maxima in $S(\mathbf{q},\omega)$ are determined for different scattering angles and ω_{max} is plotted as a function of q^2, a straight line through the origin should be obtained, with a gradient inversely proportional to the atomic mass. This procedure can be used to test for inaccuracies in the IA as shown in sections 6.6 and 8.

4. We note the following useful relationship between the initial and final velocities of scattered neutrons whose energy and momentum transfer are linked by equation 8.

$$\alpha = \frac{V_1}{V_0} = \frac{\cos\theta + [(\frac{M}{m})^2 - \sin^2\theta]^{\frac{1}{2}}}{\frac{M}{m} + 1} \tag{9}$$

where V_0 is the incident velocity, V_1 the velocity after scattering, M is the atomic mass, m the neutron mass and θ is the scattering angle. If $M = m$, as is almost the case for scattering from hydrogen, equation 9 reduces to $\alpha = \cos\theta$ and $\alpha = 0$ for $\theta = 90°$. For $\theta > 90°$, scattering from stationary hydrogen atoms does not occur. Thus for measurements of hydrogen momentum distributions, only forward scattering angles are useful.

2.2 Isotropic Harmonic Systems

We illustrate some of the formalism using the model of an isotropic harmonic system, where $S(\mathbf{q},\omega)$ and $J(y)$ can be calculated exactly [4]. In the harmonic approximation the atomic momentum distribution is identical to that for a free gas, except that the temperature T is replaced by an effective temperature T^* [8].

$$n(\mathrm{p}) = \left(\frac{1}{2\pi MT^*}\right)^{3/2} \exp\left(-\frac{p^2}{2MT^*}\right) \tag{10}$$

where

$$T^* = \int \omega Z(\omega) \coth\left(\frac{\omega}{T}\right) d\omega \tag{11}$$

with $Z(\omega)$ the density of states. From equations 4 or 6 we obtain

$$J(y) = \left(\frac{1}{(2\pi MT^*)}\right)^{1/2} \exp\left(-\frac{y^2}{2MT^*}\right) \tag{12}$$

Thus the neutron Compton profile has a Gaussian form with a standard deviation $\sigma = (MT^*)^{\frac{1}{2}}$. In the impulse approximation, it follows from equations 2, 3 and 12 that

$$S(\mathrm{q},\omega) = \left(\frac{1}{4\pi\omega_R T^*}\right)^{1/2} \exp\left(\frac{-(\omega-\omega_R)^2}{4\omega_R T^*}\right) \tag{13}$$

where $\omega_R = q^2/(2M)$.

At $T = 0$, we obtain from the Debye model for $Z(\omega)$

$$\sigma = (MT^*)^{1/2} = \left(\frac{3}{4}0.1196 M\omega_D\right)^{1/2} \tag{14}$$

with M in amu, σ in $\mathring{A}^{-1}$ and ω_D is the Debye energy in meV. Throughout this report, energies and temperatures are measured in milli electron volts (meV), momenta in inverse Angstroms ($\mathring{A}^{-1}$) and masses in atomic mass units (amu). In Appendix B we discuss the conversion factors required to obtain numbers from the various formulae. Equations 10 to 13 also apply to a single particle in an isotropic harmonic potential of frequency ω_0, ie with $Z(\omega) = \delta(\omega - \omega_0)$. At $T = 0$, we obtain,

$$\sigma = (0.1196 M\omega_0)^{1/2} \tag{15}$$

For future reference, some values of T^* and σ calculated at 20K and 290K, using the Debye model for $Z(\omega)$ are given in table 2.1.

Table 2.1 Properties of different elements in the isotropic Debye Approximation. θ_D is the Debye temperature, T the temperature, T^* the effective temperature and σ the standard deviation of the Gaussian momentum distribution.

Element	Mass(amu)	θ_D(K)	T(K)	T^*(K)	$\sigma(\mathring{A}^{-1})$
Li	6.941	400	290	316.9	6.74
Li	6.941	400	20	150.0	4.63
Be	9.012	1000	290	442.2	9.06
Be	9.012	1000	20	374.9	8.35
Al	26.982	394	290	316.1	13.3
Al	26.982	394	20	147.8	9.06
V	50.942	390	290	315.6	18.2
V	50.942	390	20	146.2	12.4
Pb	207.19	88	290	291.2	35.3
Pb	207.19	88	20	36.0	12.4

2.3 Determination of $J(y)$ from EVS Data

A schematic diagram of an inverse geometry spectrometer is shown in figure 2.2. The energy E_1 (and velocity V_1) of the detected neutrons is fixed by the analyser, which on EVS is a resonance foil. The velocity V_0 and energy E_0 of the incident neutron can be determined from the measured time of flight t via

$$t = \frac{L_0}{V_0} + \frac{L_1}{V_1} + t_0 \tag{16}$$

where L_0 is the distance from moderator to sample, L_1 the distance from sample to detector and t_0 is a time delay constant. The energy of the neutron in meV is related to its velocity in m/sec via

$$E = 5.2276 \times 10^{-6} V^2 \tag{17}$$

and the wavenumber of the neutron in $\AA^{-1}$ is related to the energy in meV via

$$k = \left(\frac{E}{2.0717}\right)^{1/2} \tag{18}$$

The energy transfer from the neutron to the target system is

$$\omega = E_0 - E_1 \tag{19}$$

and the momentum transfer q is given by

$$q = (k_0^2 + k_1^2 - 2k_1 k_0 \cos\theta)^{1/2} \tag{20}$$

where θ is the scattering angle.

The q and ω corresponding to a particular time channel in a time of flight spectrum are easily calculated via equations 16 to 20 if the fixed instrument parameters L_0, L_1, θ, t_0, and E_1 are known. The parameter y can then be calculated from equation 3 and the atomic mass M.

The number of counts collected in a time channel of width Δt centred at t is [9],

$$C(t)\Delta t = I(E_0)\frac{dE_0}{dt}\Delta t N \frac{d^2\sigma}{d\Omega dE_1}\eta(E_1)\Delta\Omega\Delta E_1 \tag{21}$$

where $I(E_0)\frac{dE_0}{dt}\Delta t$ is the number of incident neutrons/cm^2 corresponding to the time channel, N is the number of scattering atoms, $\Delta\Omega$ is the detector solid angle, ΔE_1 is the energy resolution of the analyser, $\eta(E_1)$ is the efficiency of the detector and $d^2\sigma/d\Omega dE_1$ is the partial differential neutron scattering cross-section. The latter quantity is related to the neutron scattering function $S(\mathbf{q},\omega)$ via [5],

$$\frac{d^2\sigma}{d\Omega dE_1} = \frac{\sigma}{4\pi}\frac{k_1}{k_0}S(\mathbf{q},\omega) \tag{22}$$

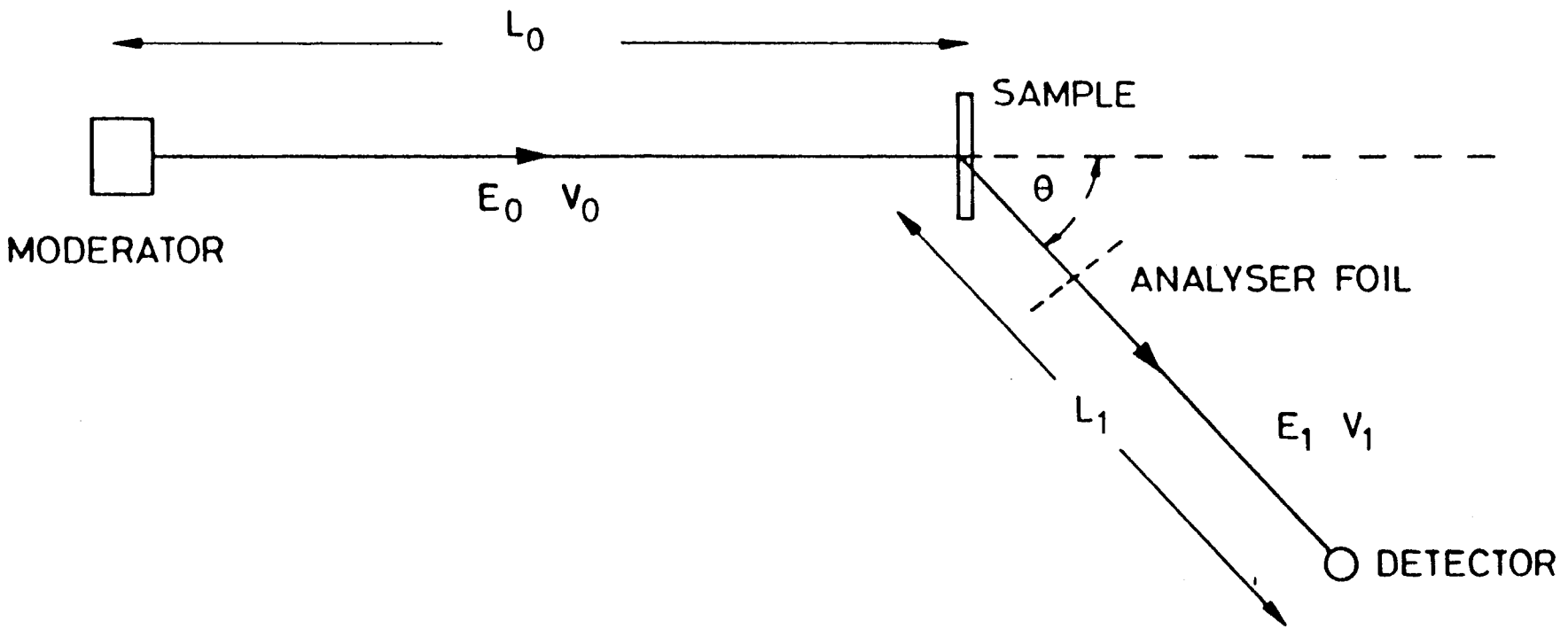

Figure 2.2 Schematic diagram of inverse geometry spectrometer.
L_0 = incident flight path
L_1 = scattered flight path
θ = scattering angle
E_0 = energy of incident neutron
E_1 = energy of detected neutrons

From equations 2, 21 and 22 we obtain,

$$C(t)dt = \left[\frac{N\Delta\Omega\eta(E_1)k_1\Delta E_1\sigma M}{4\pi}\right]\left(\frac{I(E_0)\frac{dE_0}{dt}dtJ(y)}{k_0 q}\right) \tag{23}$$

The brackets [ ] contain all factors which are independent of t. We show in section 3.5 that $I(E_0) \propto E^{-0.9}$. Furthermore $k_0 \propto {E_0}^{0.5}$ and it is easily shown from equations 16 and 17 that for a fixed final energy E_1, $dE_0/dt \propto E_0^{1.5}$. Thus

$$J(y) = A\frac{qC(t)}{E_0^{0.1}} \tag{24}$$

where A is the product of all parameters which are independent of t. The value of A can be determined from

$$\int J(y)dy = 1 \tag{25}$$

which is necessary since $J(y)$ is a probability distribution.

3 The Electron Volt Spectrometer (EVS)

A schematic diagram of the EVS instrument is shown in figure 3.1. At present there are four banks of detectors; two banks of 10 detectors centred at $\pm 45°$and two banks of 5 detectors centred at $\pm 135°$. The detectors are 10 atmosphere ^{3}He gas counters, each of which is 2.5cm in diameter and 30cm in length. The detectors are vertical with their centres in the horizontal plane. In addition to the 30 ^{3}He gas detectors, there are standard ISIS glass scintillator beam monitors, before and after the sample position. The standard sample geometry is a plane slab perpendicular to the incident beam, which is circular with a diameter of 3cm at the sample position.

On EVS the final energy is determined using the filter difference technique [10]. The filter is a thin foil of a material containing a nuclear resonance absorption, with a significant absorption cross-section only over a narrow range of neutron energies. Two measurements are made; the first with the foil placed between the sample and the detectors and the second with the foil removed. The difference between these two measurements provides a measurement of the scattered neutron energy E_1 with a resolution

$$R(E_1) = 1 - T(E_1) \tag{26}$$

where $T(E_1)$ is the transmission of the foil as a function of energy.

Most heavy elements contain nuclear resonance absorption peaks but only a few are suitable for the filter difference technique. The main requirements are

1. A narrow intrinsic width for the resonance absorption peak in the cross-section. This width determines the energy resolution of the instrument.

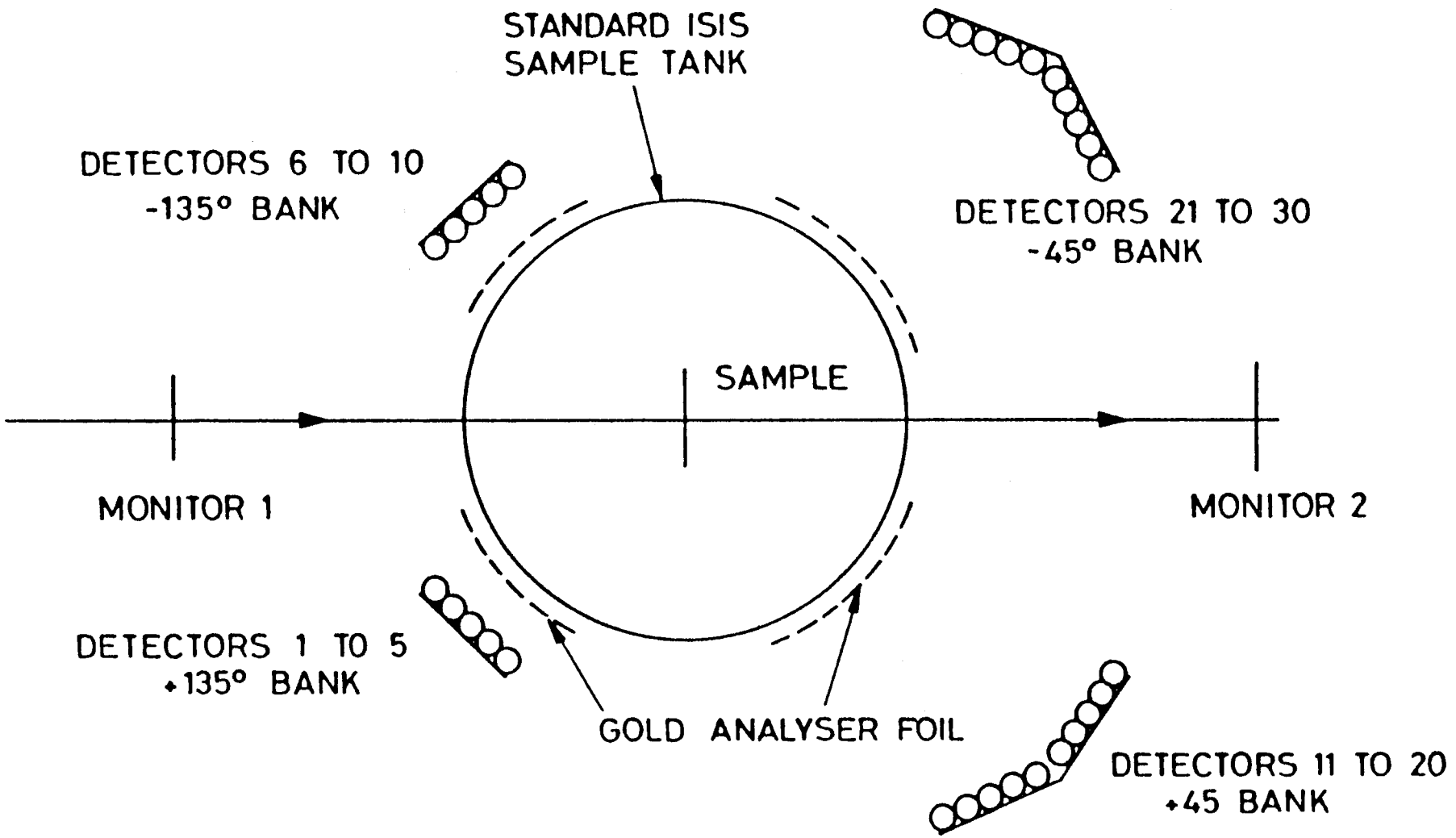

Figure 3.1 Layout of [illegible] during 1990.

2. The resonance must be well separated in energy from other resonance energies. Otherwise the instrument simultaneously detects neutrons at two different values of E_1 and features from the two different detection energies may overlap in the data, making interpretation difficult.

3. Not too high an energy ($< 50eV$). Otherwise the accuracy with which the neutron time of flight can be measured starts to dominate the energy resolution of the instrument. Higher energies require longer flight paths and hence lower count rates for good resolution.

A gold foil has been used almost exclusively on EVS so far. Although the gold resonance at $4.906eV$ has a relatively broad intrinsic width compared to resonances of suitable energy in Ta and U, the next resonance does not occur until $60.3eV$, so that overlap effects from different resonances are absent. This is particularly advantageous for scattering from hydrogen, where overlap effects are particularly troublesome with a Tantalum analyser and where the resolution of the Au filter is adequate for measurement of the H momentum distribution. However for other systems Tantalum and Uranium are also potentially useful.

In figure 3.2 we show time of flight scans in q, ω space available on the eVS forward angle banks with a gold foil analyser. The shaded region is bounded by the FWHM of the response from a hydrogen atom in zirconium hydride which has a momentum distribution with a FWHM of $9\mathring{A}^{-1}$. In figure 3.3 we show a similar plot for the forward and backward banks for scattering from Li, and in figure 3.4 for scattering from Pb. The energy and momentum transfers available on resonance filter spectrometers are much greater than those attainable on any other neutron instrument. It can be seen from figure 3.2 that on EVS, for H scattering, $1.2 < \omega < 14$ eV and $30 < q < 80\mathring{A}^{-1}$, while for $M > 2$, $\omega \simeq 30$eV and $q \simeq 90\mathring{A}^{-1}$. At such high energy and momentum transfers corrections to the IA are small, as we show in section 8.

4 Instrument Calibration

The instrumental parameters L_0,L_1,E_1,θ and t_0, defined in section 2.3 must be determined by a calibration of the instrument. Any errors in these parameters will lead to systematic errors in the calculation of y and $J(y)$ from experimental data. The sensitivity of EVS is such that even small deviations from the IA can be measured accurately, so a very accurate calibration of the instrument parameters is required. In this section we present the calibration procedure for EVS in some detail.

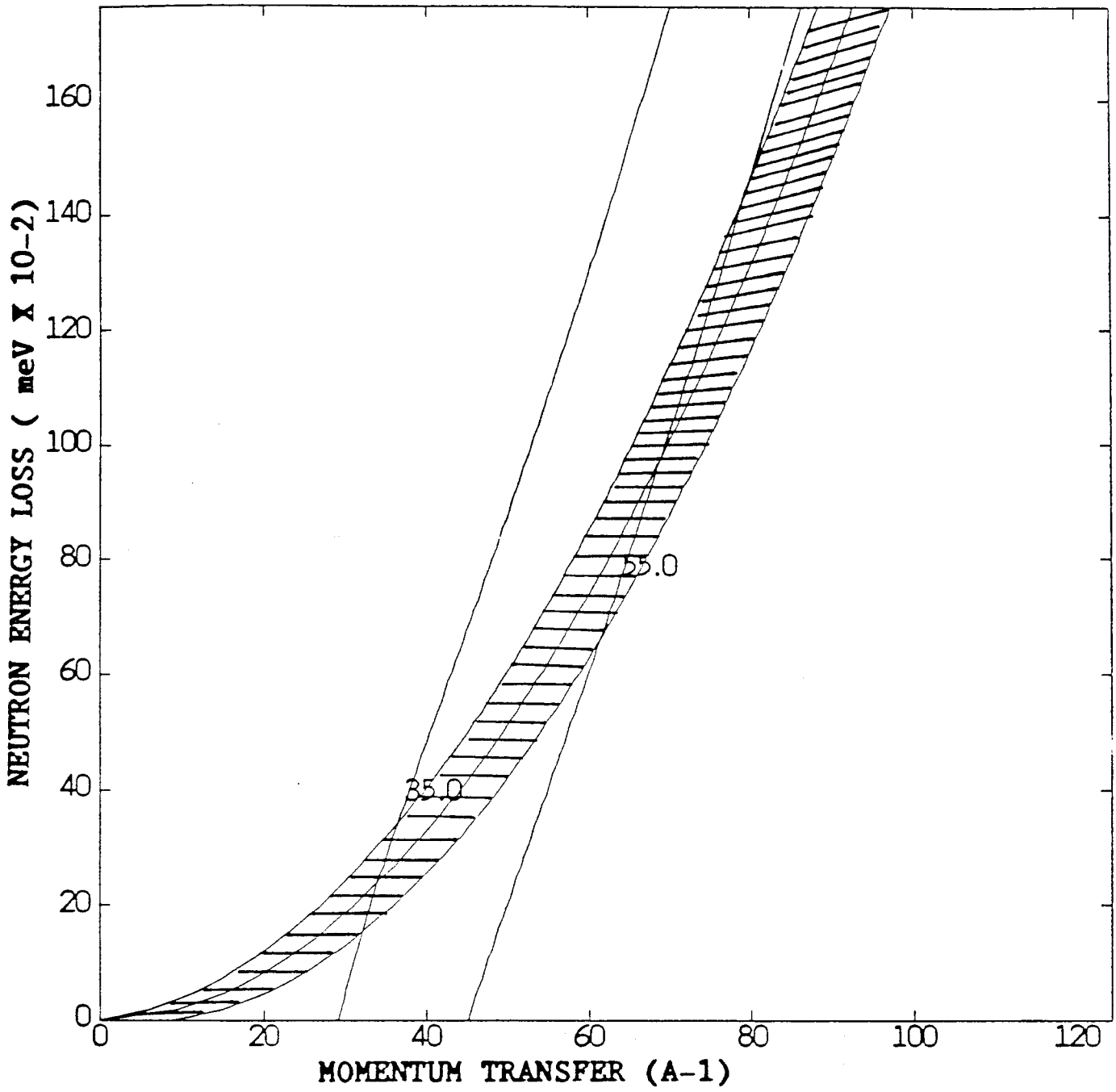

Figure 3.2 The boundary of the shaded area denotes the HWHM of $S(q,\omega)$ for scattering from the protons in zirconium hydride. The left hand line crossing the shaded area is a time of flight scan on EVS at scattering angle of 35°, the right hand line at 55°. Scans on the forward angle banks on EVS lie between these limits.

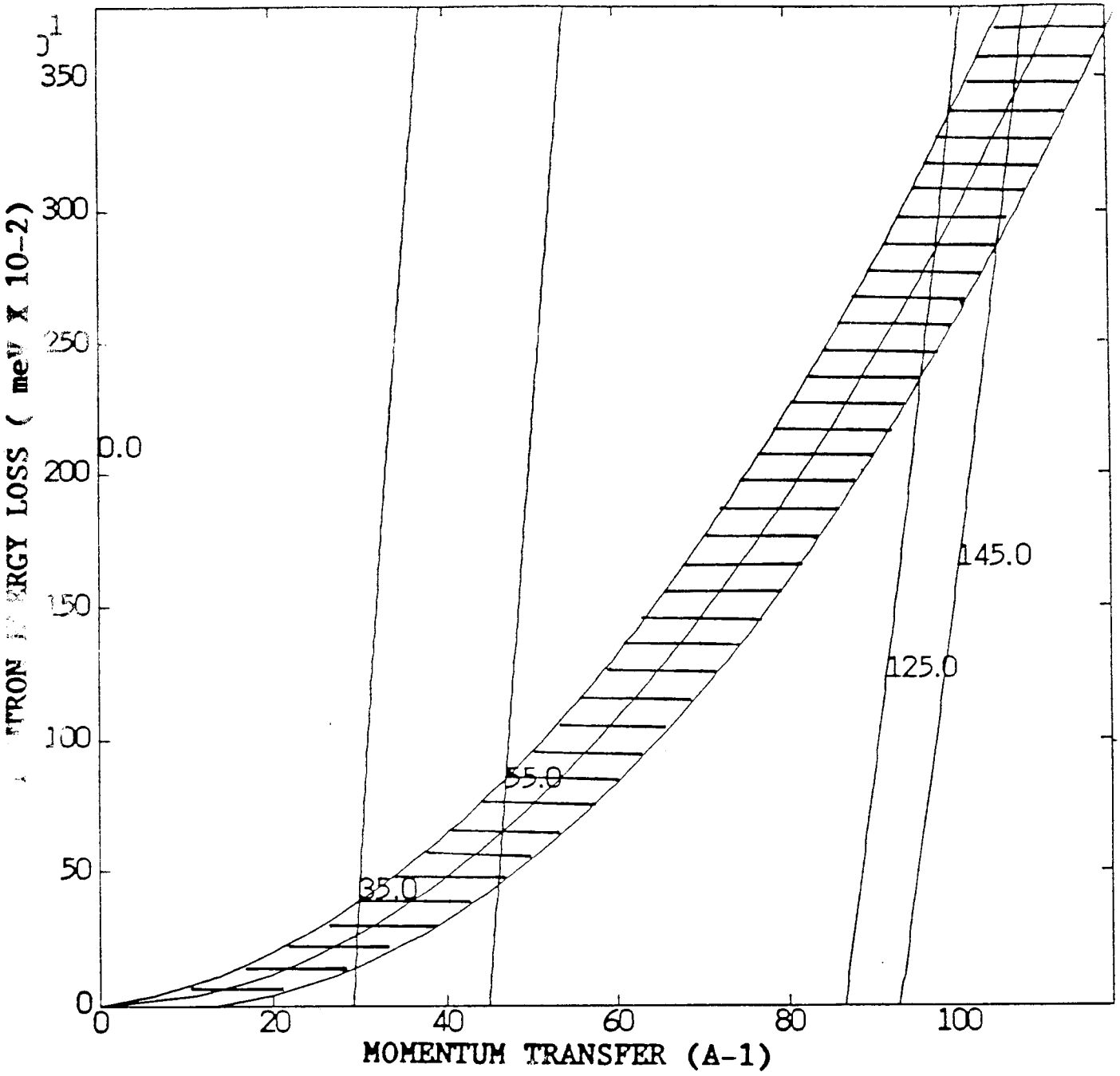

Figure 3.3 The boundary of the shaded area is the HWHM of $S(q,\omega)$ for lithium at 290K. The lines crossing the shaded area are time of flight scans at angles of 35°,55°,125° and 145°. The 45° bank scans lie between 35° and 55° and the 135° bank scans between 125° and 140°.

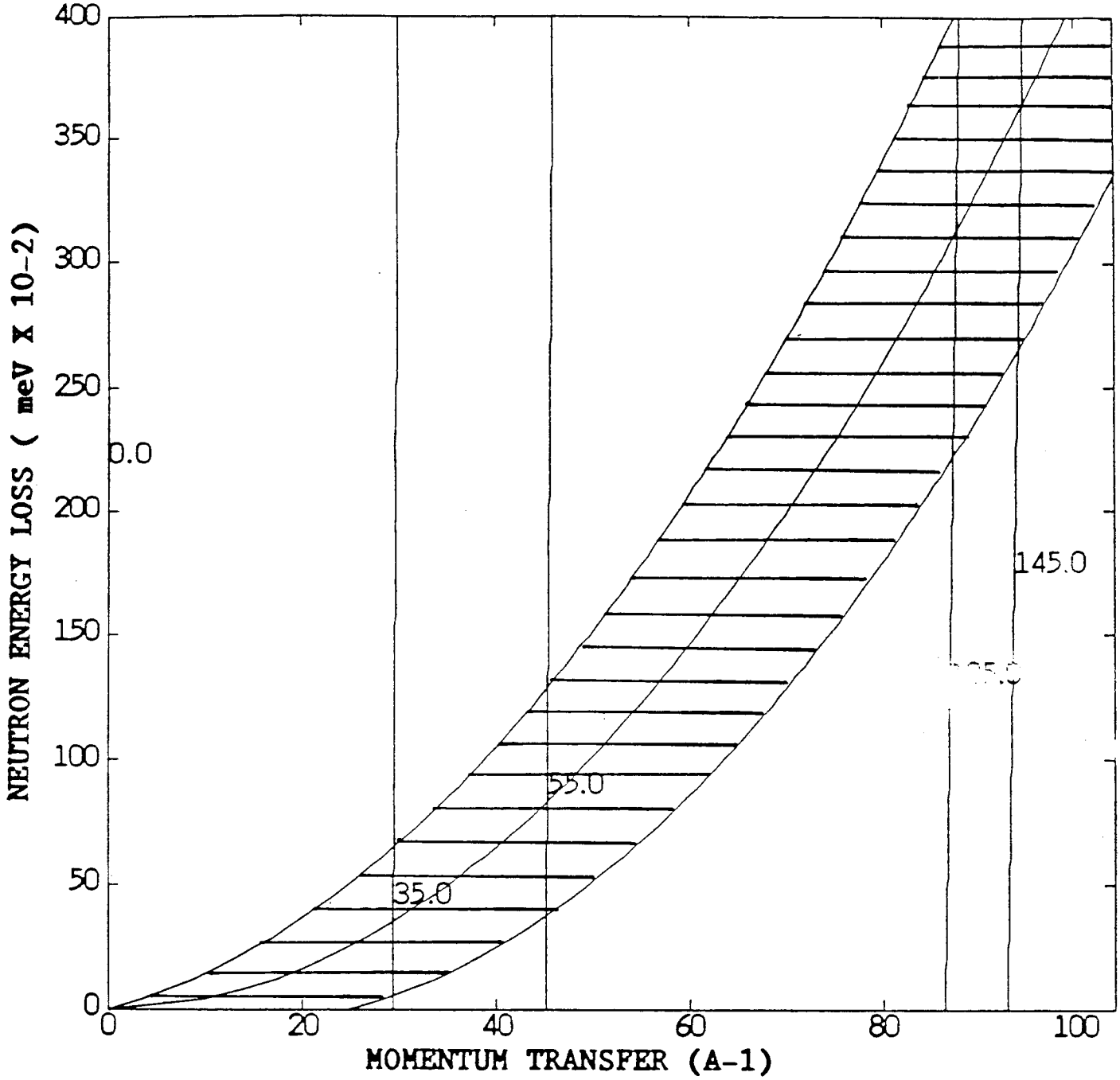

Figure 3.4 The boundary of the shaded area is the HWHM of $S(q,\omega)$ for vanadium at 290K. The lines crossing the shaded area are time of flight scans at angles of 35°.55°.125° and 145° respectively from left to right. The 45° bank scans lie between 35° and 55° and the 135° bank scans between 125° and 140°.

4.1 Length Calibration

The scattered flight paths L_1 were measured using a meter rule. The distance from the centre of the sample to the detector centre was 0.5 ± 0.005 metres for the 135° banks and 0.875 ± 0.005 metres for the 45° banks. The quoted error of $\pm 5mm$ is a generous estimate of the measurement error. The total distance $L = L_0 + L_1$, from the moderator to the detector and the time constant t_0 can be determined from the positions of uranium resonance absorption peaks in the time of flight spectra. The energies of these peaks, which are very accurately known and the corresponding neutron velocities, are given in table 4.1.

Table 4.1 Energy of Resonance Absorption Peaks In Uranium

$E_R(meV)$	$V_R(m/sec)$
6671±2	35722±5
20872±6	63187±9
36680±11	83765±13
66020±20	112379±17
102540±30	140053±20
189670±40	190479±20

A uranium foil was placed in the incident beam and the scattering spectrum from a Pb sample at room temperature was collected. If the scattering from the sample is strictly elastic then the resonance absorption peak occurs in the time of flight spectrum at

$$t = \frac{L}{V_R} + t_0 \tag{27}$$

However there is some inelasticity in the scattering due to the recoil of the Pb atoms. At the high neutron energies used in the calibration, the scattering from Pb at room temperature is well described by the impulse approximation. Thus the ratio of the final and incident velocities of the scattered neutrons is determined by equation 9 and equation 27 must be modified to

$$t = \frac{\left(L_0 + \frac{L_1}{\alpha}\right)}{V_R} + t_0 = \frac{L}{V_R} + \left(\frac{L_1}{V_R}\right)\left(\frac{1-\alpha}{\alpha}\right) + t_0 \tag{28}$$

The correction for inelasticity of the scattering from Pb makes a small ($\simeq 5mm$) difference to the calculated values of L. The values of L and t_0 were determined for each detector by performing a straight line least squares fit to equation 28, using the values of V_R in table 4.1. The resonance peak positions in t were determined by eye, using the cursor in the standard ISIS GENIE graphics package. The values of L and t_0 obtained from the fits, with standard errors, are given in table 4.2. From the measured values of L and L_1, L_0 can be calculated (see table 4.3). The mean of the L_0 values for the 30 detectors is 11.126 metres, with a standard deviation of 0.003 metres.

Table 4.2 Results of Si powder and U foil Calibrations

Detector	$L\sin(\theta/2)$ (metres)	L (metres)	$t_0(\mu sec)$
1	10.848±0.004	11.617±0.013	1.64±0.16
2	10.733±0.003	11.635±0.020	1.02±0.26
3	10.604±0.004	11.635±0.020	1.02±0.26
4	10.470±0.003	11.635±0.020	1.02±0.26
5	10.328±0.004	11.623±0.020	1.33±0.20
6	10.853±0.003	11.618±0.008	1.29±0.10
7	10.739±0.007	11.620±0.020	0.88±0.26
8	10.608±0.003	11.621±0.019	1.07±0.24
9	10.472±0.004	11.631±0.017	1.02±0.26
10	10.330±0.003	11.613±0.017	1.26±0.22
11	5.385±0.002	11.967±0.015	2.14±0.19
12	5.205±0.002	11.987±0.013	1.47±0.17
13	5.021±0.002	11.999±0.022	0.82±0.28
14	4.841±0.002	11.990±0.013	1.43±0.17
15	4.658±0.002	11.994±0.019	1.39±0.25
16	4.451±0.002	12.001±0.019	1.57±0.25
17	3.883±0.001	11.962±0.024	1.99±0.31
18	4.071±0.002	12.026±0.014	0.88±0.18
19	4.264±0.002	12.000±0.010	1.12±0.13
20	3.693±0.001	11.999±0.010	1.12±0.13
21	5.394±0.003	12.008±0.016	1.41±0.15
22	5.207±0.001	12.008±0.018	1.29±0.23
23	5.028±0.002	12.033±0.017	0.96±0.23
24	4.842±0.002	12.023±0.014	1.00±0.17
25	4.662±0.001	12.033±0.017	1.18±0.22
26	4.469±0.001	12.007±0.012	1.41±0.15
27	4.280±0.002	12.007±0.012	1.41±0.15
28	4.094±0.002	12.007±0.012	1.41±0.15
29	3.904±0.002	12.029±0.018	0.24±0.23
30	3.711±0.002	11.969±0.020	1.32±0.27
31		8.57±0.05	−0.87±0.62
32		13.38±0.06	−0.24±0.90

Table 4.3 Calibrated Instrument Parameters with Errors

Detector	L_0 (metres)	L_1 (metres)	θ (degrees)	$t_0(\mu sec)$
1	11.117±0.014	0.500±0.005	138.07±0.35	1.64±0.16
2	11.135±0.021	0.500±0.005	134.58±0.48	1.02±0.26
3	11.135±0.021	0.500±0.005	131.39±0.45	1.02±0.26
4	11.135±0.021	0.500±0.005	128.28±0.41	1.02±0.26
5	11.123±0.021	0.500±0.005	125.39±0.39	1.33±0.20
6	11.118±0.009	0.500±0.005	138.18±0.22	1.29±0.10
7	11.120±0.021	0.500±0.005	135.09±0.51	0.88±0.26
8	11.121±0.020	0.500±0.005	131.80±0.42	1.07±0.24
9	11.131±0.021	0.500±0.005	128.40±0.42	1.02±0.26
10	11.113±0.018	0.500±0.005	125.62±0.33	1.26±0.22
11	11.092±0.016	0.875±0.005	53.49±0.08	2.14±0.19
12	11.112±0.014	0.875±0.005	51.47±0.06	1.47±0.17
13	11.124±0.023	0.875±0.005	49.47±0.10	0.82±0.28
14	11.115±0.014	0.875±0.005	47.62±0.06	1.43±0.17
15	11.119±0.020	0.875±0.005	45.71±0.08	1.39±0.25
16	11.126±0.020	0.875±0.005	43.54±0.07	1.57±0.25
17	11.087±0.025	0.875±0.005	37.88±0.08	1.99±0.31
18	11.151±0.015	0.875±0.005	39.57±0.05	0.88±0.15
19	11.125±0.011	0.875±0.005	41.62±0.04	1.12±0.13
20	11.124±0.011	0.875±0.005	35.85±0.03	1.12±0.13
21	11.133±0.017	0.875±0.005	53.38±0.08	1.41±0.15
22	11.133±0.019	0.875±0.005	51.40±0.08	1.29±0.23
23	11.158±0.018	0.875±0.005	49.40±0.08	0.96±0.23
24	11.148±0.015	0.875±0.005	47.50±0.06	1.00±0.17
25	11.158±0.018	0.875±0.005	45.59±0.07	1.18±0.22
26	11.132±0.013	0.875±0.005	43.70±0.05	1.41±0.15
27	11.132±0.013	0.875±0.005	41.77±0.05	1.41±0.15
28	11.132±0.013	0.875±0.005	39.87±0.05	1.41±0.15
29	11.154±0.019	0.875±0.005	37.87±0.06	0.24±0.23
30	11.094±0.021	0.875±0.005	36.12±0.07	1.32±0.27

4.2 Angle Calibration

The scattering angles were determined by scattering from a silicon powder sample. The peaks in the powder pattern occur at time of flight values determined by Bragg's law

$$2d\sin\left(\frac{\theta}{2}\right) = \lambda = 3.9554 \times 10^{-3}\frac{(t - t_0)}{L} \tag{29}$$

where d is the spacing of the Bragg reflection planes in $\AA$, l is the neutron wavelength in $\AA$ and t is the time of flight in μsec. The time of flight t of the (111), (220), (311),

(400), (331) and (422) peaks was determined by eye, using the GENIE cursor. From equation 29, the accurately known values of d and the values of t_0 obtained from the fit to U resonances, a value of $L \sin\left(\frac{\theta}{2}\right)$ was calculated for each of the 6 peaks. The mean of these 6 values, with standard error is given for each detector in table 4.2. From the calibrated values of $L \sin\left(\frac{\theta}{2}\right)$ and L, the values of θ given in table 4.3 were calculated.

4.3 Energy of Analyser Foil

In most measurements described in this report a gold analyser foil was used. This has a resonance absorption peak at a nominal energy of $E_1 = 4906 \pm 10meV$. Since the energies of the uranium resonance peaks are known much more accurately than those of gold, the calibrated instrument parameters were used to determine the energy of the Au resonance. This procedure is also necessary for the internal consistency of the calibration. The foil was inserted in the incident beam and Lorentzian fits to time of flight spectra were made, to determine the positions of the peak. The neutron energy corresponding to the peak position was calculated from the calibrated instrument parameters for each detector. The recoil of the sample atoms was taken into account as in section 3.1. In table 4.4 we give the mean energies calculated from the detectors in the forward and backward angle banks from measurements on Pb and V samples. The mean of all the measurements is $E_1 = 4922 \pm 1meV$.

Table 4.4 Energy of Gold Foil Resonance

Sample	Detector numbers	E_1 (meV)	Angular Range
Pb	1-10	4918±2	35°-55°
Pb	11-30	4925±2	125°-138°
V	1-10	4922±2	35°-55°
V	11-30	4921±2	125°-138°

4.4 Incident Beam Intensity

The incident beam intensity $I(E_0)$ is required for the calculation of $J(y)$ from the time of flight spectrum via equation 21. The time of flight spectrum in the incident beam monitor was transformed to E_0 using the standard GENIE routines. A least squares fit to

$$I(E_0) = \frac{A}{{E_0}^n} \tag{30}$$

gave $n = 1.380$ for the incident beam monitor and $n = 1.405$ for the transmitted beam monitor. The spectrum and fit to the incident beam monitor spectrum are shown in figure 4.1. It can be seen that the functional form of equation 30 describes the

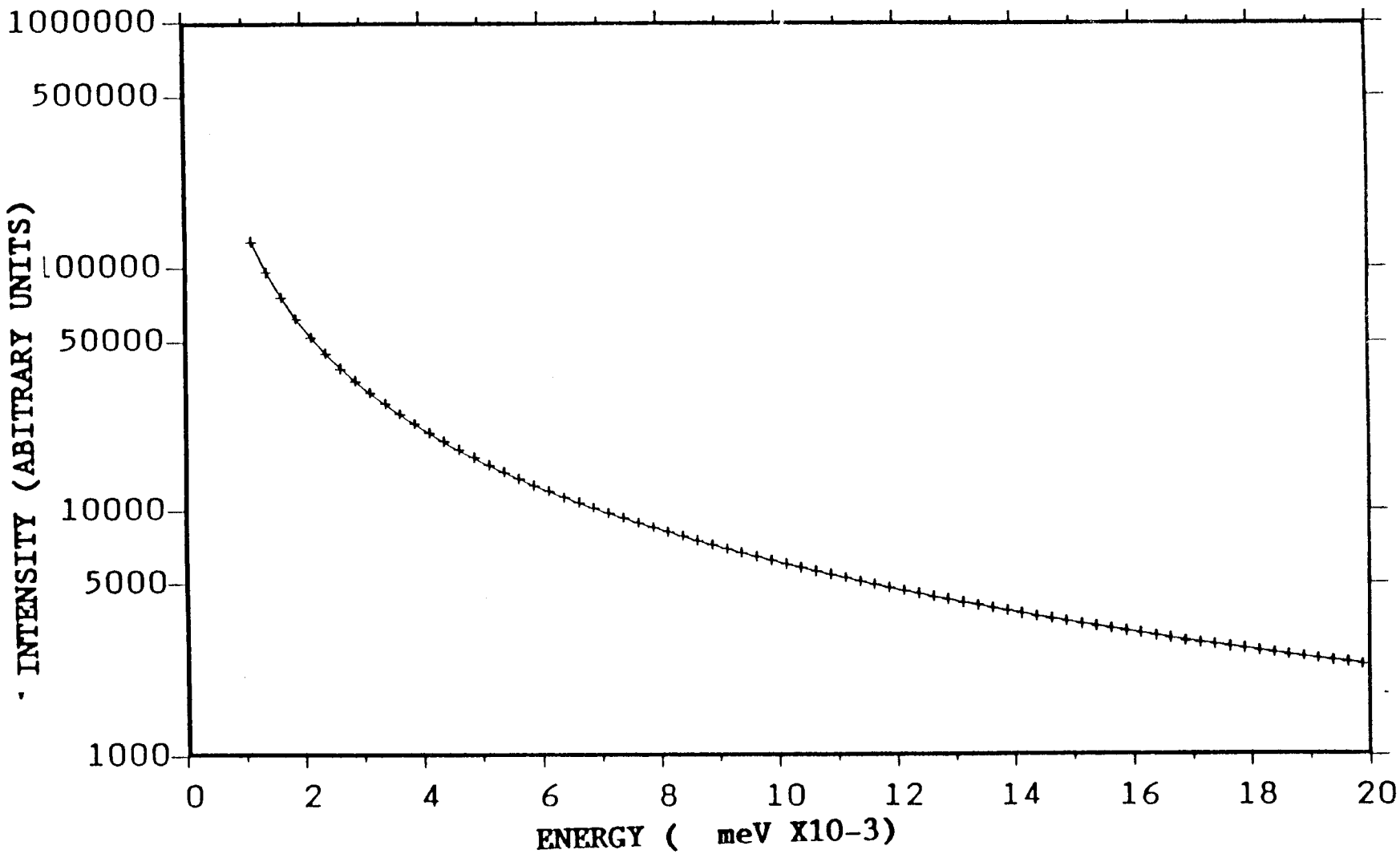

Figure 4.1 Fit to the spectrum in the incident beam monitor. Crosses are the detected intensity, line is the fit to A/E^n, with n=1.38.

spectrum extremely well. After correction for the efficiency of the monitor ($\propto E^{-\frac{1}{2}}$) we obtain $I(E_0) \propto E^{-0.9}$. This agrees very well with the predicted incident spectrum [11].

5 Instrument Resolution

In any measurement the detected neutrons sample distributions of instrument parameter values about the mean values. The form of these distributions determine the resolution function of the instrument in y space. There are five independent contributions to the y resolution, corresponding to the 5 instrument parameters.

1. The energy resolution ΔE_1 of the instrument. With a gold foil this is always the dominant contribution.
2. The angular resolution. In a single detector there is a distribution of scattering angles due to the finite size of the detector and sample. This contribution is small except for scattering from hydrogeneous systems.
3. There is a distribution of L_0 values caused essentially by the depth of the neutron moderator. This contribution is always small compared to that from ΔE_1.
4. A distribution of L_1 values due to the finite sample width and detector depth. This contribution to the resolution is larger than that from ΔL_0, but small compared to that from ΔE_1.
5. The uncertainty in the time of flight due to the finite width of the time bins, Δt. We choose Δt so that this effect is negligible.

We first discuss the angular and length contributions to the resolution, as these are required for the precise measurement of the energy contribution.

5.1 Angular Resolution

The angular resolution of the forward angle detectors can be determined from the peak shape of powder diffraction peaks, as for $\theta < 60°$, the shape of powder peaks is dominated by the angular resolution. From equation 29 we obtain

$$\Delta\theta = 2\tan\left(\frac{\theta}{2}\right)\frac{\Delta\theta}{\theta} = 2\tan\left(\frac{\theta}{2}\right)\frac{\Delta t}{t} \tag{31}$$

In table 5.1 we list the positions and standard deviations of Gaussian fits to the silicon (111) powder peak and the corresponding standard deviation of the angular

distribution calculated from equation 31. A typical fit is shown in figure 5.1. It can be seen that the distribution in t and therefore in θ is well approximated by a Gaussian form.

$$f(\theta) \propto \exp\left(\frac{-(\theta-\theta_0)^2}{(2\sigma_\theta{}^2)}\right) \tag{32}$$

The small deviation from Gaussian behaviour is caused by the time structure of the pulse of neutrons. This introduces asymmetries and slightly broadens the peak. We note that the fitted widths therefore slightly overestimate the width of the angular distribution of scattered neutrons. The results in table 5.1 show that σ_θ slowly increases as θ gets smaller. This is a geometrical effect introduced because the detector is straight rather than curved, so that it does not lie precisely on the cone defined by scattering angle θ_0. The scattering angle at the ends of the detector is thus slightly different from that at the centre. This effect is a maximum at $\theta = 0$ and $\theta = 180°$ and absent for $\theta = 90°$. However this is a small effect ($\simeq 0.02°$) and the angular resolution of the detectors in the forward angle bank is well approximated by $\sigma_\theta = 0.58° \pm 0.02°$.

The angular resolution of the backward angle banks cannot be measured so directly, as the angular and time components of the Bragg peak resolution function are comparable for backscattering. However the angular component of the y resolution is relatively unimportant for backscattering and a precise measurement of σ_θ is not so necessary. We assume that σ_θ scales linearly with distance, so that for backscattering $\sigma_\theta = 0.58 \times 0.875/0.50 = 1.02°$. The only inaccuracy in this assumption is caused by changes in the small effects mentioned above, due to the detector not lying on the scattering cone.

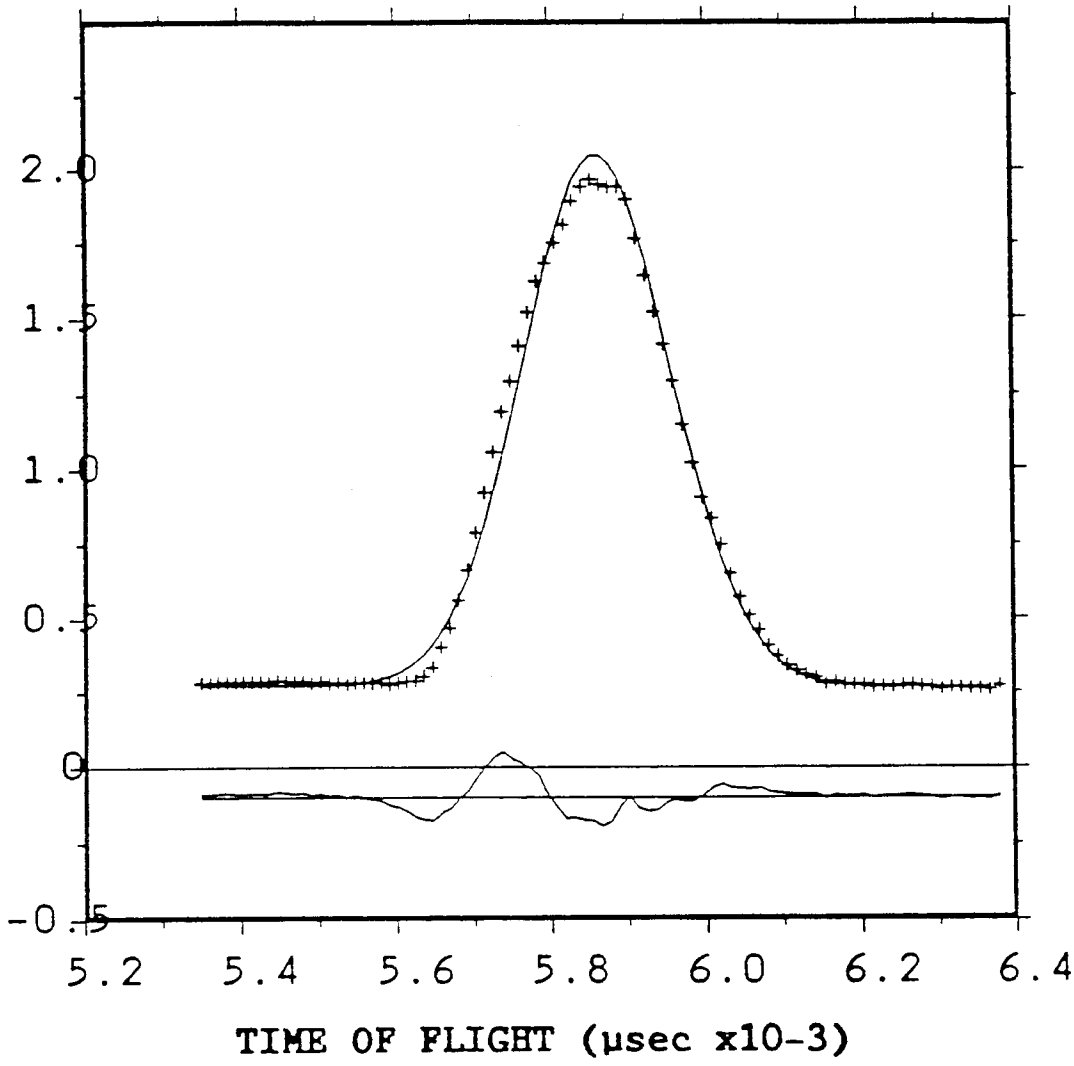

Figure 5.1 Gaussian fit to silicon powder (111) peak for spectrum 20.

Table 5.1 t is the peak position and Δt the standard deviation obtained from gaussian fits to a silcon powder (111) peak. θ_0 is the scattering angle and σ_θ the standard deviation of the angular resolution function obtained from equations 31 and 32.

Spectrum	$t(\mu sec)$	$\Delta t(\mu sec)$	θ_0(degrees)	σ_θ(degrees)
11	8532	81.4	53.49	0.551
12	8247	84.6	51.47	0.566
13	7956	84.4	49.47	0.560
14	7671	85.5	47.62	0.564
15	7381	87.4	45.71	0.572
16	7052	89.3	43.54	0.580
17	6154	95.4	37.88	0.610
18	6454	93.2	39.57	0.595
19	6753	92.1	41.62	0.594
20	5853	95.3	35.85	0.603
21	8540	87.2	53.38	0.588
22	8253	83.2	51.40	0.556
23	7965	84.3	49.40	0.557
24	7673	87.3	47.50	0.574
25	7384	88.1	45.59	0.575
26	7078	87.2	43.70	0.566
27	6782	91.4	41.77	0.589
28	6486	95.3	39.87	0.611
29	6183	93.4	37.87	0.594
30	5884	95.2	36.12	0.605

5.2 Instrument Length Effects

In the epithermal region, the pulse shape from the moderator is of the form [11]

$$\phi(t) = C(vt)^2 \exp(-\beta vt) \tag{33}$$

where v is neutron velocity, t is time of flight and C and β are constants. This distribution of flight times can be interpreted as being caused by a distribution of incident flight paths, ie

$$F(L_0) \propto (L_0 - < L_0 >)^2 \exp[-\beta(L_0 - < L_0 >)] \tag{34}$$

where $< L_0 >$ is the mean value of L_0. A Monte Carlo calculation of the of the pulse shape at $1eV$ [11] predicts a FWHM of $1\mu sec$. This correponds to $\beta = 246M^{-1}$ and a HWHM of $0.7cm$ for $F(L_0)$.

The uncertainty in the final flight path can be estimated from the diameter of the ^{3}He detector ($2.5cm$) and the diameter of the beam ($3cm$). With a plane slab

sample pependicular to the beam, the distribution of final flight paths L_1 can be approximated as a Gaussian with a standard deviation of $1.5cm$.

Although the flight path uncertainties cannot be measured directly they have a small effect on the instrument resolution for all atomic masses compared to the component from the gold foil analyser. Thus errors in the estimation of ΔL_0 and ΔL_1 and the approximation of equation 34 by a Gaussian function should have little effect on the calculated instrumental resolution in y space.

5.3 Calibration of Energy Component of Resolution

The energy component of the resolution in y space was calibrated by scattering measurements from polycrystalline lead, vanadium, aluminium and lithium samples. We assumed that the momentum distribution of atoms in these materials could be calculated in the harmonic model, using the Debye approximation for the density of states as in section 2.2. The measured neutron Compton profile, $J_m(y)$, is a convolution of the gaussian contribution from the intrinsic momentum distribution $J(y)$ with the various resolution contributions.

$$J_m(y) = J(y) * R_\theta(y) * R_L(y) * R_E(y) \tag{35}$$

where $R_\theta(y)$ is the angular, $R_L(y)$ the length and $R_E(y)$ the energy component of the resolution in y space. Since we assume that $J(y)$,$R_\theta(y)$ and $R_L(y)$ are gaussians,

$$J_m(y) = J_b(y) * R_E(y) \tag{36}$$

where $J_b(y) = J(y) * R_\theta(y) * R_L(y)$ is a gaussian. The width of $J_b(y)$ can be calculated by summing in quadrature the widths of $R_\theta(y)$ and $R_L(y)$ and the calculated width of $J(y)$. Typical values for the various components are given in table (5.2). It can be seen that $J_b(y)$ is only slightly broadened by the angular and length components of the resolution.

Table 5.2 σ, σ_θ and σ_L are the standard deviations of the Gaussians $J(y)$,$R_\theta(y)$ and $R_L(y)$ respectively. $\sigma_b = [\sigma^2 + {\sigma_\theta}^2 + {\sigma_L}^2]^{\frac{1}{2}}$ is the standard deviation of $J_b(y)$. σ_E is the HWHM of the Lorentzian component of the resolution.

Sample	σ_E $\AA^{-1}$	σ_b $\AA^{-1}$	σ $\AA^{-1}$	σ_θ $\AA^{-1}$	σ_L $\AA^{-1}$
Pb	231	40.6	35.3	0.46	20.0
V	60.3	18.9	18.2	0.46	4.95
Al	29.2	13.6	13.3	0.46	2.64
Li	8.36	6.8	6.74	0.46	0.70

The energy resolution function is

$$R(E_1) = 1 - T(E_1) \tag{37}$$

where $T(E_1)$ is the transmission of the foil. It is found empirically that $R(E_1)$ is well approximated by a Lorentzian function,

$$R(E_1) = \frac{constant}{[(E_R - E_1)^2 + \Delta E^2]} \tag{38}$$

The energy component of the resolution function in y space is also well approximated by a Lorentzian function

$$R_E(y) = \frac{constant}{[y^2 + {\sigma_E}^2]} \tag{39}$$

where ΔE is related to σ_E via

$$\Delta E \simeq \sigma_E \left(\frac{\partial E_1}{\partial y} \right)_{y=0} \tag{40}$$

Thus, from equations 36 and 39, $J_m(y)$ is a convolution of a Gaussian and a Lorentzian (known as a Voigt function). The measured spectra in y space were fitted to a Voigt function with a Gaussian component of fixed width σ_b, to determine σ_E for each detector. The corresponding ΔE for each detector was calculated using equation 40. (A typical fit to lead data is shown in figure 5.2. Note that for lead the gaussian component has a negligible effect and $J_m(y)$ is almost Lorentzian.) The mean values of ΔE calculated from the 20 detectors at forward angles is given in table 5.3 for various calibration runs. The quoted error is the standard deviation of the values from the 20 detectors.

Table 5.3 Mean values of ΔE for detectors in 45° bank

Element	Run Number	$\Delta E(meV)$
Pb	843	146.7±1.4
V	887	153.8±0.7
V	894	153.7±1.2
V	955	151.6±0.5
Al	890	146.6±1.8
Al	963	148.7±1.3
Al	1053	151.7±1.5
Li	1048	151.0±2.6

The mean value for the energy resolution is $\Delta E = 150.5 \pm 1.0$. In figure 5.3 σ_E calculated from equation 40 using this mean value of ΔE is shown as a solid line, while the points are the fitted experimental values of σ_E for the different calibration samples. It can be seen that the energy component of the resolution function is well described by equation 40 and the single parameter $\Delta E = 150meV$ for all atomic masses between 7 and 207 amu.

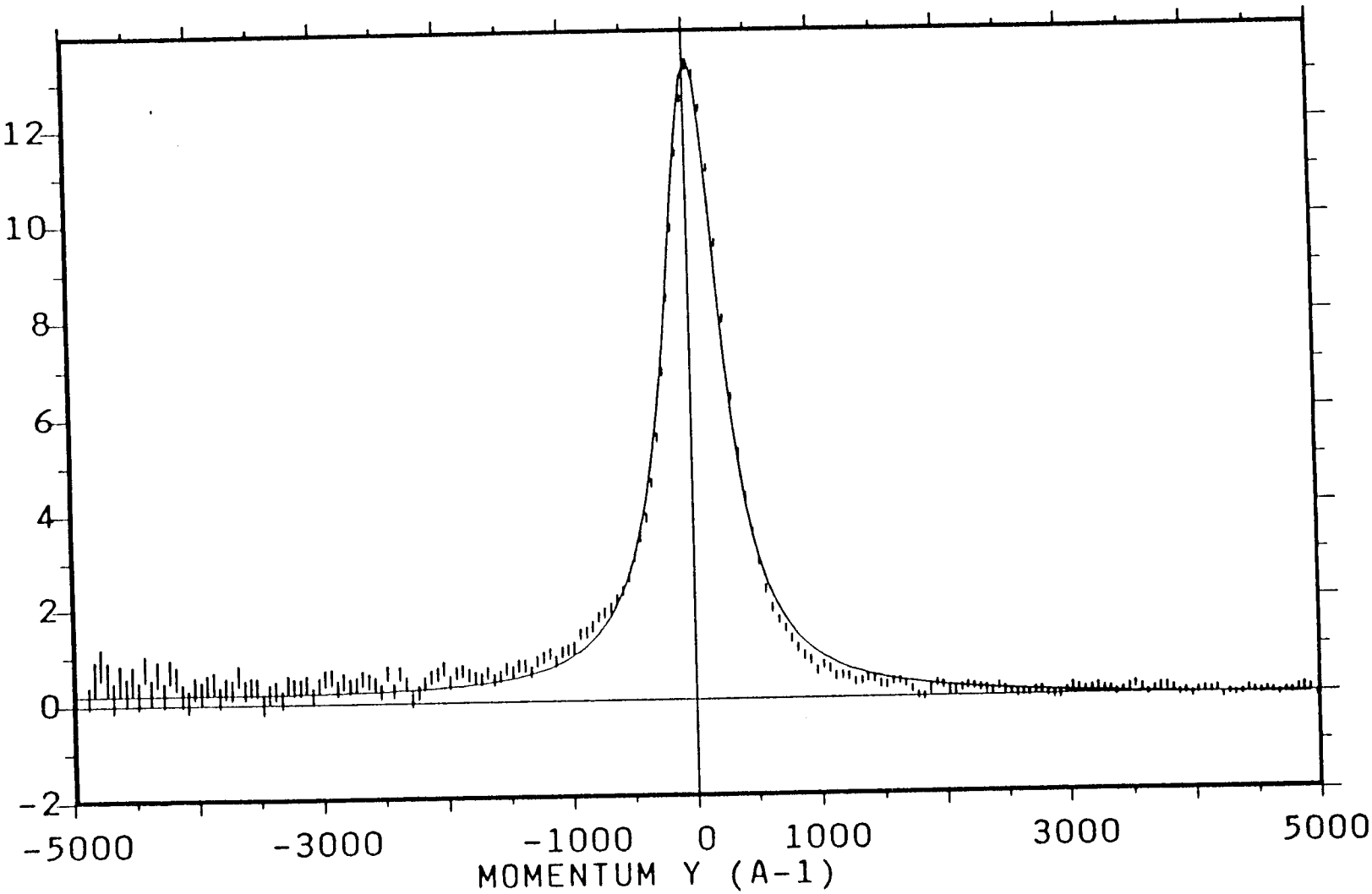

Figure 5.2 Voigt fit to the measured neutron Compton profile in lead at 290K.

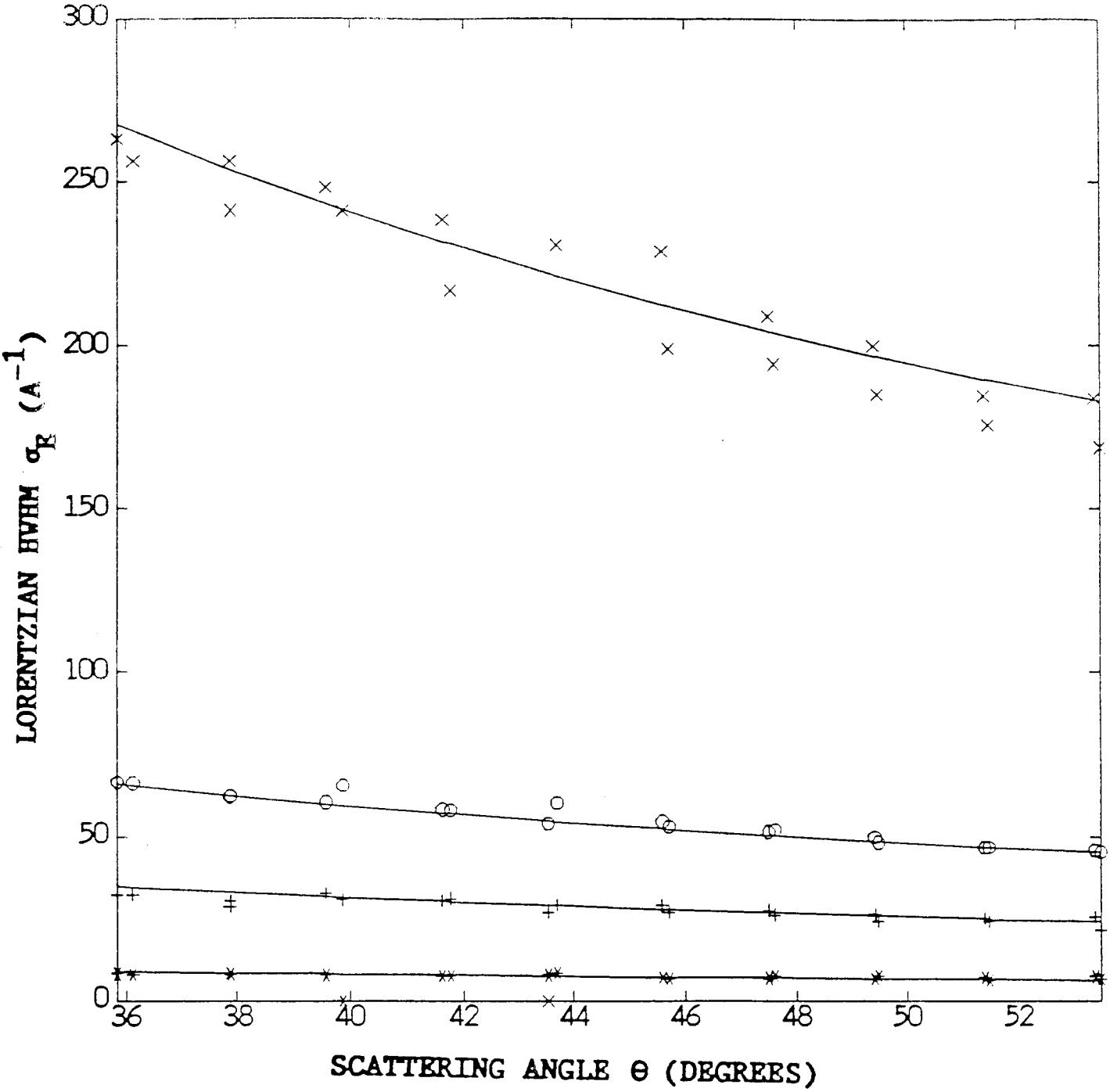

Figure 5.3 The points shown are the fitted values of σ_E obtained from individual spectra as a function of angle; x Pb, o V, + Al, * Li. The lines are calculated from equation 41 with $\Delta E = 150$ meV.

5.4 Calculation of Instrument Resolution

Analytic expressions for the different contributions to the resolution in y space are given in appendix 1. The parameters in tables 5.4 and 5.5, which are representative of the calibrated values of the instrument parameters and resolution widths for the $\pm 45°$ and $\pm 135°$ banks respectively, were used for the calculation of the resolution components in y.

Table 5.4 Instrument parameters and resolution widths for $\pm 45°$ banks

$L_0 = 11.127$ metres	$\Delta L_0 = 0.007$ metres
$L_1 = 0.875$ metres	$\Delta L_1 = 0.015$ metres
$\Delta\theta = 0.58°$	
$E_1 = 4922meV$	$\Delta E_1 = 150meV$

Table 5.5 Instrument parameters and resolution widths for the $\pm 135°$ banks

$L_0 = 11.127$ metres.	$\Delta L_0 = 0.007$ metres
$L_1 = 0.5$ metres	$\Delta L_1 = 0.015$ metres
$\Delta\theta = 1.03°$	
$E_1 = 4922meV$	$\Delta E_1 = 143meV$

In figure 5.4 we show the calculated resolution components as a function of angle for scattering from hydrogen and in figure 5.5 for scattering from lithium. In figure 5.6 we show calculations of the resolution components for lithium in the backward angle banks. The lines are the standard deviations of the gaussian widths for the angular (σ_θ) and length (σ_1 and σ_0) components and the HWHM of the Lorentzian for the energy (σ_E) component of resolution. The resolution is entirely dominated by the energy component for backscattering. The angular term is significant for scattering from hydrogen, but the energy component still dominates the resolution of EVS at all available angles in the $\pm 45°$ banks.

6 Data Analysis

We outline the basic data analysis procedure currently being used on EVS for samples in which there is no preferred direction, eg powders or liquids. At present the analysis is limited to the extraction of the mean atomic kinetic energy. We anticipate that as the stability and sensitivity of EVS improves, the data analysis procedures will be refined further to allow for peak shape analysis.

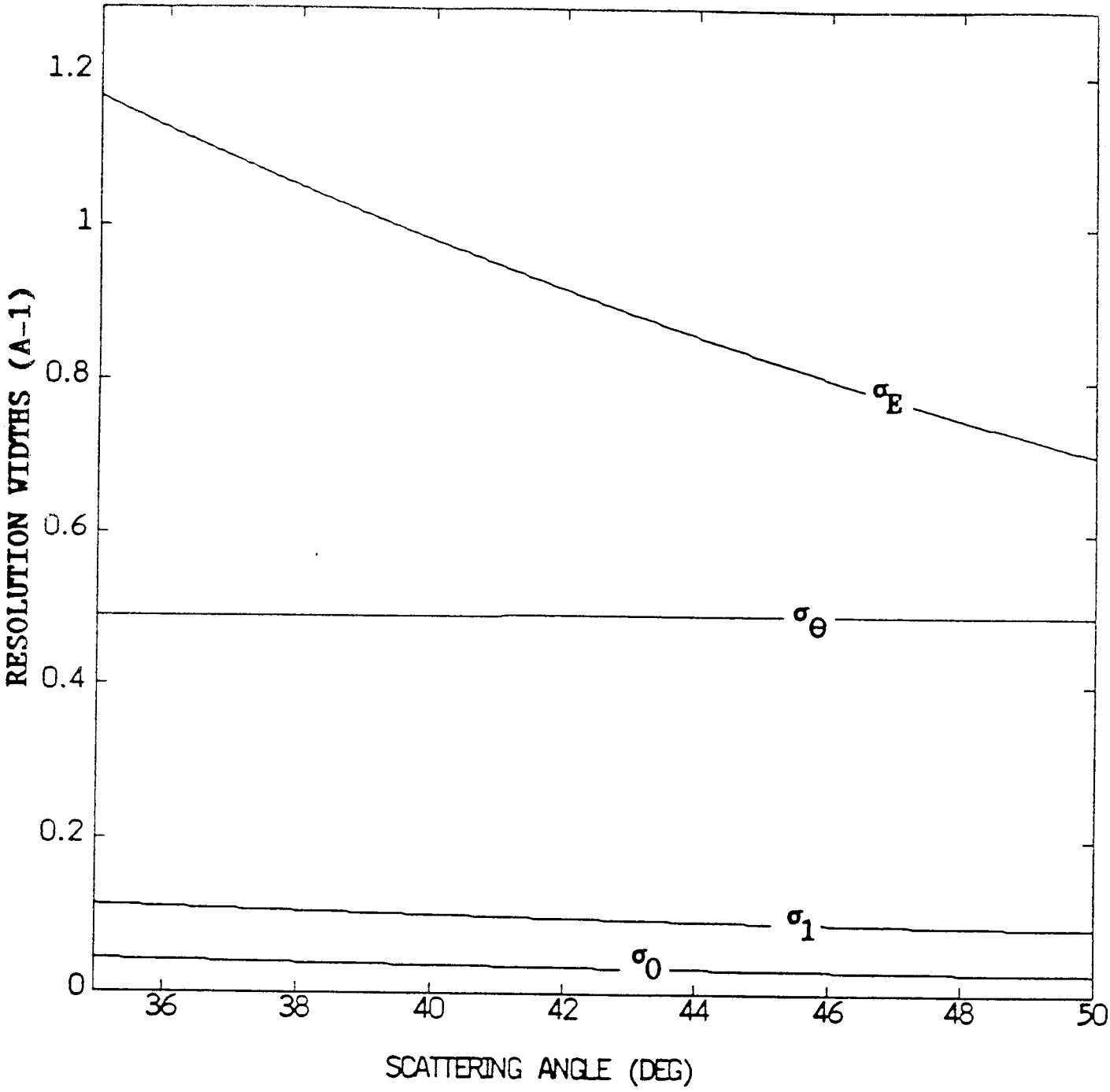

Figure 5.4 Calculated resolution components of EVS in the $\pm 45°$ banks for hydrogen scattering. The instrument parameters used in the calculation were taken from table 5.4. The different resolution components shown are

$$\sigma_E = (\partial y/\partial E)\Delta E \quad \sigma_\theta = (\partial y/\partial \theta)\Delta\theta$$
$$\sigma_0 = (\partial y/\partial L_0)\Delta L_0 \quad \sigma_1 = (\partial y/\partial L_1)\Delta L_1$$

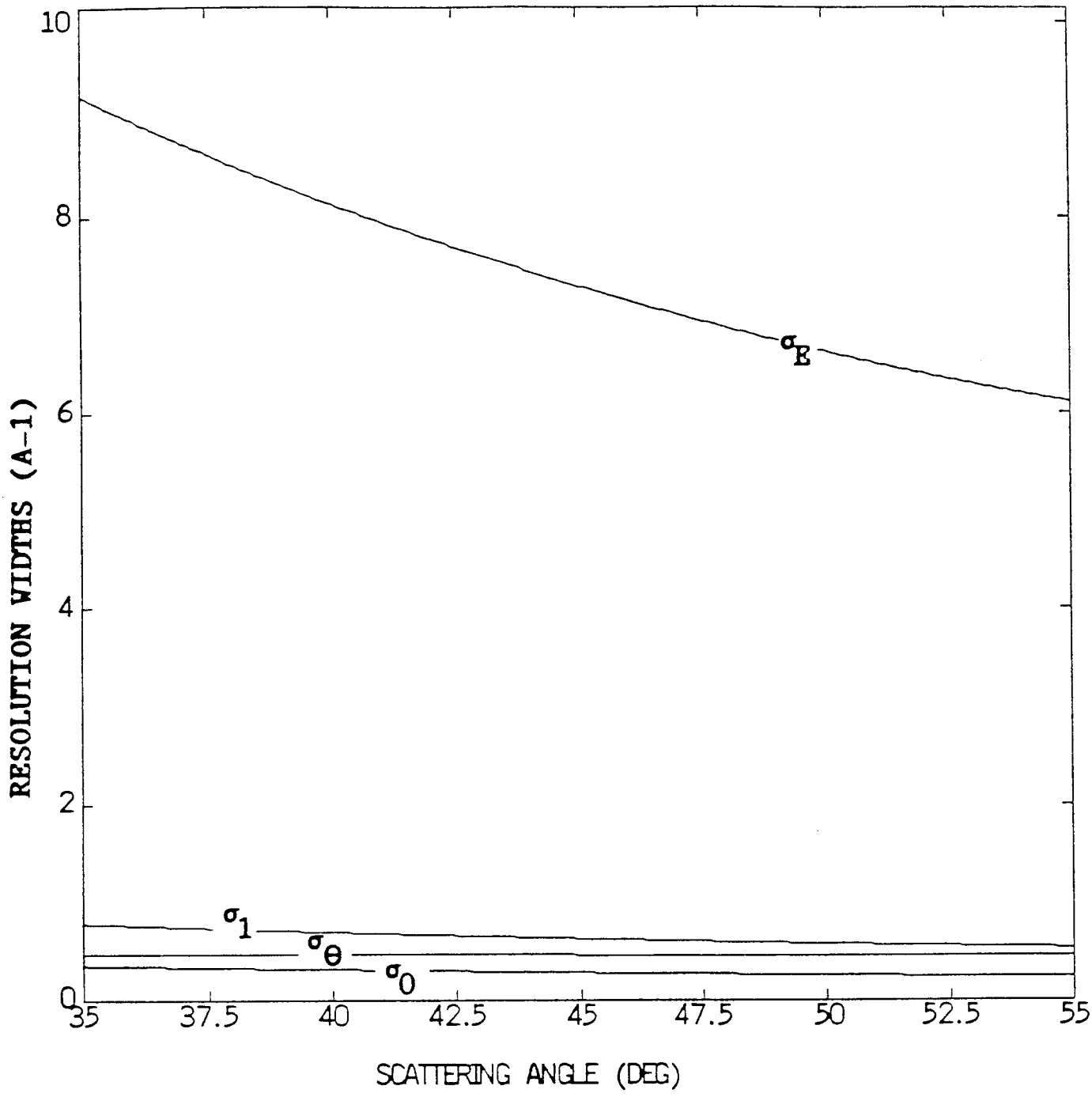

Figure 5.5 Calculated resolution components of EVS in the $\pm 45°$ banks for lithium scattering. The instrument parameters used in the calculation were taken from table 5.4.

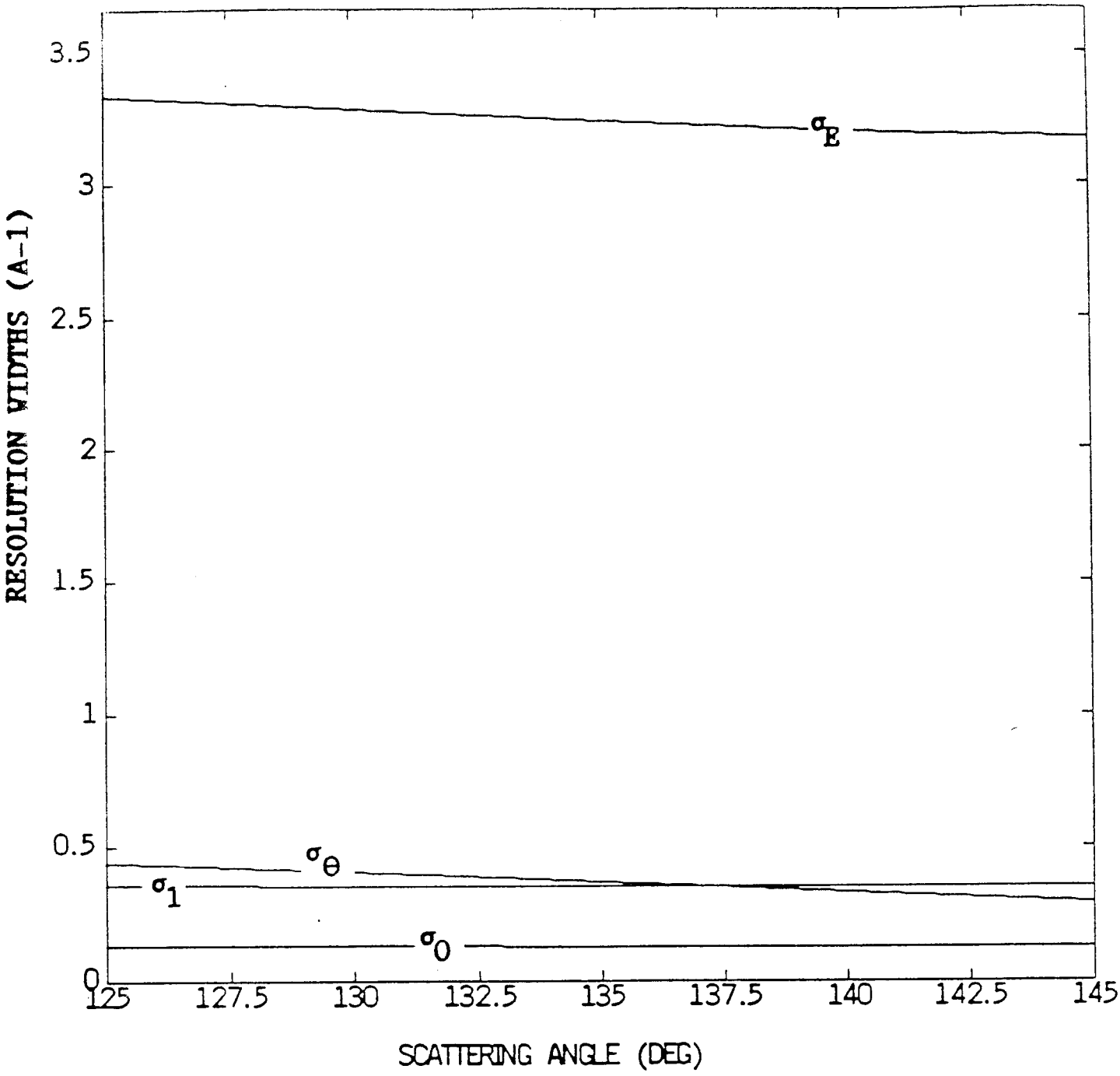

Figure 5.6 Calculated resolution components of EVS in the $\pm 135°$ banks for lithium scattering. The instrument parameters used in the calculation were taken from table 5.5.

6.1 Obtaining 'Raw' Data

As discussed in section 3, EVS uses the filter difference method to define the energy of the scattered neutron. The 'raw' data is the difference, (filter-out) - (filter-in). In figure 6.1 we show the time of flight spectrum collected on detector 11 ($\theta = 55°$) from a filter-out run on zirconium hydride, together with an 8th order polnomial fit. The filter-out spectrum is generally a smooth function and polynomial fitting allows for a short filter-out spectrum to be collected, with essentially no statistical error, in a short time ($\simeq$ 1 hour). However we note that this procedure must be used with caution, since if for any reason (eg detector saturation) the incident spectrum is not smoothly varying with t, the fit will not be accurate and spurious features may be introduced into the differenced spectra.

In figure 6.2 we show the corresponding filter-in spectrum from detector 11 together with the polynomial fit to the filter-out spectrum. The two spectra are normalised to the sum of the counts between $100 - 150$ and $500 - 600 \mu sec$. These regions were chosen for normalisation because they are unaffected by the presence of the filter, but close to the data region. This method of spectrum normalisation is preferable to using the incident beam monitor to normalise spectra, as the drift in relative detection efficiency of the monitor and other detectors with time is typically $1 - 2\%$. There is some drift with time of the relative efficiency of the regions $100 - 150$ and $500 - 600$ within a single spectrum, but this is much smaller ($\simeq 0.3\%$ see section 9.1).

The difference between the smoothed foil out spectrum and the foil in spectrum is shown in figure 6.3 for detectors in one of the two 45° banks on EVS. There are two clearly separated peaks. The first, at shorter times is due to hydrogen scattering and moves to lower t as the scattering angle increases. The second 'elastic' peak at comes from zirconium and aluminium can scattering and has a position which is almost independent of angle. The higher angles give a clear separation of the two peaks. This separation, which is only obtained at very high q, is one of the advantages of the EVS instrument for hydrogeneous samples. Scattering from all sources other than hydrogen, eg cryostat tail or sample can scattering, occurs in a different region of the time of flight spectrum to the scattering from hydrogen.

6.2 Transformation to y Space

The next step in the data analysis is to transform the time of flight data to y space using equation 24. The results of a transformation on time of flight spectra from detector 11 is shown in figure 6.4.

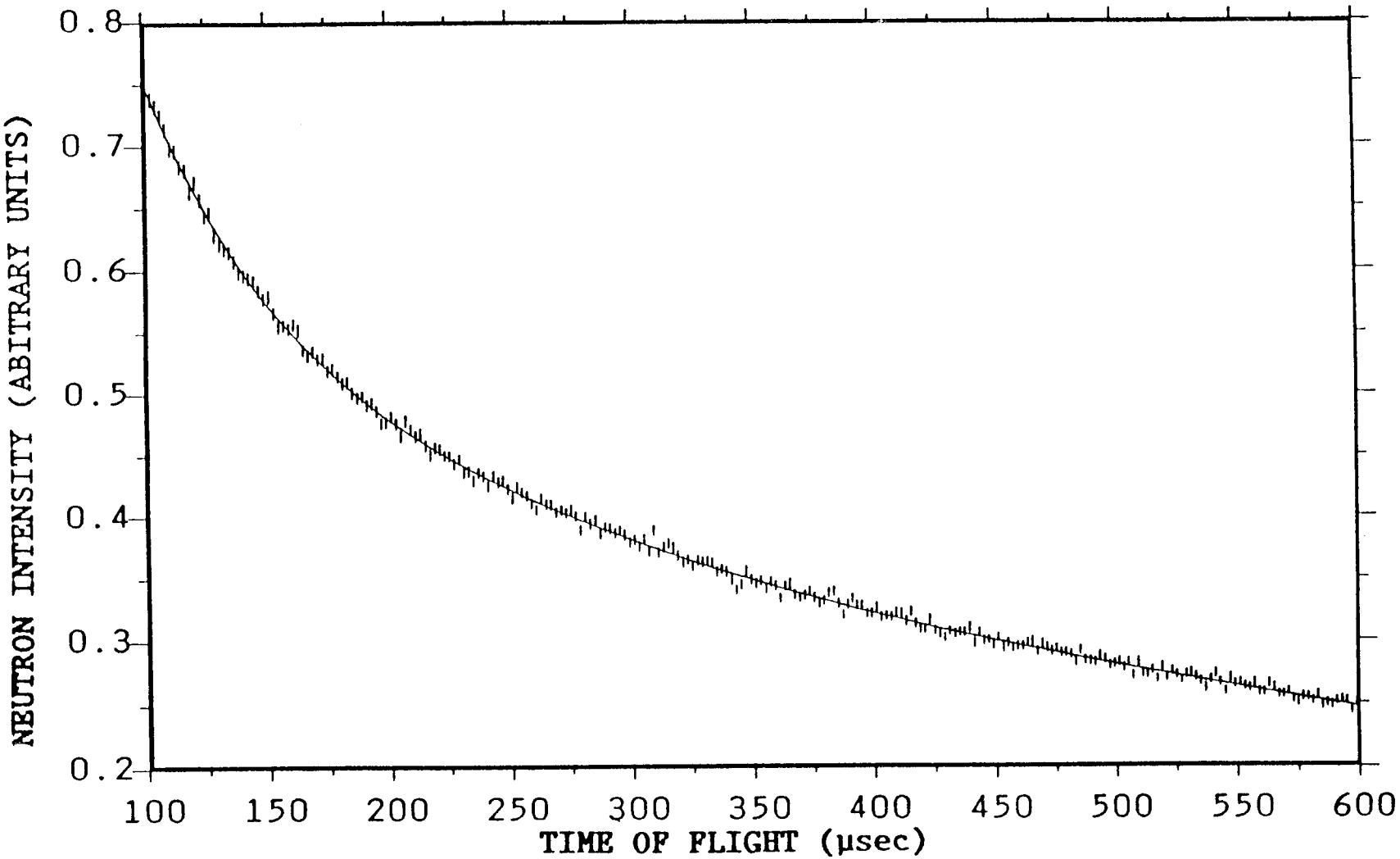

Figure 6.1 Time of flight spectrum S11 from a filter-out run on zirconium hydride. The solid line is an 8th order polynomial fit.

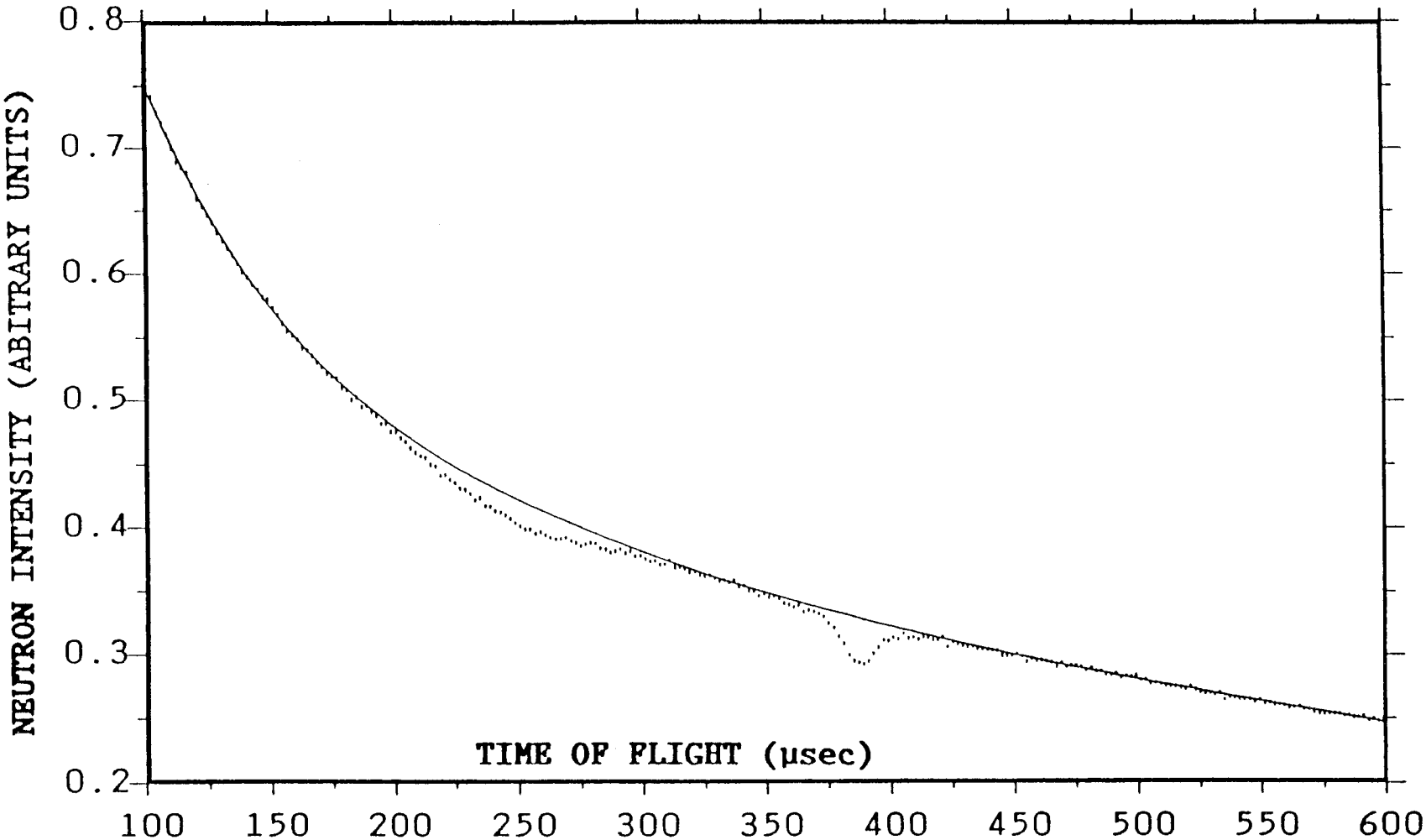

Figure 6.2 Error bars are the measured filter-in spectrum and the solid line the fitted filter-out spectrum shown in figure 6.1.

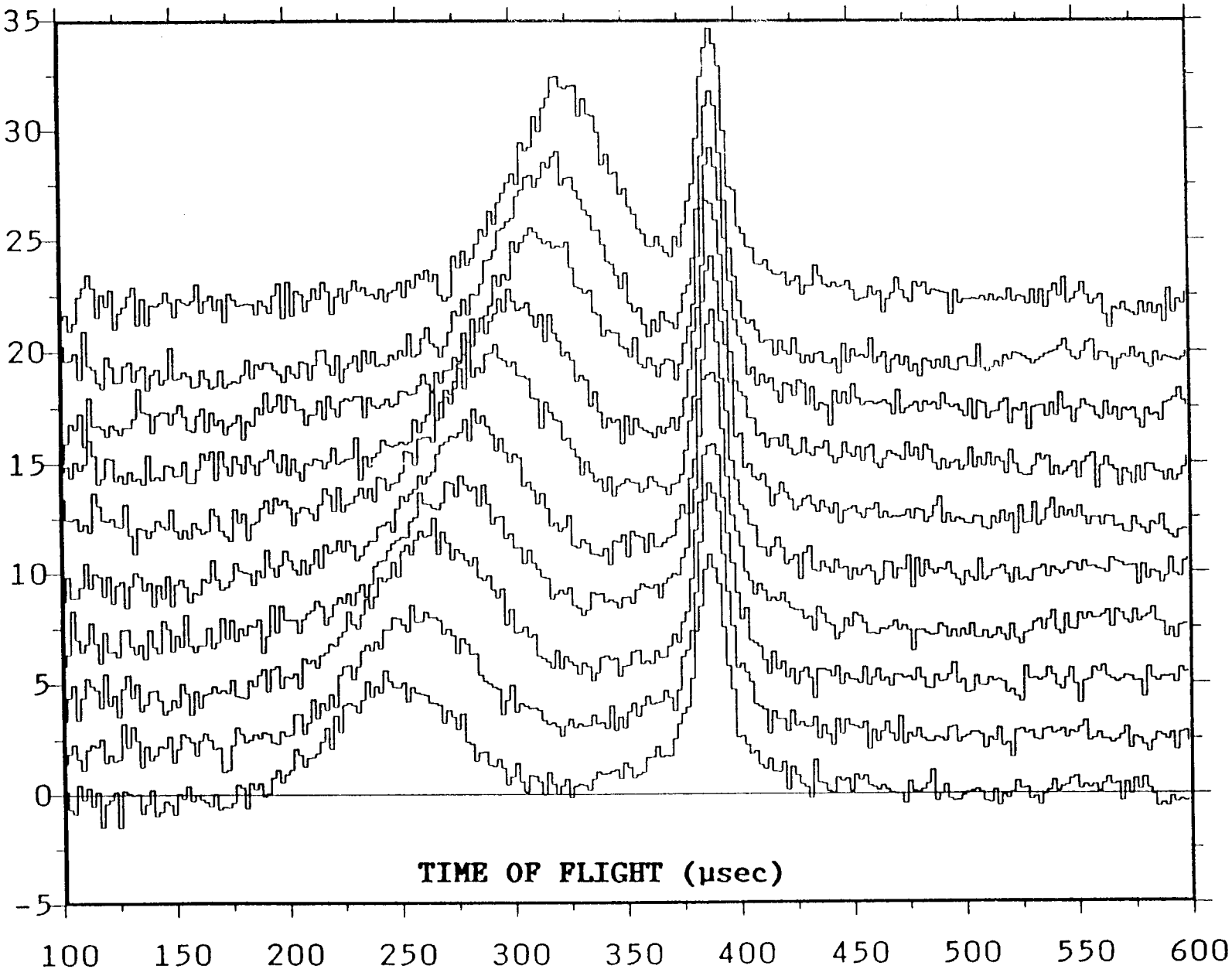

Figure 6.3 Differenced time of flight spectra from detectors 21 to 30. The sample was zirconium hydride. The scattering angle decreases from 55° for the bottom spectrum to 35° at the top.

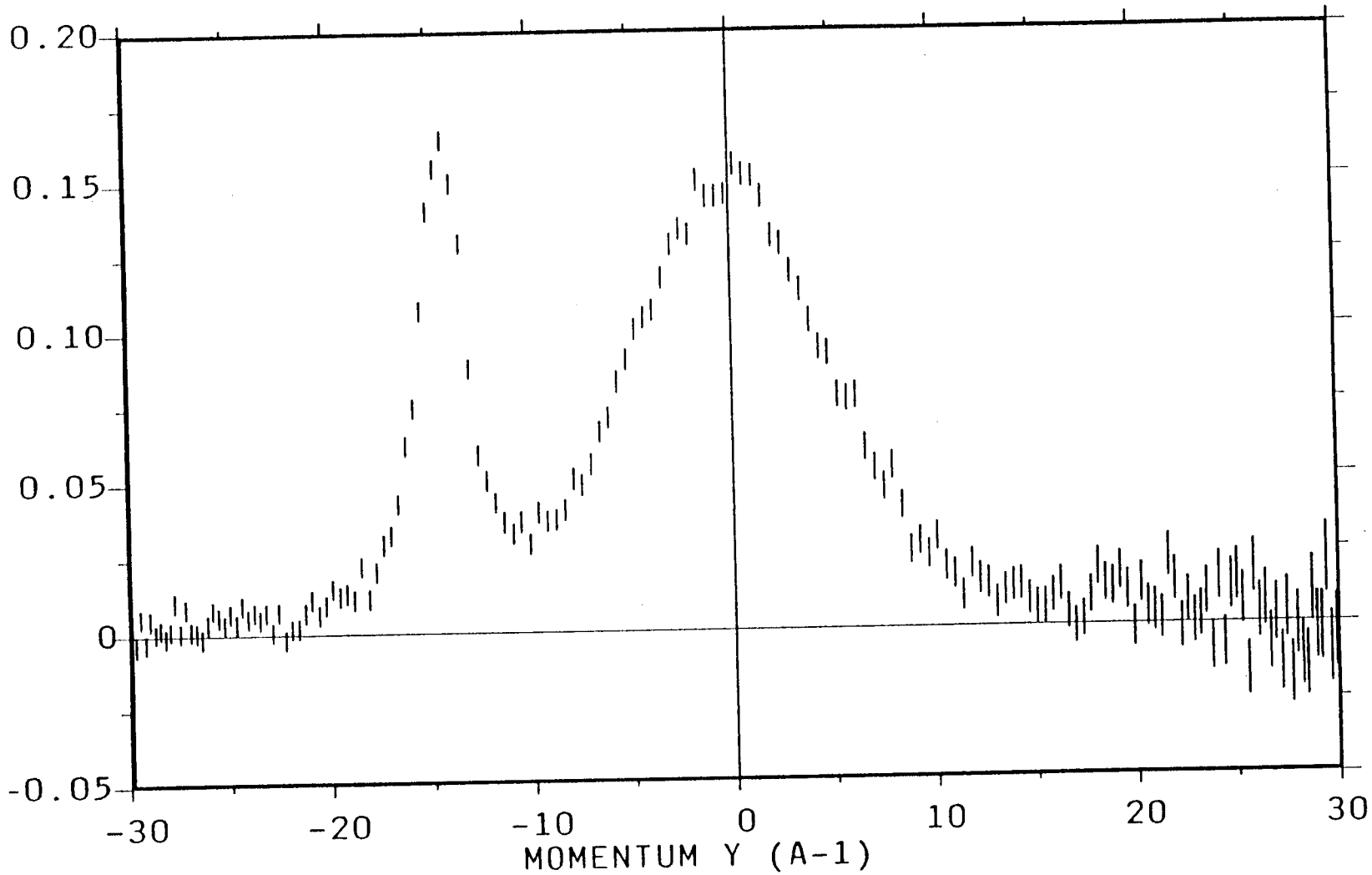

Figure 6.4 Spectrum 20 after transformation to y.

6.3 Subtraction of Elastic Scattering

The shape of the nearly elastic peak in y space is determined by the instrument resolution function for large masses, ie Lorentzian. The elastic component can be removed by fitting the sum of a Lorentzian and a Gaussian to spectra of the form shown in figure 6.4 and then subtracting the Lorentzian component from the data. Spectra from detectors 11 and 20 are superimposed in figure 6.5 after subtraction of the Lorentzian. Detector 11 at $\theta = 55°$ and detector 20 at $\theta = 35°$ correspond to the maximum and and minimum scattering angles in the forward angle banks. We note that the very good agreement between the two spectra after transformation to y, indicates that the impulse approximation is well satisfied for scattering from hydrogen for all detectors in the forward angle bank on EVS.

If the elastic peak is not well separated from the response from the sample atoms (see eg section 7.1), an aluminium can subtraction may be preferable to the Lorentzian subtraction. Automatic routines are available to perform a can subtraction including a correction for sample attenuation.

6.4 Symmetrisation

There are good arguments for symmetrising the data around $y = 0$ to reduce inaccuracies in the measured $J(y)$, introduced by a breakdown of the impulse approximation. As mentioned in section 2.1 the physical interpretation of $J(y)$ as a momentum distribution implies that $J(y)$ should be symmetric about $y = 0$. Antisymmetric components in the measured $J(y)$ are introduced by a breakdown of the impulse approximation. Sears [6] has shown that for data taken at constant q, symmetrisation removes IA inaccuracies of order $1/q$, leaving only $1/q^2$ terms. However at the high q and ω available on EVS, inaccuracies in the IA are so far undetectable and symmetrisation of the data has virtually no effect. This procedure is available if required and may become necessary as the quality of data improves.

6.5 Calculation of Atomic Kinetic Energy

The calculation of the atomic kinetic energy relies upon the assumption that $J(y)$ is of Gaussian form. The individual spectra are fitted to a Voigt function with a fixed Lorentzian component, the width of which is calculated from the energy resolution of EVS as in section 5. The Gaussian standard deviation of $J(y)$ is then obtained by subtracting the Gaussian resolution components from the fitted Gaussian component of the Voigt function. ie

$$\sigma_y = \left({\sigma_f}^2 - {\sigma_\theta}^2 - {\sigma_0}^2 - {\sigma_1}^2\right)^{\frac{1}{2}} \tag{41}$$

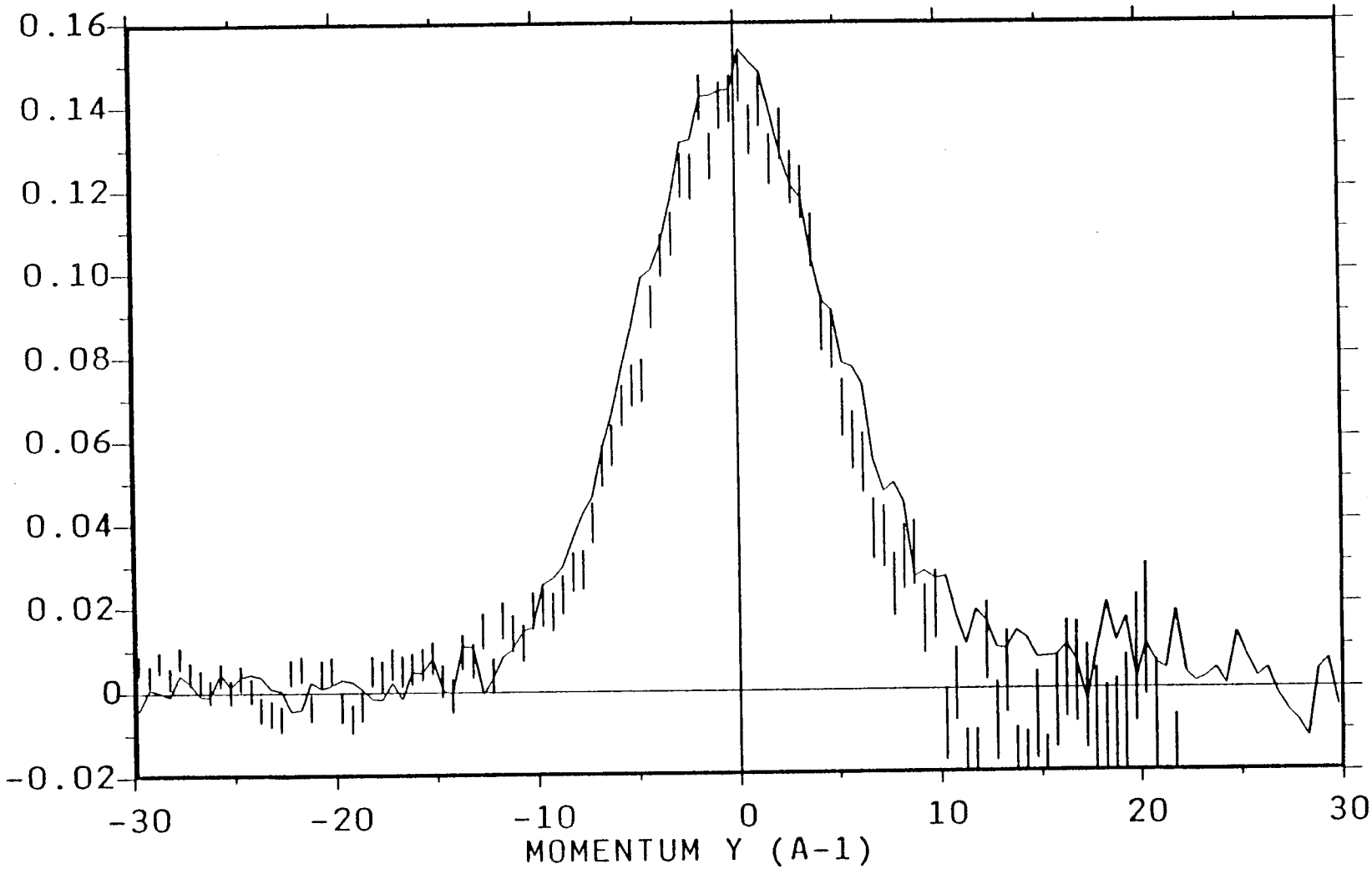

Figure 6.5 Superposition of data from detectors 11 at 55° (error bars) and 20 at 35° (line) after subtraction of the elastic Lorentzian and transformation to y. The close agreement of the spectra shows that the data y scales and suggests that the Impulse Approximation is valid.

where σ_y, σ_f ,σ_θ,σ_0 and σ_1 are respectively the standard deviations of $J(y)$,the fitted Gaussian component and the resolution components due to θ,L_0 and L_1.

The results of this procedure for a ZrH_2 sample are shown in table 6.1 which is the standard output of the automated data processing routines currently used on EVS. We note that the Gaussian resolution components make very little difference to the derived σ_y. For example σ_y for spectrum 30 is 4.302 whereas $\sigma_f = (4.302 + 0.494 + 0.119)^{\frac{1}{2}} = 4.33$. However the energy component of the resolution does make a significant difference. For example a Gaussian fit to spectrum 20 is shown in figure 6.6. The fit gave $\sigma = 4.73\mathring{A}^{-1}$ whereas after correction for the Lorentzian resolution component, we obtain $\sigma_y = 4.23\mathring{A}^{-1}$.The mean of the 20 σ values is $4.43\mathring{A}^{-1}$ with a standard error of $\pm 0.04\mathring{A}^{-1}$.

The HWHM of the Lorentian component varies between $0.6\mathring{A}^{-1}$ at $\theta = 35°$ (detectors 11 and 21) to $\simeq 1.1\mathring{A}^{-1}$ at 55° (detectors 20 and 30) for scattering from hydrogen. Thus it is not strictly correct to add spectra. However it is found empirically that if spectra 11 to 30 are added and fitted to a Voigt function with a Lorentzian HWHM of $0.8\mathring{A}^{-1}$, the fitted width of the Gaussian component is in good agreement with the mean of fits to individual spectra. This procedure is useful primarily because a display of the summed spectra gives a good indication of the quality of the data. In figure 6.7 we show the sum of spectra 11 to 30, with a fit. The fit gave $\sigma_y = 4.41 \pm 0.06\mathring{A}^{-1}$ in good agreement with the value obtained from fits to individual spectra.

6.6 The Validity of the Impulse Approximation

The fitted positions of the maxima in $J(y)$ measured on individual detectors can be used to test for inaccuracies in the Impulse Approximation. Any point in y transforms to a unique point in time of flight t and hence unique values of q and ω via equations 3, 16, 19 and 20. Thus the positions y_{max} of the peak positions in y obtained from the data analysis, give values of q_{max} and ω_{max} for each detector. As mentioned in section 2.1, if the IA is valid the peak positions satisfy $\omega_{max} = {q_{max}}^2/2M_f$ where M_f is the free atomic mass. Thus a fit to $\omega_{max} = ({q_{max}}^2 + C)/2M$ with M and C as adjustable parameters should give $M = M_f$ and $C = 0$. A fit to the values of q_{max} and ω_{max} calculated from the fitted values of y_{max} in table 6.1 is shown in figure 6.8. The fit gave $M = 0.998 \pm 0.006amu$, which is consistent with the free atomic mass $M_f = 1.0079$, and $C = -42 \pm 27meV$. The results of this test are thus consistent with the assumption that the IA is valid.

A second indication of the validity of the IA is whether the value of σ_y obtained from fits to the data changes if the data is symmetrised about $y = 0$.(See section 6.4.) For the ZrH_2 data shown in figure 6.7 we obtained $\sigma_y = 4.44 \pm 0.04$ after symmetrisation compared with 4.43 ± 0.04 before symmetrisation, ie σ_y is unchanged indicating that the IA is a good approximation.

I	LOR HWHM	SIGMA	PK POS	DYTH	DYT	CHI-SQ
11	6.213E-01	4.149E+00	-1.742E-01	4.934E-01	8.498E-02	9.973E-01
12	6.648E-01	4.328E+00	1.797E-01	4.934E-01	8.747E-02	7.566E-01
13	7.105E-01	4.315E+00	1.680E-01	4.934E-01	9.025E-02	9.273E-01
14	7.555E-01	4.402E+00	2.657E-01	4.934E-01	9.323E-02	8.849E-01
15	8.048E-01	4.631E+00	3.642E-01	4.934E-01	9.650E-02	9.719E-01
16	8.649E-01	4.403E+00	1.808E-01	4.934E-01	1.006E-01	1.003E+00
17	1.049E+00	4.392E+00	-2.702E-01	4.934E-01	1.143E-01	9.316E-01
18	9.887E-01	4.498E+00	9.881E-02	4.934E-01	1.093E-01	9.386E-01
19	9.224E-01	4.464E+00	1.051E-01	4.934E-01	1.047E-01	9.269E-01
20	1.126E+00	4.233E+00	-2.003E-01	4.935E-01	1.199E-01	9.099E-01
21	6.233E-01	4.129E+00	-7.775E-02	4.934E-01	8.481E-02	7.833E-01
22	6.662E-01	4.430E+00	2.232E-01	4.934E-01	8.740E-02	8.588E-01
23	7.119E-01	4.369E+00	1.922E-01	4.934E-01	9.013E-02	1.007E+00
24	7.582E-01	4.595E+00	4.067E-01	4.934E-01	9.315E-02	1.009E+00
25	8.077E-01	4.652E+00	3.302E-01	4.934E-01	9.638E-02	1.056E+00
26	8.603E-01	4.602E+00	2.894E-02	4.934E-01	1.002E-01	1.342E+00
27	9.177E-01	4.605E+00	-1.830E-01	4.934E-01	1.043E-01	1.103E+00
28	9.787E-01	4.650E+00	-3.453E-01	4.934E-01	1.087E-01	9.982E-01
29	1.048E+00	4.450E+00	-2.639E-01	4.934E-01	1.137E-01	1.023E+00
30	1.115E+00	4.302E+00	-5.863E-01	4.935E-01	1.194E-01	9.533E-01

Table 6.1 Output of standard data processing routines.

Column 1 detector number
Column 2 σ_E = calculated HWHM of energy component of resolution function.
Column 3 σ_y = fitted standard deviation of $J(y)$
Column 4 Peak position in y.
Column 5 σ_θ = calculated standard deviation of angular component of resolution function.
Column 6 $(\sigma_0{}^2 + \sigma_1{}^2)^{1/2}$ = calculated standard deviation of length component of resolution function.
Column 7 reduced chi-square of the Voigt fit to the processed spectrum.

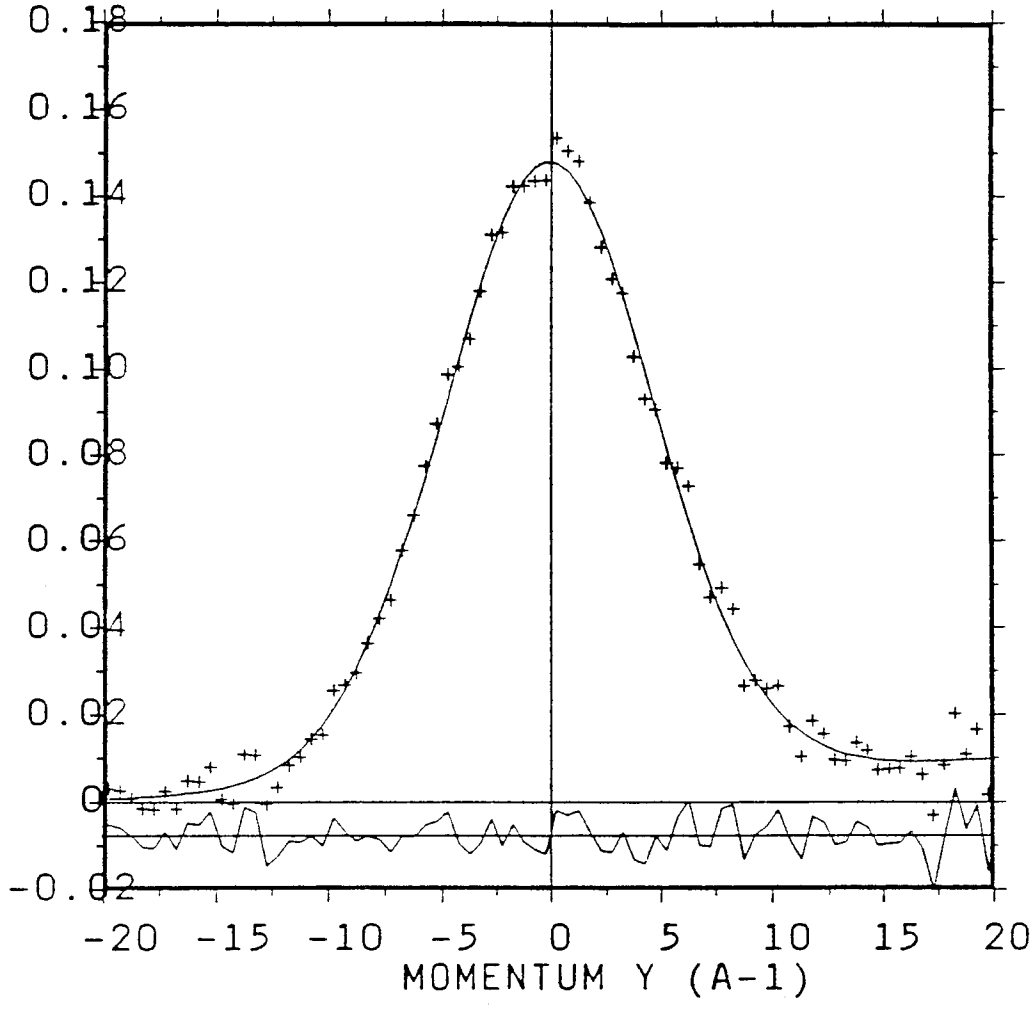

Figure 6.6 Gaussian fit to spectrum 20.

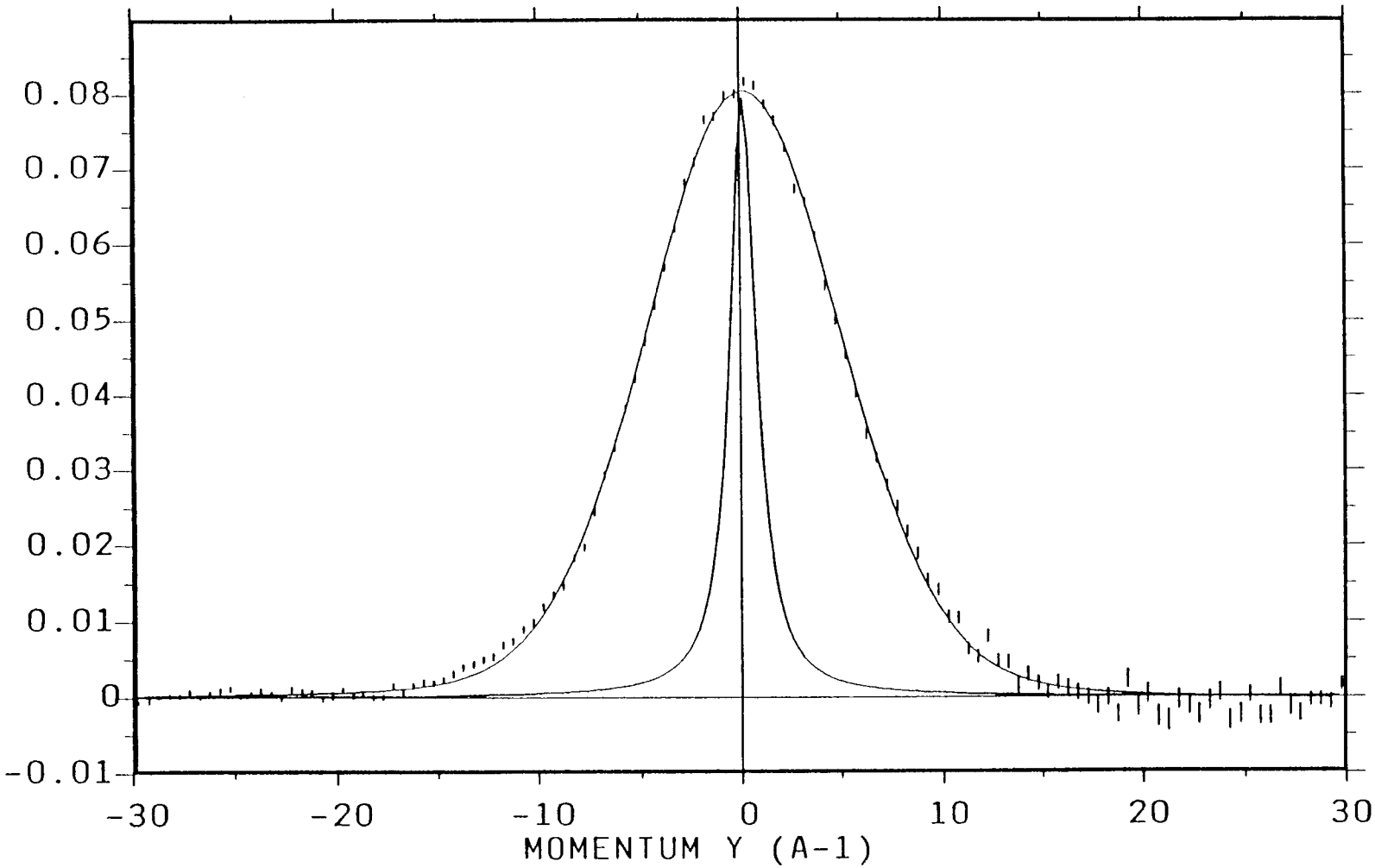

Figure 6.7 Error bars are the sum of all detectors in the $\pm 45°$ banks. The solid line is a Voigt fit. The esimated resolution function of the instrument is also shown.

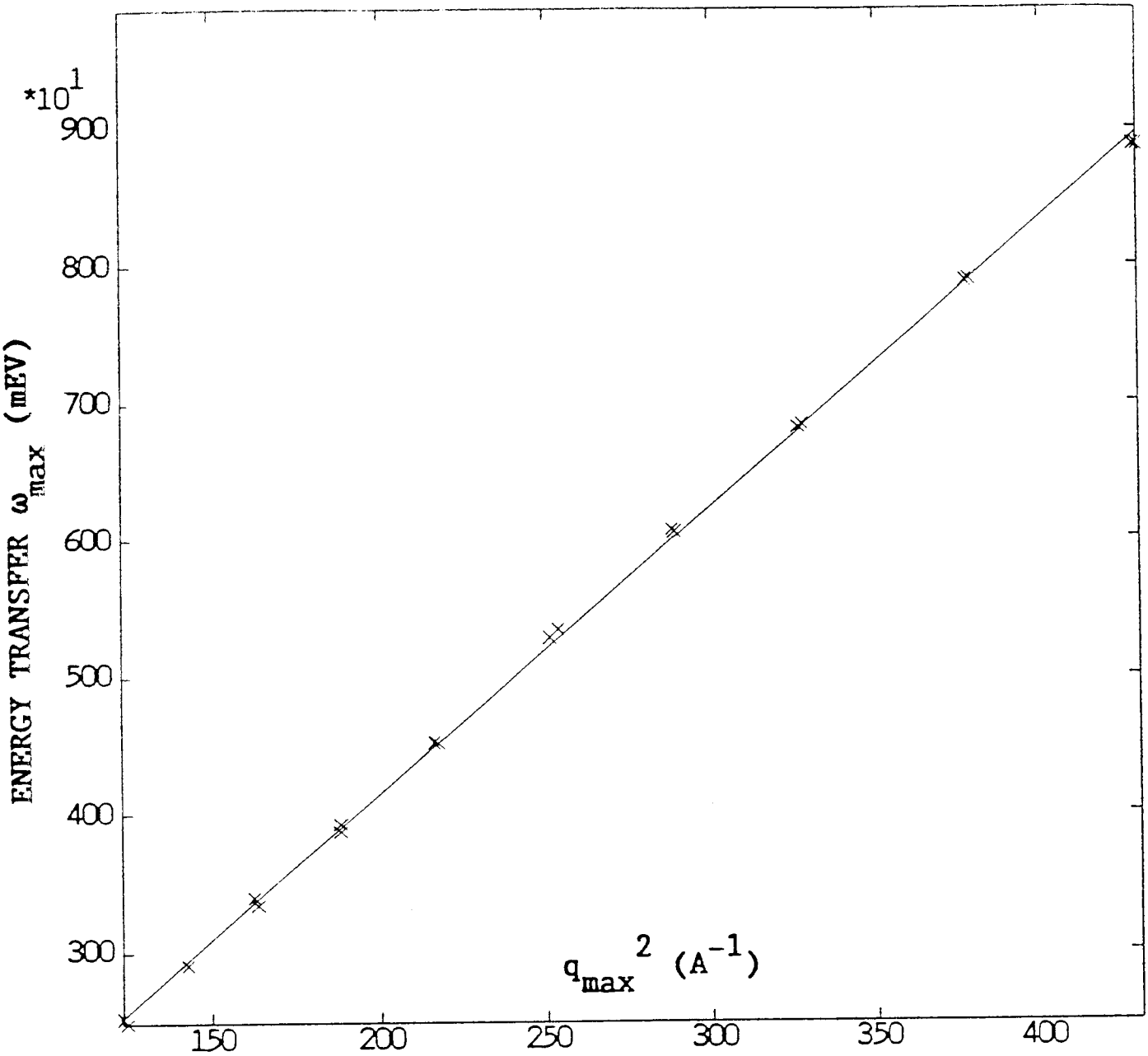

Figure 6.8 The points are the fitted positions of the hydrogen peak in q, ω. The solid line is a least squares fit to $\omega = q^2/(2M) + C$, with $M = 0.998 \pm 0.006$, $C = -42 \pm 27$.

A third test for the validity of the IA is to calculate the difference $C^* = [\omega_{max} - {q_{max}}^2/2M_f]$ for each detector. The mean value of C^* calculated from the data in table 6.1 was $C^* = 10 \pm 11meV$, ie $C^* = 0$ to within the experimental error as required by the IA.

7 Examples of Measurements

7.1 Polycrystalline Lithium

Measurements of the neutron Compton profile in lithium were made at 20K and room temperature. The differenced time of flight spectra from detectors 3 ($\theta = 131.4°$) and 15 ($\theta = 45.7°$) at 20K are shown in figures 7.1 and 7.2 respectively. The counting time required to obtain these spectra was $3600\mu Ahrs$, ie 36 hours at normal ISIS intensity, with a 1% scatterer. The peak to the right in figure 7.1 is caused by scattering from the aluminium container, that to the left by scattering from Li. In figure 7.2 the lithium and aluminium peaks are merged into a single peak. This is due to the lower momentum transfers and worse resolution available at forward angles. The separation in energy transfer (and hence time of flight) of peaks from different atomic masses decreases as θ and q decrease and the resolution is worse by a factor 2.5 at 45° compared with 135°. The combination of these two effects causes the resolution broadened peaks to merge into a single peak.

It can be seen from figure 5.6 that over the angular range of the backward angle bank ($125° < \theta < 138°$), the energy component of the y space resolution for Li is virtually constant at $\sigma_L \simeq 3.2\mathring{A}^{-1}$. Thus spectra 1 to 10 can be added and fitted to a Voigt function with the above value of σ_L for the Lorentzian component. In figures 7.3 and 7.4 we show the summed data for the 20K and 290K data after aluminium can subtraction and conversion to y space. The fit to a Voigt function and the Lorentzian component of the Voigt function are also shown. The Gaussian components of the fitted Voigt function were $4.80\mathring{A}^{-1}$ at 20K and $6.95\mathring{A}^{-1}$ at 290K . The Gaussian component of the resolution function, was $({\sigma_L}^2 + {\sigma_6}^2)^{\frac{1}{2}} \simeq 0.7\mathring{A}^{-1}$. After correction for the Gaussian resolution component we obtain $\sigma = 4.77 \pm 0.06\mathring{A}^{-1}$ at 20K and $\sigma = 6.91 \pm 0.07\mathring{A}^{-1}$ at 290K.

An alternative procedure for data analysis is to use the procedure described in section 6. In this case, Voigt fits are performed on individual spectra and the mean values and standard deviation of the means from the various detectors are calculated. This procedure is preferable for the forward angle banks, where the resolution varies significantly over the angular range. In table 7.1 we give values for the standard deviation of $J(y)$ obtained from the $\pm 45°$ and $\pm 135°$ banks at 20K and 290K.

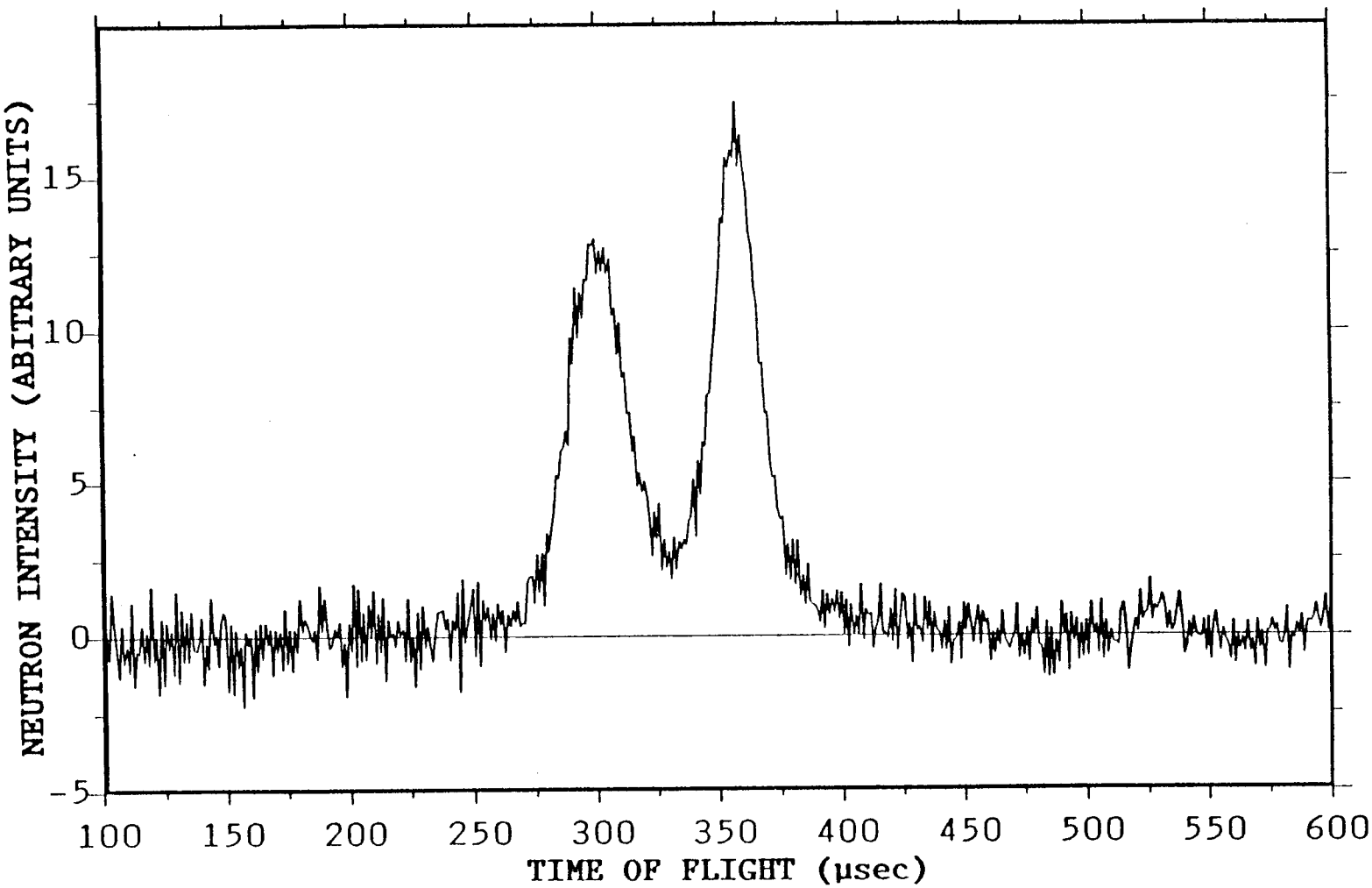

Figure 7.1 Differenced time of flight spectrum for lithium at 290K and a scattering angle of 135°. The left hand peak is the lithium response, the right hand peak is scattering from the aluminium sample can.

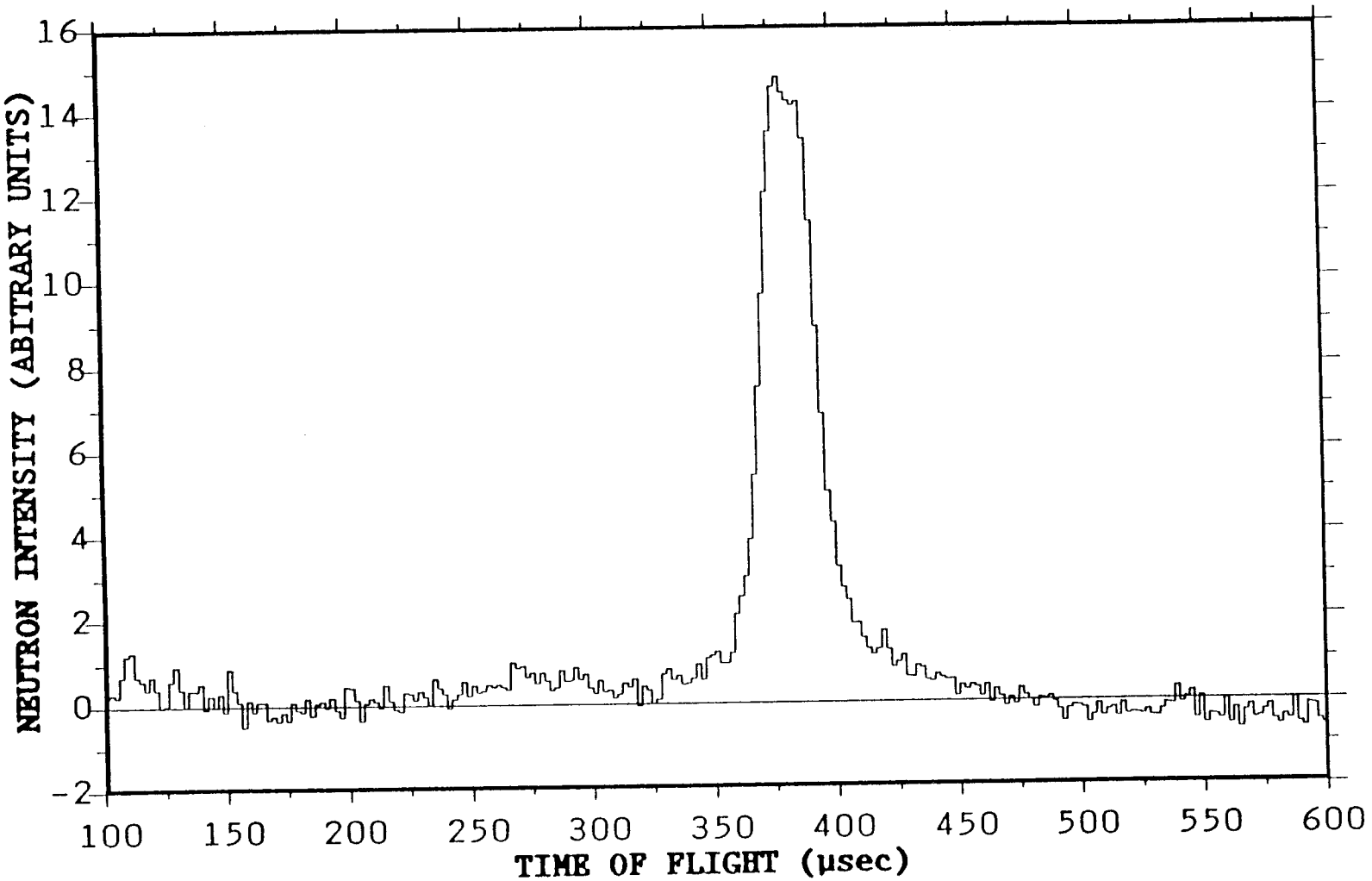

Figure 7.2 Differenced time of flight spectrum for lithium at 290K and a scattering angle of 45°. The lithium and aluminium scattering are merged into a single peak.

Table 7.1 Standard deviation of J(y). σ_1 was obtained using the data analysis procedure of section 6, σ_2 was obtained from the fits shown in diagrams 7.3 and 7.4. σ_D is the prediction of the Debye model (see section 2.3)

T	Bank	$\sigma_1(\mathring{A}^{-1})$	$\sigma_2(\mathring{A}^{-1})$	$\sigma_D(\mathring{A}^{-1})$
20	135°	4.76±0.06	4.77±0.06	4.63
20	45°	5.29±0.06		
290	135°	6.90±0.08	6.87±0.07	6.74
290	45°	6.75±0.06		

Previous measurements have suggested that the mean kinetic energy of lithium is between 10% and 30% higher than the prediction of the Debye model [12], whereas the EVS data suggests that the KE is $\simeq 5\%$ higher than the Debye model prediction. The agreement between the measurements at 45° and 135° is very satifactory considering that (from figure 5.5) $6 < \sigma_L < 9\mathring{A}^{-1}$ for the forward angle bank and thus the measured $J(y)$ is resolution dominated at 45°. The small discrepancy between the 45° and 135° results at 20K is probably caused by an imperfect can subtraction in the latter case.

7.2 Measurements on Zirconium Hydride

Three experiments on the same sample of zirconium hydride were performed over a three month running period, with a separation of approximately a month between measurements. A typical data set collected over a 20 hour running period with a 5% scatterer is shown in figure 6.7 and the results of the data analysis procedures described in section 6 are given in table 7.2.

Table 7.2 Parameters obtained from different runs for zirconium hydride

RUN	$\sigma(\mathring{A}^{-1})$	$M(amu)$	$C(meV)$	$C^*(meV)$
857	4.43±0.04	0.998±0.005	−42±27	10±11
897	4.47±0.06	1.002±0.009	−28±46	5±17
948	4.41±0.06	1.004±0.008	−17±40	39±15

We note that no differences from the predictions of the IA ($M = 1.0079, C = C^* = 0$) are detectable within the accuracy of the measurements. From equation 15, assuming that the proton sits in a harmonic potential, $\sigma = 4.44\mathring{A}^{-1}$ corresponds to a harmonic oscillator with frequency $\omega_0 = 164meV$ compared with the values between 140 and $170meV$ obtained from measurements of transition energies by neutron spectrosopy [13].

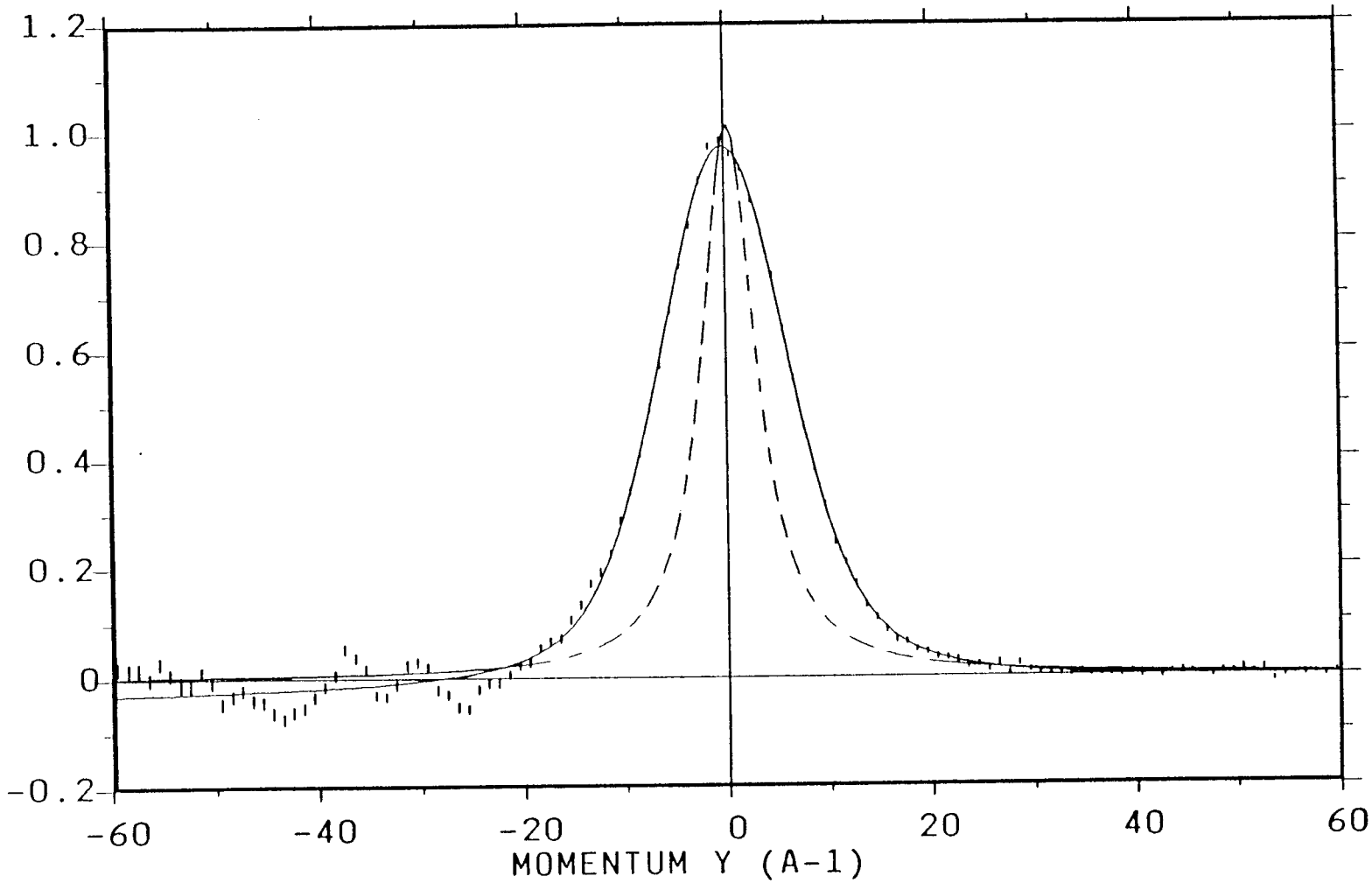

Figure 7.3 Error bars are the measured $J(y)$ for lithium at 20K. The solid line is the fit. The dashed line is the calculated instrument resolution function. The oscillations to the left of the peak are caused by an imperfect can subtraction.

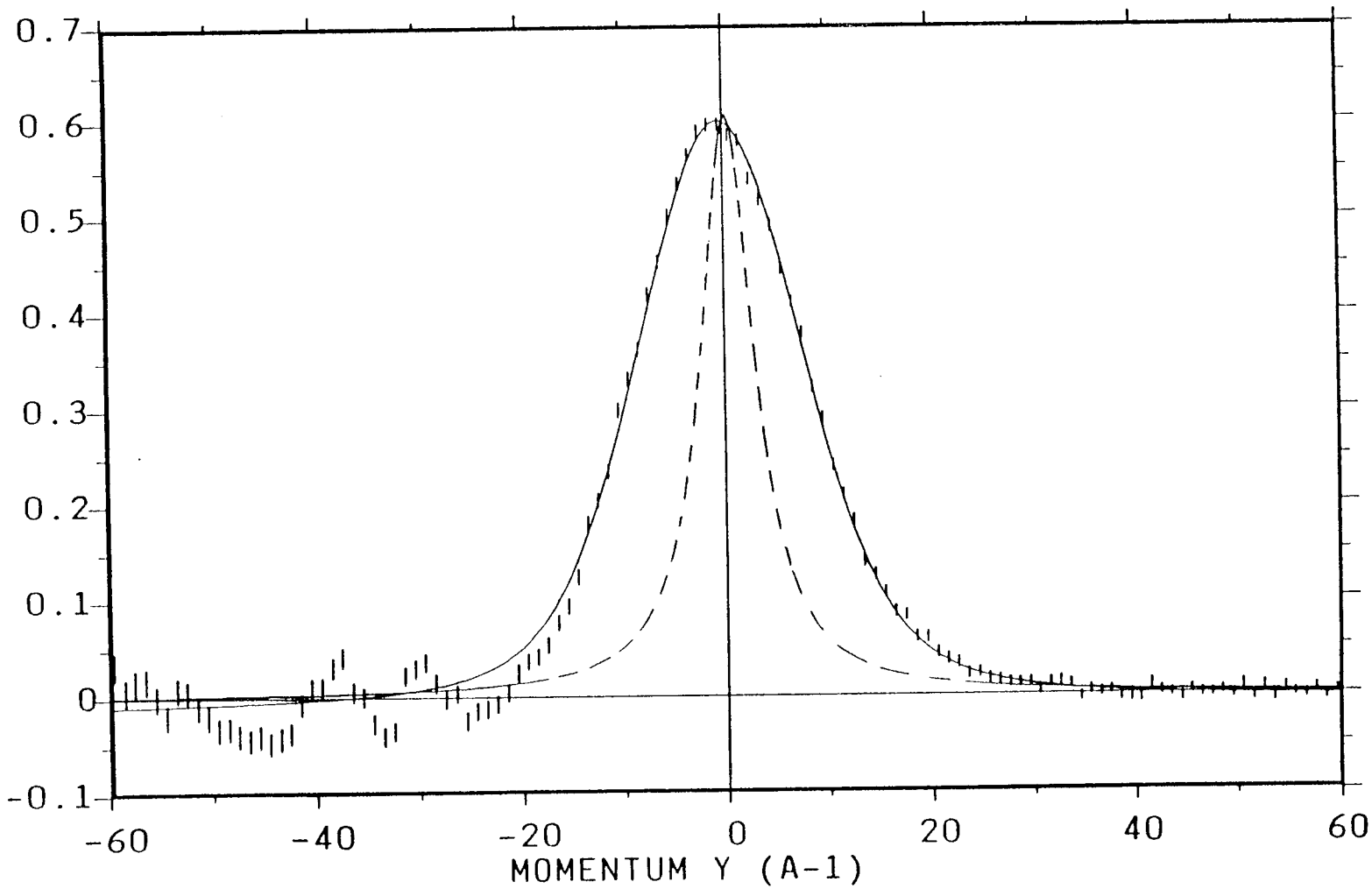

Figure 7.4 Error bars are the measured $J(y)$ for lithium at 290K. The solid line is the fit. The dashed line is the calculated instrument resolution function. The oscillations to the left of the peak are caused by an imperfect can subtraction.

7.3 Measurements on Light and Heavy Water

Measurements were performed on H_2O and D_2O at 290K and 20K. Typical fits to the sums of spectra 11–30 are shown in figure 7.5 for H_2O at 20K and figure 7.6 for D_2O at 20K. We note that the measured $J(y)$ is non-zero to the right of the peak for both H_2O and D_2O data. For H_2O this is probably caused by the detector instability discussed in section 9.1. For D_2O the most likely explanation is that there was some contamination of the sample with H_2O and the non-zero baseline to the right is caused by scattering from hydrogen. Non-zero baselines are potentially a serious problem they influence the fitted width of the distribution. Typically a negative baseline reduces the fitted width, while a positive baseline increases the fitted width. Visual inspection of figures 7.5 and 7.6 suggests that the H_2O width is accurate, but the D_2O widths are probably slightly too large. The parameters obtained from the data analysis procedures are listed in table 7.4.

Table 7.4 Results of measurements on H_2O and D_2O

Sample	Temperature	$\sigma(\AA^{-1})$	$M(amu)$	$C(meV)$	$C^*(meV)$
H_2O	20	5.09±0.04	1.003±0.006	−2±30	21±10
H_2O	290	5.39±0.07	1.007±0.010	−16±37	−14±14
D_2O	20	5.93±0.17	2.008±0.020	8±18	14±5
D_2O	290	6.13±0.10	2.030±0.020	−3±18	16±5

We note that the results are in agreement with simple mass scaling. If we assume that H or D sit in the same harmonic potential, then σ should be proportional to $M^{\frac{1}{4}}$ and the ratio of the σ values for D/H should be $2^{1/4} = 1.189$. The ratios obtained from table 7.4 are 1.17 ± 0.03 at 20K and 1.14 ± 0.03 at 290K.

7.4 Single Crystal Measurements on Potassium Bicarbonate

As a final example of EVS data we show some measurements of $J(y)$ in a single crystal sample of $KHCO_3$, which is a hydrogen bonded system. The aim of the measurement was to observe anisoptropy in the momentum distribution of the proton in the hydrogen bond. $KHCO_3$ is a particularly favourable system as all hydrogen bonds are aligned along a single crystalline direction. It is thought that the proton experiences a double-well potential along the hydrogen bond direction and a harmonic potential perpendicular to the hydrogen bond [14].

The sample was a 20x20x1mm platelet with the H bond at $\simeq 10°$ to the plane of the sample. It was oriented with the H bond pointing at the centre of the $-45°$ detector bank. With this arrangement simultaneous measurements of $J(y)$ were made with q

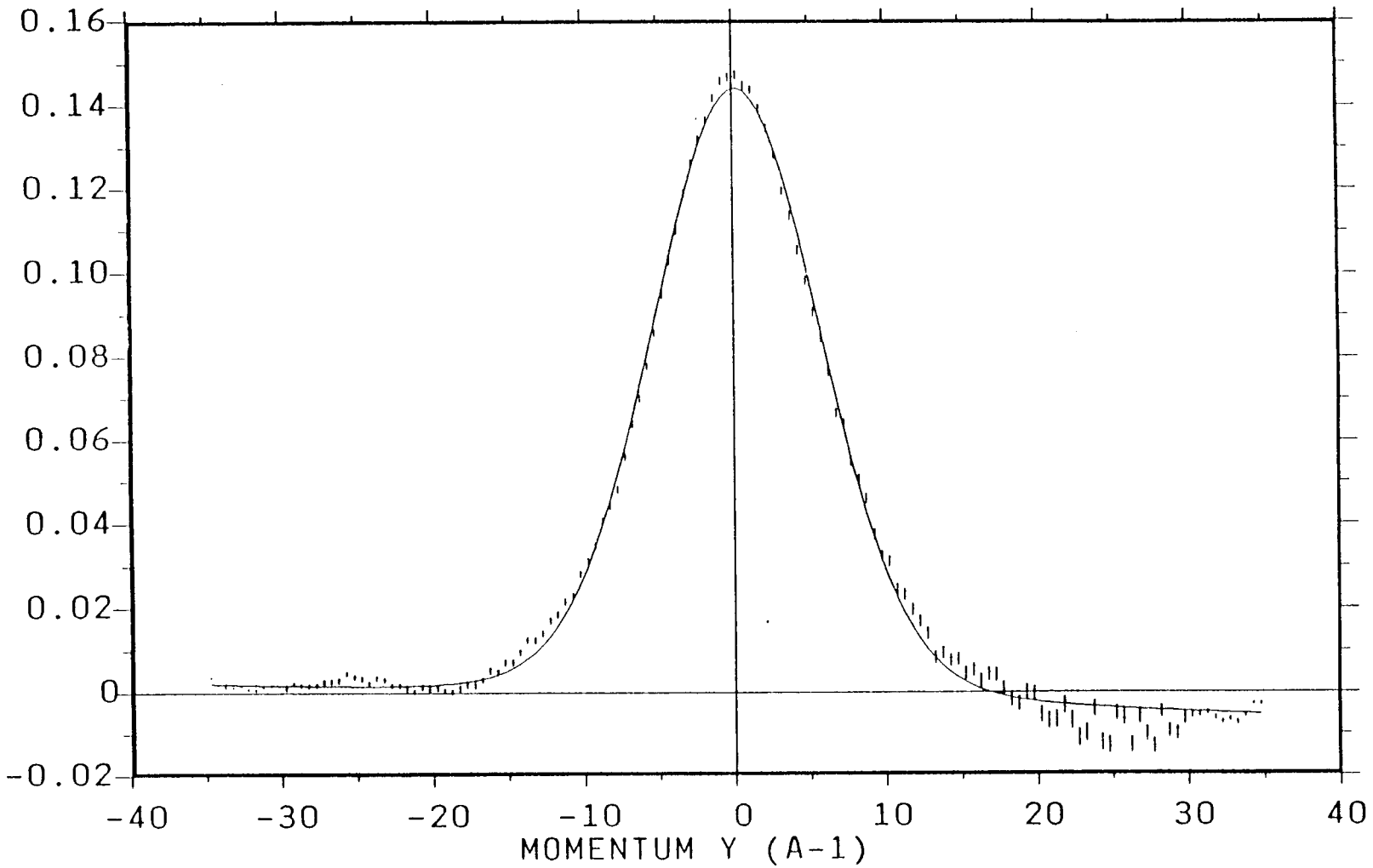

Figure 7.5 Error bars are the measured $J(y)$ for H_2O at 20K. The solid line is the fit.

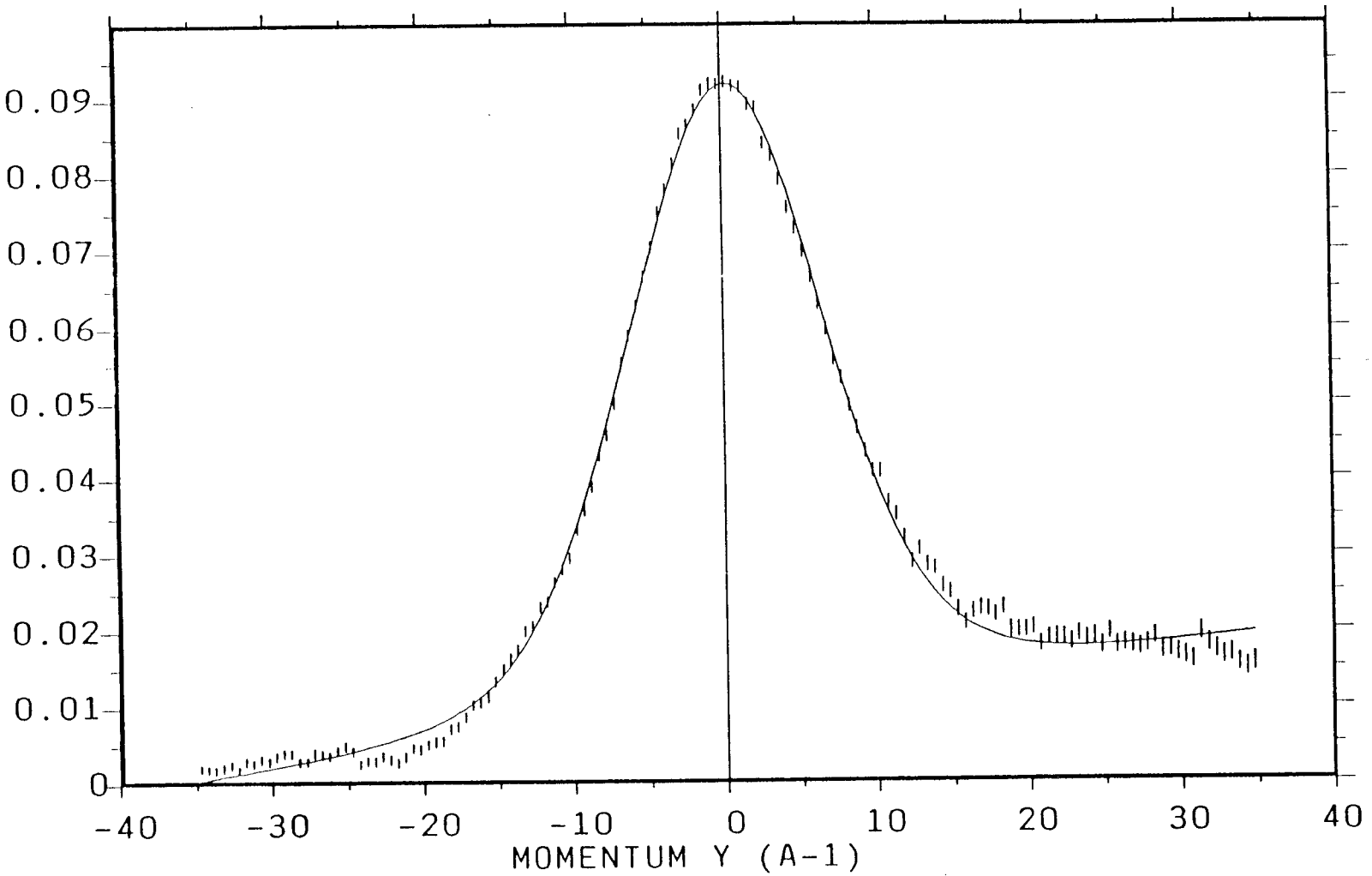

Figure 7.6 Error bars are the measured $J(y)$ for D_2O at 20K. The solid line is the fit.

roughly along the bond in the $+45°$ bank and perpendicular to the bond in the $-45°$ bank. Note that, as shown in Appendix A, in hydrogeneous systems q is perpendicular to the direction of the scattered neutron at $y = 0$. The time of flight scans on the different detector banks correspond to the scans through atomic momentum space shown in figure 7.7. The direction of q is a function of both scattering angle and time of flight and varies by $\simeq \pm 10°$ about the mean values of $\pm 45°$ in the two detector banks.

The sum of spectra from the two banks is shown in figure 7.8. The anisotropy of $J(y)$ is obvious. Fits to the data from the two banks are shown in figures 7.9 and 7.10. We obtain $\sigma = 5.3 \pm 0.09$ for q along the bond and $\sigma = 4.55 \pm 0.08$ with q perpendicular to the bond. It has been shown that the measurements are consistent with the postulated double well potential for the proton [14].

8 The Validity of the Impulse Approximation on EVS

As discussed in sections 2.1 and 6.6, the experimental data can be used to test for inaccuracies in the IA. For example if the IA is valid then the standard deviations of Gaussian fits to the measured $J(y)$ should be unaffected by symmetrisation of $J(y)$ about $y = 0$. In table 8.1 we give standard deviations before and after symmetrisation for a variety of samples.

Table 8.1 Standard deviations of Gaussian fits to the measured neutron Compton profile before (σ) and after (σ_s) symmetrisation about $y = 0$.

Sample	Temperature (K)	$\sigma(\AA^{-1})$	$\sigma_s(\AA^{-1})$
$ZrH2$	290	4.43±0.03	4.45±0.03
NbH	290	4.48±0.04	4.51±0.04
$KHCO_3$	290	5.23±0.06	5.24±0.06
H_2O	20	5.09±0.04	5.10±0.05
H_2O	290	5.39±0.07	5.41±0.09
D_2O	20	5.93±0.17	6.13±0.15
D_2O	290	6.13±0.10	6.33±0.09
Li	20	5.59±0.07	5.59±0.07
Li	290	6.75±0.06	6.75±0.06

It can be seen that for all samples except D_2O, symmetrisation makes no difference to the width of the distribution. The difference in the case of D_2O is caused by the assymmetry in $J(y)$ which can be seen in figure 7.6. As mentioned in section 7.3 this can be explained by H_2O contamination of the sample and is not caused by a breakdown of the IA.

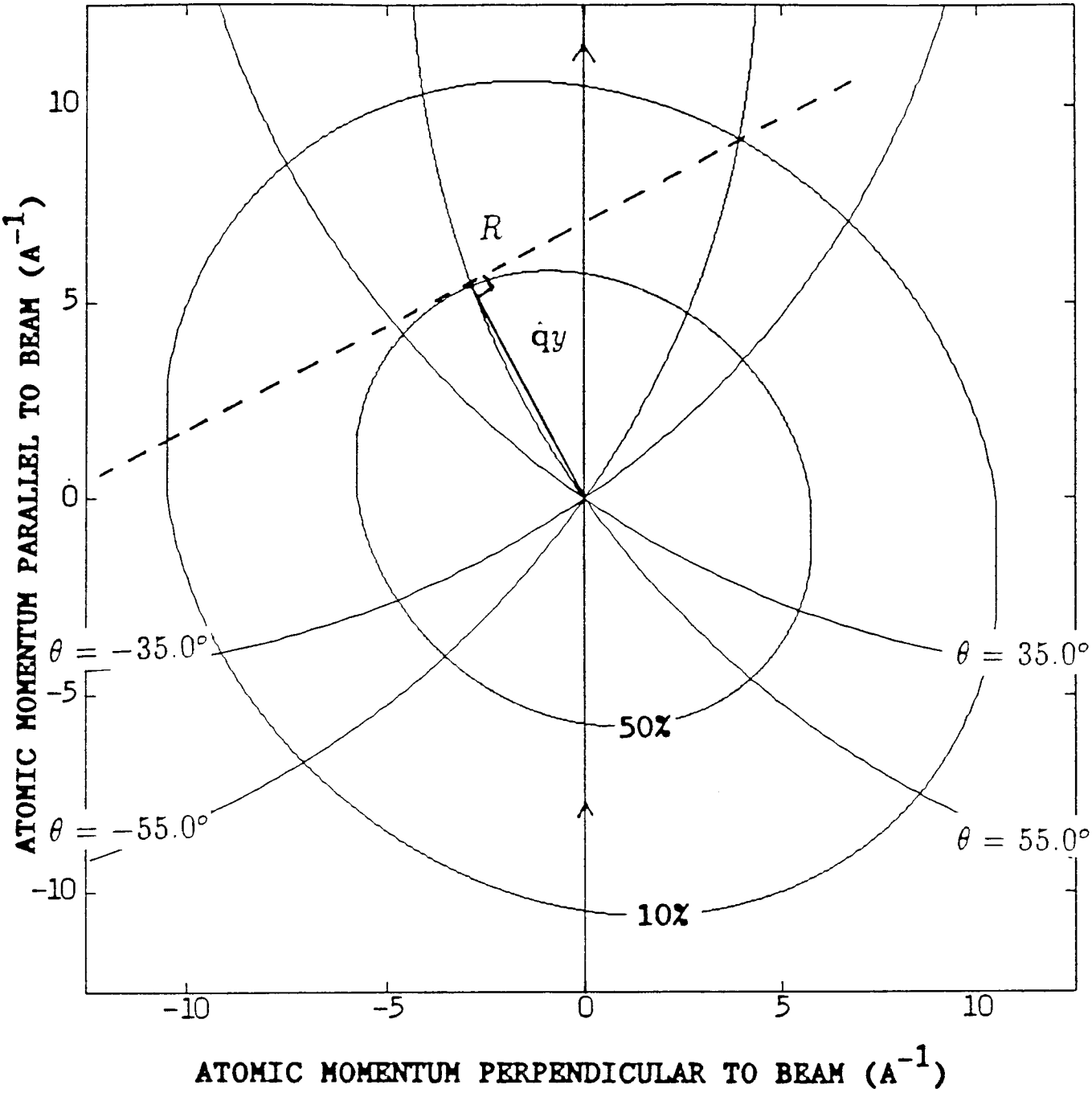

Figure 7.7 Scans in atomic momentum space on EVS for $KHCO_3$ single crystal. The ellipses have been drawn where $n(\mathbf{p})$ has fallen to 50% and 10% of its value at $\mathbf{p} = 0$. The lines indicate the path followed by the point y $\dot{\mathbf{q}}$ in $\mathbf{p}$ space (see comments after equation 5) as the time of flight varies for different scattering angles. $J(y)$ at the point R is calculated by integrating $n(\mathbf{p})$ over the plane perpendicular to $\mathbf{q}$. The projection of this plane onto the scattering plane is shown as a dotted line.

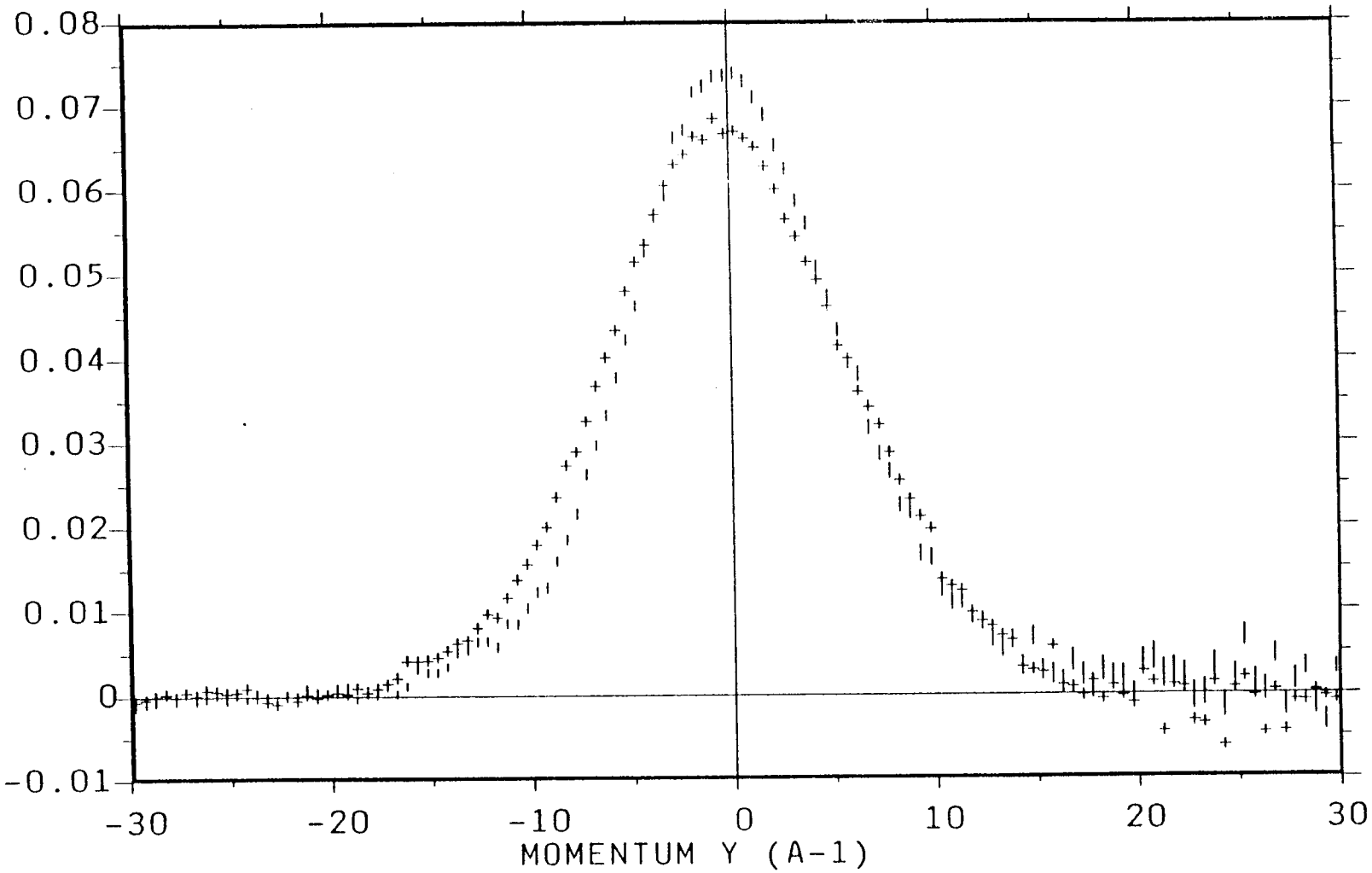

Figure 7.8 Measurement of $J(y)$ in a single crystal of $KHCO_3$. + points were measured on the $+45°$ bank with q approximately parallel to the hydrogen bond, error bars on the $-45°$ bank, with q approximately pependicular to the hydrogen bond.

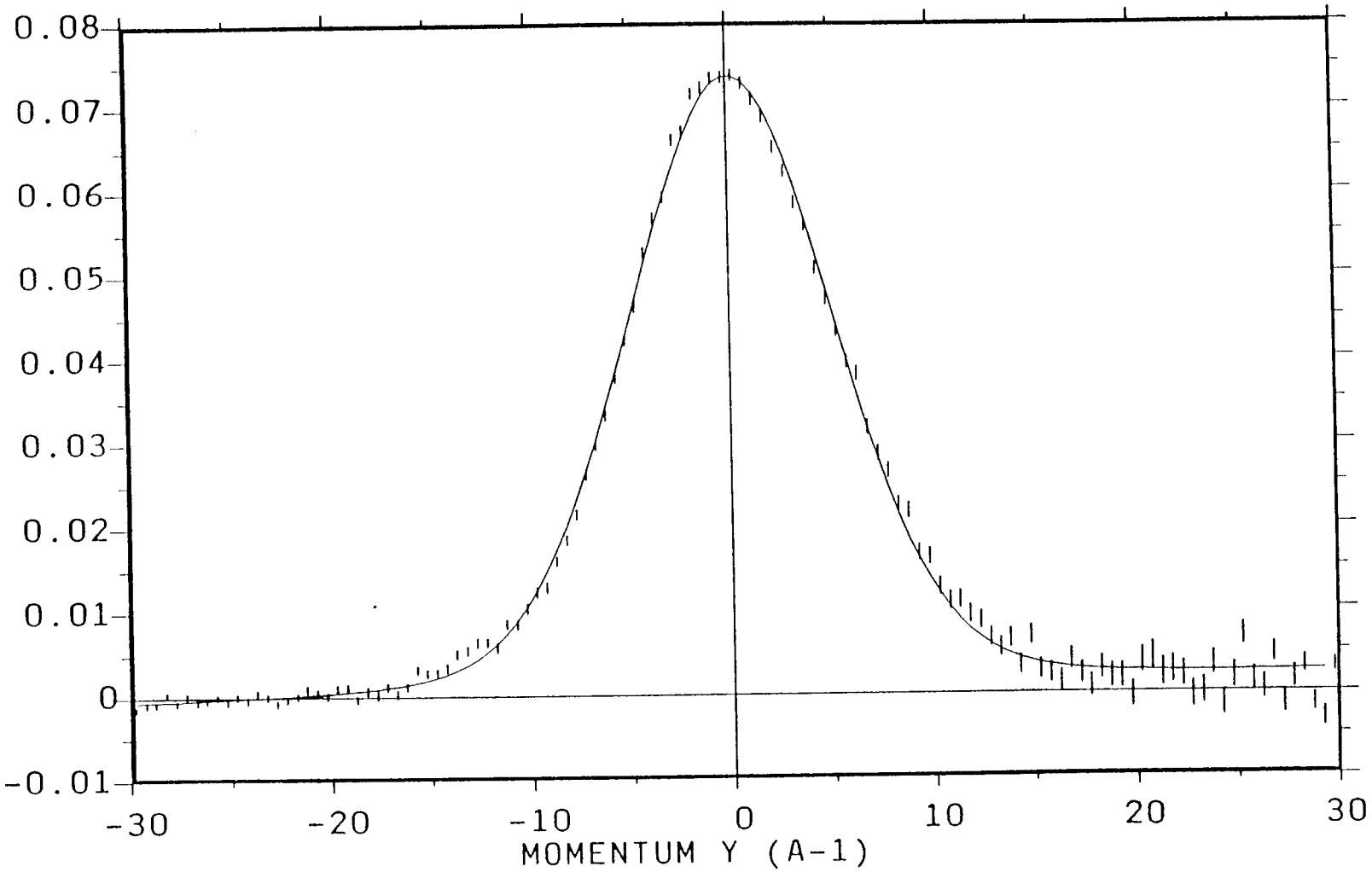

Figure 7.9a Fit to $KHCO_3$ spectrum with q parallel to bond.

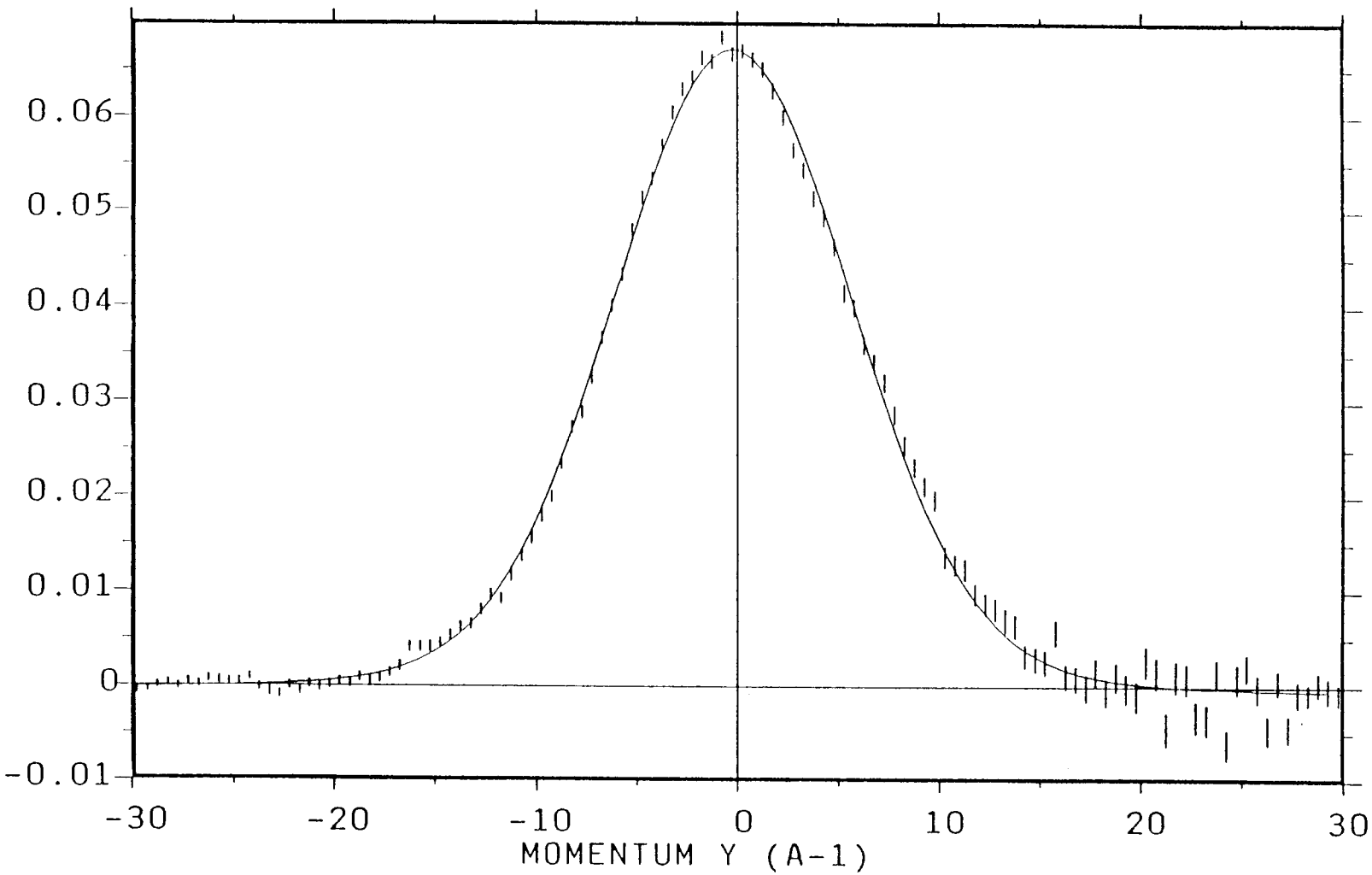

Figure 7.9b Fit to $KHCO_3$ spectrum with q pependicular to bond.

A second test of the validity of the IA is to calculate values of ω_{max} and q_{max} for each detector, as described in section 6.6, and to perform a least squares fit to $\omega_{max} = ({q_{max}}^2 + C)/2M$. If the IA is valid, we should obtain $C = 0$ and $M = M_f$ where M_f is the free atomic mass. In table 8.2 we give values of M and C calculated for the samples listed in table 8.1, using the 20 detectors in the $\pm 45°$ banks.

Table 8.2 M_f is the free atomic mass. The parameters M ,C and C^* are calculated as described in the text.

Sample	Temperature	$M_f(amu)$	$M(amu)$	$C(meV)$	$C^*(meV)$
ZrH_2	$290K$	1.0079	1.002±0.004	−28±30	10±11
NbH	$290K$	1.0079	1.007±0.003	−31±18	−25±7
$KHCO_3$	$290K$	1.0079	1.009±0.009	−60±38	−65±14
H_2O	$20K$	1.0079	1.003±0.006	−2±30	21±10
H_2O	$290K$	1.0079	1.007±0.010	−2±30	14±14
D_2O	$20K$	2.015	2.008±0.020	8±18	21±10
D_2O	$290K$	2.015	2.030±0.020	−3±18	16±5
Li	$20K$	6.941	6.44±0.17	−16±12	3±3
Li	$290K$	6.941	6.78±0.22	−8±15	3±3

It can be seen that the IA appears to be well satisfied for all samples in the table, ie $M = M_f$ and $C = 0$ to within experimental error.

A third way of analysing the data for departures from the prediction of the IA is to calculate the quantity $C^* = \omega_{max} - ({q_{max}}^2/2M_f)$ for each detector. In figure 8.1 we show values of C^* calculated for EVS detectors as a function of ω_{max} for some hydrogeneous samples. The points at a particular scattering angle lie on a single line which is defined by the instrument geometry. Their position on this line is determined by the value of y_{max} derived from $J_m(y)$. There is perhaps a suggestion from the plot that a maximum occurs at $\omega_{max} \simeq 5500meV$, corresponding to a scattering angle of $\simeq 45°$. However deviations from the IA are clearly small with $C^* \simeq 30meV$ for $\omega_{max} \simeq 5000meV$. The mean value of C^* calculated for the 20 detectors in the $\pm 45°$ banks is given in table 8.2. It can be seen that $C^* = 0$ within experimental error in most cases. The most likely explanation for the non zero values of C^* obtained for NbH and $KHCO_3$ is detector instability, rather than any breakdown of the IA.

9 Current Problems and Future Progress

9.1 Detector Instability

We believe that most serious problem facing EVS at present is caused by instability in the efficiencies of the ^3He gas detectors. Referring to figure 6.2 we see that the

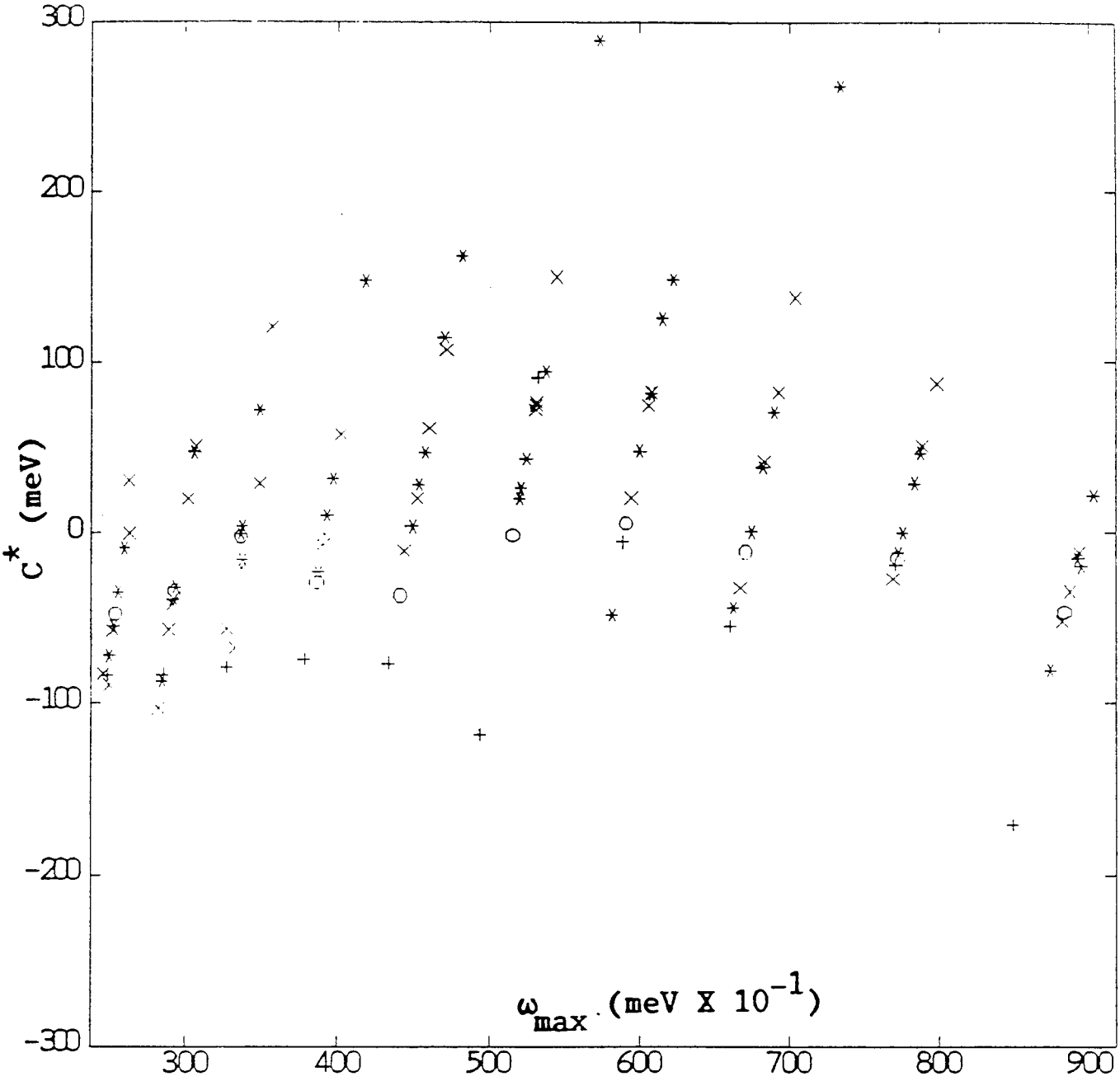

Figure 8.1 The parameter C^* as a function of ω for various runs on hydrogeneous samples. x ZrH_2, * H_2O, o NbH.

difference between the filter in and filter out spectra in the region of the hydrogen peak is $\simeq 5\%$. Thus a variation in detector efficiency of $\simeq 0.2\%$ between the filter in and filter out runs gives $\simeq 4\%$ error in the differenced spectra, introducing non-zero baselines and spurious changes in peak shape. The instability is worse when the detectors are close to saturation, presumably because the detector efficiency is then dependent on the incident beam intensity. However instabilities are still present when the detectors are not close to saturation.

As mentioned in section 6.1 the spectra are normalised to the sum of counts between $100 - 150$ and $500 - 600\mu sec$. Any change by a constant factor in the detector efficiency is removed by the normalisation procedure and is therefore unimportant.However a change in the shape of the efficiency curve or of the incident spectrum as a function of time of flight is not removed by this normalisation procedure. In figure 9.1 we show the ratio R (integrated counts between 100 and $150\mu sec$) / (integrated counts between 500 and 600), for a series of spectra in the 45° banks as a function of run number. A typical run length was 10 hours. Runs 902 to 906 were performed with the filter in and 907 to 909 with the filter out. Apart from this the runs were performed under identical conditions and any deviation of the ratio from a constant value is caused either by instability in the detector efficiency or the shape of the incident spectrum. Typical values for the deviations of the ratio from the mean are $\simeq 0.3\%$ which translates to an error of between 5 and 10% in the differenced spectra. It appears from figure 8.1 that the changes in R are correlated to some extent in different detectors, as one would expect if these changes are caused either by variations in temperature or incident beam intensity. For example all spectra display a lower value of R for run 905.

In figure 9.2 we show a spectrum from run 905 with the filter in and run 907 with the filter out. The instability causes the filter out spectrum to lie below the filter in spectrum at $t < 200\mu sec$ and above at $t > 200\mu sec$. The difference between these two spectra is shown in figure 9.3. The subtraction does not give a zero baseline and the fitted width of the hydrogen beak is likely to be incorrect due to the distortion of the peak shape introduced by the drift in detector efficiency.

It should be possible to eliminate instability problems by frequent cycling of the foil in – foil out runs. An automatic device for moving the foil in and out under computer control is at present under construction and should be operational during 1991.

9.2 Detector Saturation

The instantaneous neutron intensity at short times of flight is very high and the gas detectors are easily saturated. In figure 9.4 we show spectra from the 45° and 135° banks obtained from a beryllium sample which scattered 22% of the incident

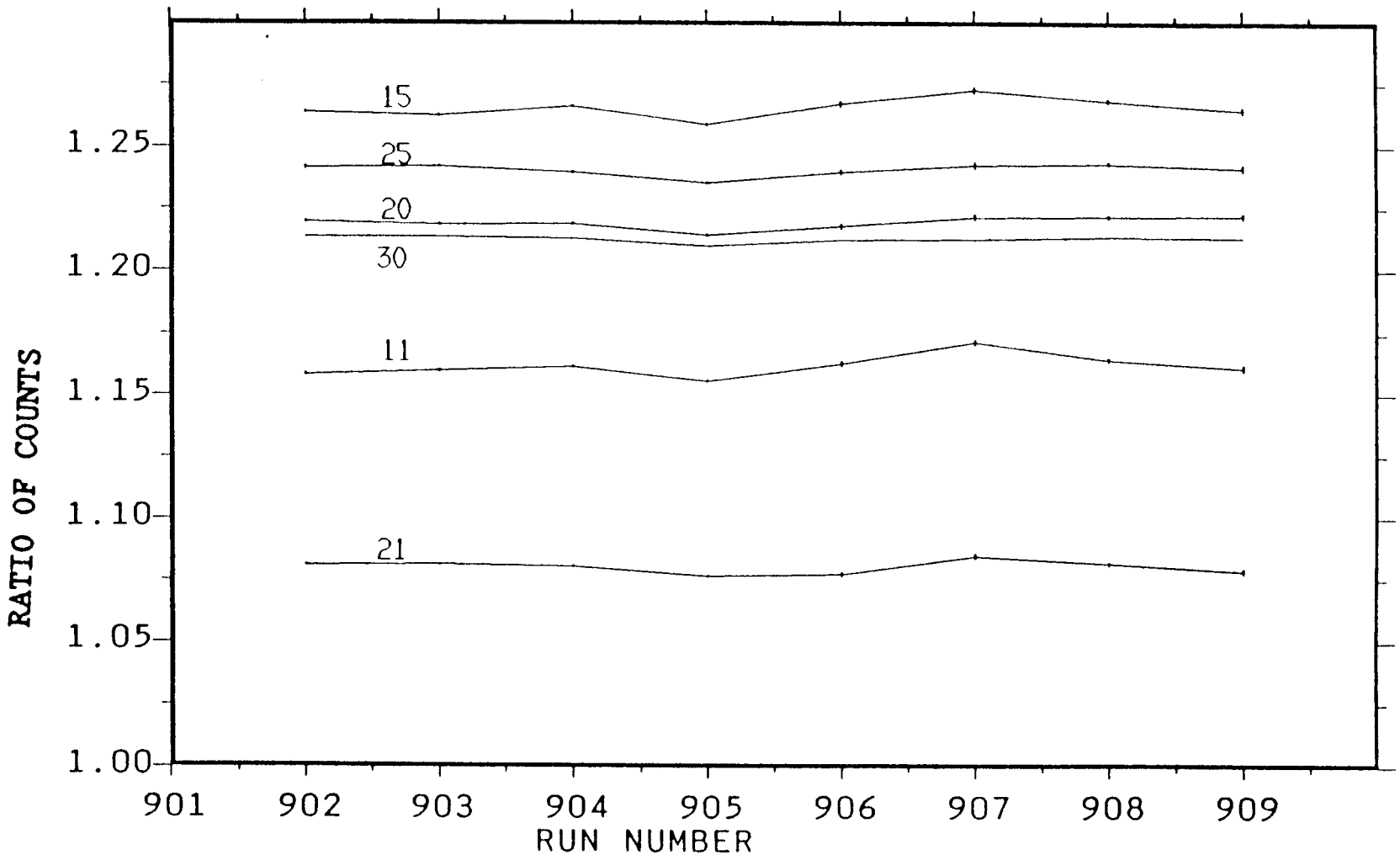

Figure 9.1 Stability test for detectors in the $\pm 45^{\circ}$ banks. The points shown as a function of run number are the ratio; (summed counts between 100 and 150 μsec) / (summed counts between 500 and 600 μsec). Runs 902 to 906 were filter-in, 907 to 909 filter-out.

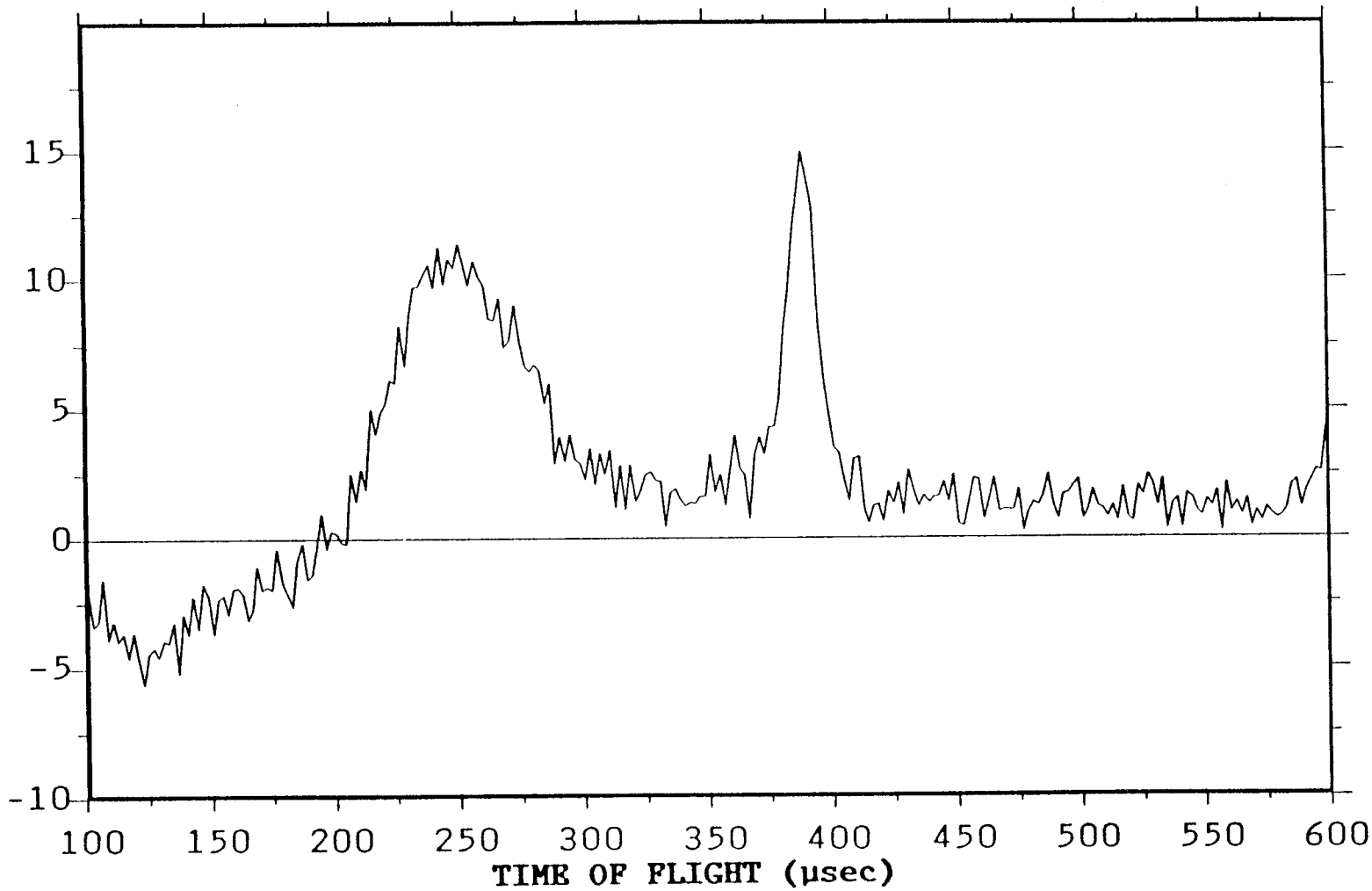

Figure 9.3 Illustration of the effects of detector instability. The difference between the spectra shown in figure 9.2.

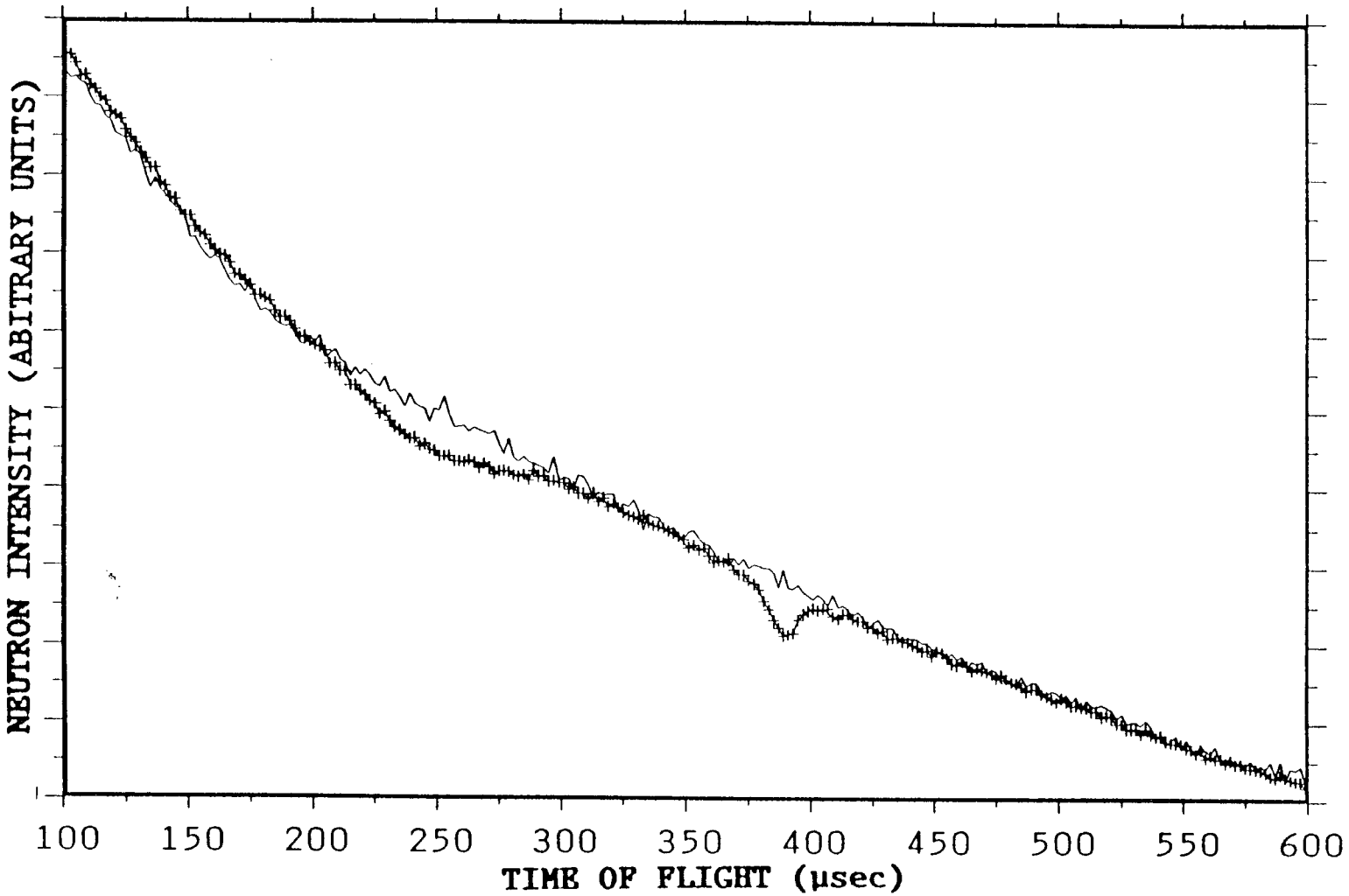

Figure 9.2 The points + are a filter in spectrum from run 905 and the line is the corresponding filter out spectrum from run 907.

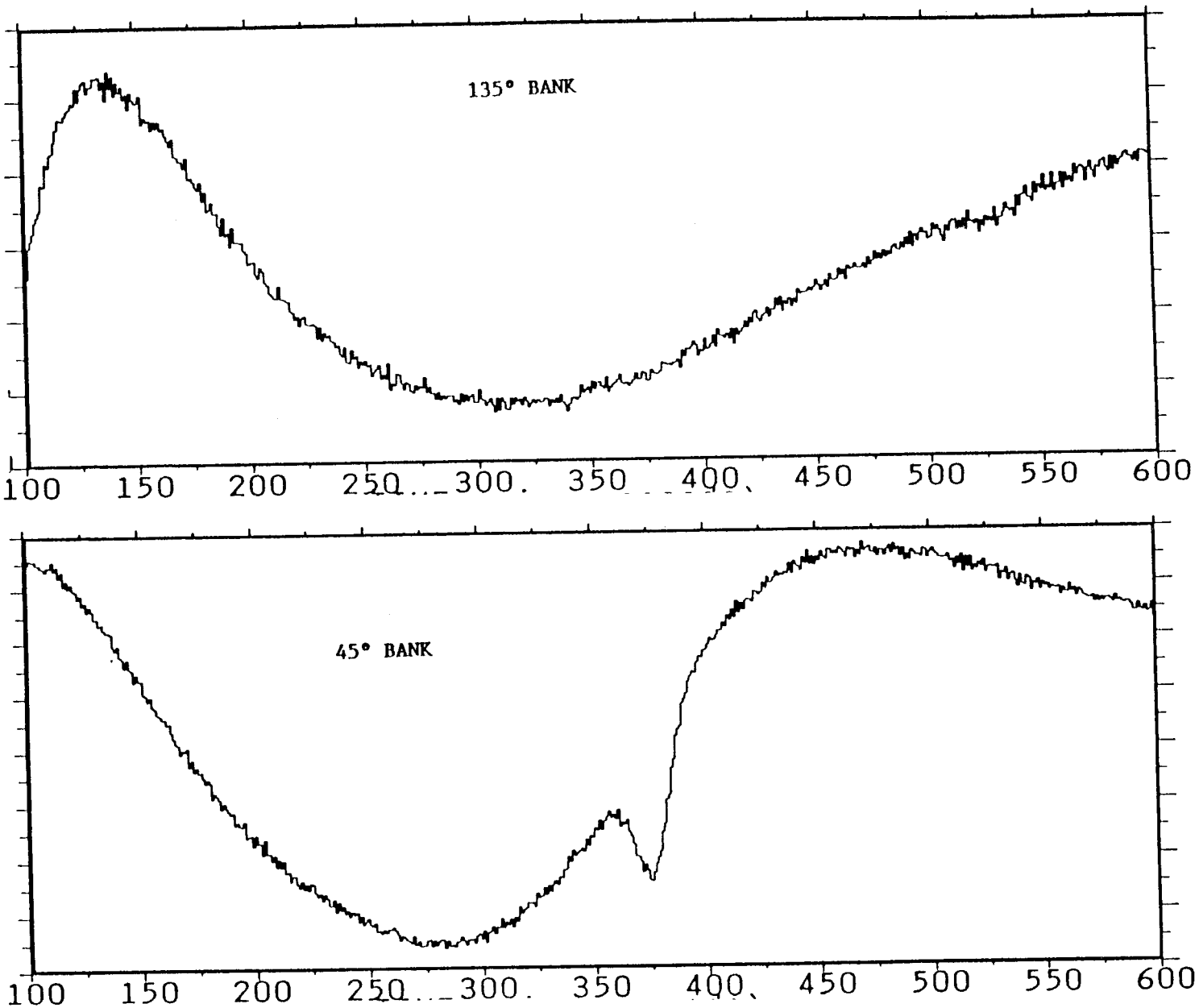

Figure 9.4 Illustration of the effects of detector saturation. The top figure is a time of flight spectrum from the $\pm 135^{o}$ banks, the bottom figure was taken from the $\pm 45^{o}$ banks. Saturation is worse at 135^{o} as the detector is closer to the sample and thus the count rate is higher.

beam. The effects of detector saturation are easily seen if these spectra are compared with figure 6.1. The detectors start to recover from saturation after $\simeq 300\mu sec$ and the detected intensity starts to increase although the incident intensity decreases monotonically with increasing time of flight from t=0.

The most serious potential problem associated with saturation is the possibility that the detector efficiency may be different, depending upon whether the analyser foil is in or out. The count rate is changed by the presence of the foil and if the detector is saturating, the efficiency is a function of count rate. This problem is particularly serious as it will not be affected by rapid cycling of the foil in and out. Another practical problem introduced by spectra such as that shown in figure 9.4 is that fitting of the foil out spectrum requires a higher order polynomial and care must be taken to ensure that a good fit is obtained and that no spurious oscillations are produced in the fit.

All these problems can be avoided by using only weak scatterers. From practical experience it appears that a 5% scatterer is the maximum which can safely be used. This does not seem a serious problem since count rates are high. The zirconium hydride data in figure 6.7 was collected during a 24 hour running period, using a sample which scattered 5% of the incident beam. There are in fact advantages in using thin samples, as multiple scattering and self shielding effects should be negligible. If for practical reasons a sufficiently thin sample cannot be produced, then an attenuator must be inserted in the incident beam. In principle the problem of detector saturation can be overcome by the use of scintillator detectors, which saturate less easily than gas detectors. However we note that γ-sensitive scintillators are not suitable as γ-rays are produced by the analyser foil during neutron capture.

9.3 Data Analysis

The current data analysis routines assume that the neutron Compton profile $J(y)$ is Gaussian, ie that the potential is harmonic. With this assumption the standard deviation of the distribution and hence the mean atomic momentum component parallel to the direction of q can be obtained by fitting to the data. As the quality of the data improves, deviations from Gaussian behaviour due to anharmonicity in the atomic potential should become apparent. For example a double well potential such as that described in section 7 should introduce oscillations into $n(p)$ with a periodicity inversely realated to the well separation. We hope that the improvements in stability introduced by, for example, foil cycling will allow for the observation of these more subtle features of the atomic momentum distribution. The data analysis routines will then have to be modified to allow for comparison with models other than the harmonic model.

Further desirable developments in data analysis are routines for deconvolution of

the instrumental resolution function, routines to fit postulated anisotropic momentum distributions in single crystals simultaneously to data from detectors at different angles and multiple scattering correction routines. Although multiple scattering effects should be small for the thin samples required to avoid detector saturation, a calculation of these effects will be necessary as the quality of the data available improves.

10 Summary

We have summarised the present state of development of neutron Compton scattering on the EVS spectrometer at ISIS. We believe that the data collected so far shows the potential of the EVS instrument for obtaining fundamental information on atomic dynamics. We anticipate that further improvement of the instrument and data analysis techniques will considerably improve the sensitivity of EVS during 1991.

Acknowledgements Thanks to Andrew Taylor for support and encouragement, to Zoe Bowden for technical assistance on EVS and to Bill David for supplying the Voigt function subroutine used in the fitting programs.

References

[1] 'Compton Scattering', edited by B Williams (Mcgraw-Hill, New York, 1977)

[2] P C Hohenberg and P M Platzmann, *Phys Rev* **152** 198 (1966)

[3] R N Silver *Phys Rev B* **38** 2283 (1988) and references therein.

[4] J Mayers Phys *Rev B* **41** 41 (1990) and references therein.

[5] S W Lovesey 'Theory of Neutron Scattering from Condensed Matter', Oxford University Press, London 1987, Vol. 1

[6] V F Sears *Phys Rev B* **30** 44 (1984)

[7] J Mayers, C Andreani and G Baciocco, *Phys Rev B* **39** 2022 (1989)

[8] M S Nelkin and D E Parks *Phys Rev B* **119** 1060 (1960)

[9] C G Windsor 'Pulsed Neutron Scattering', Taylor and Francis, 1981

[10] P A Seeger, A D Taylor and R M Brugger, *Nuc Inst Meth* **A240** 98 (1985)

[11] A D Taylor 'SNS Moderator Performance Predictions', Rutherford Appleton Laboratory Report, RAL-84-120, (1984)

[12] M P Paoli, D. Phil Thesis, Oxford University (1988)

[13] J Tomkinson, J Penfold and S T Robertson, Rutherford Appleton Laboratory Report, RAL-89-074, (1989)

[14] P Postorino, F Fillaux, J Mayers, J Tomkinson and R S Holt, *J Chem Phys* 94 4441 (1991)

[15] C Andreani, G Baciocco, R S Holt and J Mayers *Nuc Inst Meth* **A276** 297 (1989)

A Resolution of EVS in y Space

The resolution in momentum space for both direct and inverse geometry spectrometers has been treated in a previous paper [15]. We summarise the relevant results for EVS. The definition of y is

$$y = \frac{M}{q}\left(\omega - \frac{q^2}{2M}\right) \tag{42}$$

where q is the momentum transfer, ω the energy transfer and M the atomic mass. We calculate the partial derivatives of y at the centre of the recoil peak (ie at $y = 0$), with respect to the instrument parameters.

$$\frac{\partial y}{\partial x} = \left(\frac{\partial y}{\partial \omega}\right)\left(\frac{\partial \omega}{\partial x}\right) + \left(\frac{\partial y}{\partial q}\right)\left(\frac{\partial q}{\partial x}\right) = \frac{M}{q}\left(\frac{\partial \omega}{\partial x}\right) - \left(\frac{\partial q}{\partial x}\right) \tag{43}$$

where x is L_0,L_1, θ or E_1. The dominant contribution to the resolution comes from the energy resolution of the spectrometer. By direct differentiation, we obtain from equations 16 to 20,

$$\left(\frac{\partial \omega}{\partial E_1}\right) = -\left[1 + \left(\frac{L_1}{L_0}\right)\left(\frac{V_0}{V_1}\right)^3\right] = R_1 \tag{44}$$

and

$$\left(\frac{\partial q}{\partial E_1}\right) = \frac{m}{q}\left[1 - \left(\frac{L_1}{L_0}\right)\left(\frac{k_0}{k_1}\right)^3 + \left(\frac{L_1}{L_0}\right)\left(\frac{k_0}{k_1}\right)^2 \cos\theta - \left(\frac{k_0}{k_1}\right) cos\theta\right] = \frac{m}{q} R_2 \tag{45}$$

where m is the neutron mass, k_0 the wavenumber of the incident neutron, k_1 the wavenumber of the scattered neutron and the dimensionless parameters R_1 and R_2 are defined by equations 44 and 45. Using equation 43

$$\left(\frac{\partial y}{\partial E_1}\right)\Delta E_1 = \left[\left(\frac{M}{q}\right) R_1 - \left(\frac{m}{q}\right) R_2\right]\Delta E_1 \tag{46}$$

With q measured in $\AA^{-1}$, ΔE_1 in meV,

$$\left(\frac{\partial y}{\partial E_1}\right)\Delta E_1 = \frac{0.2413}{q}\left[\left(\frac{M}{m}\right) R_1 - R_2\right]\Delta E_1 \tag{47}$$

In a similar way, we obtain

$$\left(\frac{\partial y}{\partial \theta}\right)\Delta\theta = -\left(\frac{k_0 k_1 \sin\theta}{q}\right)\Delta\theta \tag{48}$$

$$\left(\frac{\partial y}{\partial L_0}\right)\Delta L_0 = \left\{k_0^2 \frac{\left[\frac{M}{m} - 1 + \frac{k_1}{k_0}cos\theta\right]}{qL_0}\right\}\Delta L_0 \tag{49}$$

$$\left(\frac{\partial y}{\partial L_1}\right)\Delta L_1 = \left\{\frac{k_0^3}{k_1}\frac{\left[\frac{M}{m} - 1 + \frac{k_1}{k_0}cos\theta\right]}{qL_0}\right\}\Delta L_1 \tag{50}$$

A.1 Resolution for $M = m$

When the atomic mass M is equal to the neutron mass, which is a very good approximation for scattering from hydrogen, the resolution expressions simplify considerably. At $y = 0$,

$$\omega = \frac{{k_0}^2 - {k_1}^2}{2m} = \frac{q^2}{2M} \tag{51}$$

When $M = m$ equation 51 reduces to

$${k_0}^2 = q^2 + k_1^2 \tag{52}$$

ie q is perpendicular to k_1 and

$$\frac{k_0}{k_1} = \frac{1}{\cos\theta} \tag{53}$$

$$q = k_1 \tan\theta = k_0 \sin\theta \tag{54}$$

Substituting in equations 44 to 50

$$\frac{\partial y}{\partial E_1} = -\frac{M}{q}\left[1 + \frac{L_1}{L_0 \cos\theta}\right] = -\frac{M}{k_1 \sin\theta}\left[\cos\theta + \frac{L_1}{L_0}\right] \tag{55}$$

$$\frac{\partial y}{\partial \theta} = -k_1 \tag{56}$$

$$\frac{\partial y}{\partial L_0} = \frac{k_1^2}{qL_0} = \frac{k_1}{L_0 \tan\theta} \tag{57}$$

$$\frac{\partial y}{\partial L_1} = \frac{k_0 k_1}{qL_0} = \frac{k_1}{L_0 \sin\theta} \tag{58}$$

A.2 Resolution for $M \gg m$

A second important special case is when the atomic mass is much greater than the neutron mass. In this case, it follows from equation 43 that only the contribution from the ω resolution is important. Thus the angular contribution to the y resolution is negligible since $\partial\omega/\partial\theta = 0$. The scattering is nearly elastic, so that $k_0/k_1 \simeq 1$ and $q = 2k_1 \sin(\theta/2)$. Then

$$\frac{\partial y}{\partial E_1} \simeq -M \frac{\left[1 + \frac{L_1}{L_0}\right]}{\left[2k_1 \sin\frac{\theta}{2}\right]} \tag{59}$$

$$\frac{\partial y}{\partial L_0} \simeq \frac{\partial y}{\partial L_1} \simeq \frac{Mk_1}{2L_0 \sin\frac{\theta}{2}} \tag{60}$$

$$\frac{\partial y}{\partial \theta} \simeq 0 \tag{61}$$

B Numerical Conversion Factors

In this report the following units are used;

Quantity	Unit	Abbreviation
energy	milli electron volts	meV
momentum	inverse Ångstroms	$\AA^{-1}$
mass	atomic mass units	amu
temperature	milli electron volts	meV

The conversion between temperature in meV and degrees Kelvin is,

$$T(meV) = 11.604T(K) \tag{62}$$

eg

$$300K = \frac{300}{11.604} = 25.9meV \tag{63}$$

The conversion factors for equations involving energy, momentum and mass can be derived from the numerical value of Planck's constant in this system of units.

$$\hbar = 2.04434(meV - amu)^{\frac{1}{2}}/\AA^{-1} \tag{64}$$

Thus the energy of the neutron ($m = 1.00867amu$) in meV is related to its momentum in $\AA^{-1}$ via

$$E = \frac{\hbar^2 k^2}{2m} = \frac{2.0443^2}{(2 \times 1.00867)} k^2 = 2.0717k^2 \tag{65}$$

The recoil energy $\omega_R = \frac{\hbar^2 q^2}{2M}$ is,

$$\omega_R = \frac{2.0717 q^2}{M} \tag{66}$$

and y is related to q, ω and M via

$$y = \frac{M}{\hbar^2 q}\left[\omega - \frac{q^2}{2M}\right] = \frac{0.2393 M}{q}\left[\omega - \frac{q^2}{2M}\right] \tag{67}$$